SOFT X-RAY SPECTROSCOPY OF A GAS-PUFF Z-PINCH

A Thesis Submitted for the Degree of

DOCTOR OF PHILOSOPHY

in the

UNIVERSITY OF LONDON

by

Gillian Nave

The Blackett Laboratory

Imperial College of Science and Technology

London SW7 2BZ

To Mary

for her Son

Jesus

ABSTRACT

Soft x-ray spectra between 9Å and 100Å produced by a gas-puff z-pinch have been recorded using a 5m grazing incidence grating spectrcgraph. Both axially and radially recorded spectra of argon, neon, nitrogen, and carbon dioxide have been obtained.

In argon plasmas, ionization stages from Ar IX up to Ar XV have been observed. The electron temperature was found from the line intensity ratios by assuming a coronal model. The absolute line intensity was then used to obtain the electron density.

H-like and He-like lines of low z plasmas were analysed to find the electron density, the electron temperature, the state of ionization of the plasma, and the plasma size. The electron temperature was found from both resonance line and satellite line ratios, and from the soft x-ray continuum. The electron density was found from satellite line intensity ratios and from the Stark and opacity broadened line profiles. The effect on these parameters of pre-ionizing the plasma was also investigated, together with the effect of varying the charging voltage.

TABLE OF CONTENTS

TITLE	1
DEDICATION	3
ABSTRACT	5
TABLE OF CONTENTS	7
LIST OF FIGURES	11
LIST OF TABLES	14
ACKNOWLEDGEMENTS	15
CHAPTER 1 INTRODUCTION	17
1.1 Introduction	17
1.2 High density, high temperature plasma sources.	18
1.3 Previous experiments on the gas-puff z-pinch.	20
1.4 X-ray spectroscopy as a diagnostic technique.	22
1.4.1 Spectroscopy of tokamaks.	23
1.4.2 Spectroscopy of laser plasmas.	25
1.5 The gas-puff z-pinch at Imperial College.	27
1.6 Soft x-ray spectroscopy of the gas-puff z-pinch.	34
1.7 The work in this thesis.	35

CHAPTER 2 THEORY OF PLASMA SPECTROSCOPY 37

2.1 Introduction 37

2.2 Line intensity ratios (excluding satellites). 39

2.2.1 Line intensities in the LTE model. 39

2.2.2 Criteria for LTE 41

2.2.3 Non-LTE models 44

2.2.3.1 The coronal model 46

2.2.3.2 The collisional-radiative model 48

2.3 Intensities of dielectronic satellite lines 48

2.3.1 Populations of the satellite levels 52

2.3.2 Satellite / resonance line intensity ratios 55

2.3.3 Ratio of the satellite intensities 58

2.4 The collisional-radiative model and interpretation of the observed intensities 61

2.5 Continuum intensities 64

2.6 Line broadening processes 64

2.6.1 Natural and Doppler broadening 65

2.6.2 Stark broadening 66

2.6.3 The effect of opacity 69

2.6.4 Interpretation of observed line profiles. 71

2.7 Concluding remarks 74

CHAPTER 3 THE EXPERIMENT 76

3.1 Introduction 76

3.2 Geometry of Rowland circle spectrographs 78

3.3 The spectrograph 81

3.3.1 Gratings used 87

3.3.2 Photographic plates 87

3.4 Focussing and adjustment of the spectrograph 89

3.5 Calibration of the spectrograph 89

3.6 Analysis of the spectra 93

CHAPTER 4 SPECTRA OF ARGON DISCHARGES 95

4.1 Introduction 95

4.2 Results 95

4.3 Spatially resolved spectra 124

4.4 Analysis of the spectra 127

CHAPTER 5 SPECTRA OF LOW Z DISCHARGES 133

5.1 Introduction 133

5.2 Analysis of CO_2 spectrum 133

5.2.1 Electron temperature measurements 142

5.2.1.1 Slope of the soft x-ray continuum 142

5.2.1.2 Satellite / resonance line intensity ratio 145

5.2.1.3 Ionization of the plasma 147

5.2.2 The electron density 150

5.2.2.1 Satellite line intensity ratios 150

5.2.2.2 Line broadening 151

5.2.3 Discussion 171

5.3 The effect of pre-ionization 173

5.4 Results obtained in other gases 179

CHAPTER 6 CONCLUSIONS 189

6.1 Summary of results 189

6.2 Suggestions for further work 191

LIST OF FIGURES

1.1 THE GAS-PUFF Z-PINCH AT IMPERIAL COLLEGE 28

1.2 X-RAY DIODE AND PIN DIODE TRACES 29

1.3 PINHOLE PHOTOGRAPH 32

1.4 SPECTRUM OF ARGON OBTAINED WITH PET CRYSTAL SPECTROMETER 33

2.1 IONIZATION OF OXYGEN IN COLLISIONAL-RADIATIVE EQUILIBRIUM 45

2.2 ENERGY LEVELS OF HE-LIKE AND LI-LIKE DIELECTRONIC SATELLITES 49

2.3 PROCESSES INVOLVED IN DIELECTRONIC SATELLITE FORMATION 52

2.4 INTENSITY RATIO $\frac{AD + QR}{JKL}$ FOR OXYGEN 59

2.5 INTENSITY RATIO $\frac{2s2p(^3P)\text{-}1s^2 2s + 2p^2(^3P)\text{-}1s2p}{2p^2(^1D)\text{-}1s2p}$ FOR OXYGEN 60

2.6 IDEALIZED LINES OF BEST FIT FOR A LINE SERIES 73

3.1 THE ROWLAND CIRCLE 79

3.2 DIAGRAM OF THE GML5M GRAZING INCIDENCE GRATING SPECTROGRAPH 82

3.3 THE GML5M GRAZING INCIDENCE GRATING SPECTROGRAPH 83

3.4 EFFICIENCY OF GRATING 2 AS A FUNCTION OF ANGLE 85

3.5 EFFICIENCY OF GRATING 1 AS A FUNCTION OF ANGLE 86

3.6 PERCENTAGE TRANSMISSION OF 0.2 μM PMMA FILM AS A FUNCTION OF WAVELENGTH 86

3.7 THE EXPERIMENTAL ARRANGEMENT 88

3.8 FWHM OF AR IX LINES AS A FUNCTION OF THE FOCUS OF SPECTROGRAPH 90

3.9 INTENSITY CALIBRATION CURVE FOR THE SPECTROGRAPH 92

4.1 CARBON DIOXIDE AND ARGON SPECTRA 99

4.2	ARGON SPECTRA	101
4.3	ARGON SPECTRA	103
4.4	DENSITOMETER TRACE OF ARGON SPECTRUM IN FIGURE 4.1	105
4.5	DENSITOMETER TRACE OF ARGON XV SPECTRUM	109
4.6	RADIALLY AND AXIALLY RESOLVED ARGON SPECTRA	125
4.7	IONIZATION BALANCE FOR ARGON ASSUMING CORONAL EQUILIBRIUM	129
5.1	CARBON DIOXIDE SPECTRA	137
5.2	DENSITOMETER TRACE OF CARBON DIOXIDE SPECTRUM	139
5.3	RADIAL DENSITOMETER TRACE ACROSS MAJOR LINES IN CARBON DIOXIDE SPECTRUM	141
5.4	SLOPE OF THE SOFT X-RAY CONTINUUM FOR CARBON AND OXYGEN	143
5.5	IONIZATION BALANCE FOR CARBON AT 10^{20} CM^{-3}	148
5.6	IONIZATION BALANCE FOR OXYGEN AT 10^{21} CM^{-3}	149
5.7	FITTING OF OXYGEN LYMAN α SATELLITES	152
5.8	FITTING OF OXYGEN $2^1P - 1^1S$ SATELLITES	153
5.9	FITTING OF CARBON LYMAN α SATELLITES	154
5.10	FITTING OF CARBON $2^1P - 1^1S$ SATELLITES USING GABRIEL'S WAVELENGTHS	155
5.11	FITTING OF CARBON $2^1P - 1^1S$ SATELLITES USING VAINSTEIN AND SAFRANOVA'S WAVELENGTHS	156
5.12	FITTING OF CARBON LYMAN LINES FOR SPECTRUM IN FIGURE 5.1B	158
5.13	FITTING OF CARBON LYMAN LINES FOR SPECTRUM IN FIGURE 5.1C	159
5.14	CARBON LYMAN LINE PROFILES FOR SPECTRUM IN FIGURE 5.1B	160
5.15	CARBON LYMAN LINE PROFILES FOR SPECTRUM IN FIGURE 5.1C	164

5.16 FITTING OF OXYGEN LYMAN LINES FOR SPECTRUM IN FIGURE 5.1 B 167

5.17 OXYGEN LYMAN LINE PROFILES IN FIGURE 5.1B 168

5.18 CARBON DIOXIDE SPECTRUM TAKEN WITHOUT PRE-IONIZATION 175

5.19 DENSITOMETER TRACE OF CARBON DIOXIDE SPECTRUM TAKEN WITHOUT PRE-IONIZATION 177

5.20 SLOPE OF THE SOFT X-RAY CONTINUUM FOR SPECTRUM IN FIGURE 5.18 178

5.21 NEON SPECTRA 181

5.22 DENSITOMETER TRACE OF NEON SPECTRA 183

5.23 RADIAL DENSITOMETER TRACE ACROSS MAJOR LINES IN NEON SPECTRUM 188

LIST OF TABLES

2.1	CRITERIA FOR LTE TO HOLD IN VARIOUS PLASMAS	43
2.2	WAVELENGTHS, RADIATIVE RATES AND AUTOIONIZING RATES FOR DIELECTRONIC SATELLITES IN CARBON, OXYGEN AND NEON	53
2.3	LEVELS INCLUDED IN COLLISIONAL-RADIATIVE CODE	62
2.4	DIFFERENT METHODS FOR FINDING KT_e AND N_e	75
3.1	PARAMETERS FOR THE GML5M SPECTROGRAPH	92
4.1	EXPERIMENTAL CONDITIONS FOR THE SPECTRA IN CHAPTER 4	96
4.2	WAVELENGTHS AND INTENSITIES OF OBSERVED LINES IN AR	111
4.3	SUMMARY OF TABLE 4.2	121
4.4	WAVELENGTHS AND INTENSITIES OF AR XV LINES	122
4.5	WAVELENGTHS AND OSCILLATOR STRENGTHS FOR AR LINES	127
4.6	CALCULATED TEMPERATURE FOR PLATES IN FIGURES 4.1 - 4.5	130
4.7	CALCULATED ELECTRON DENSITIES FOR SPECTRUM IN FIGURE 4.3A	132
5.1	EXPERIMENTAL CONDITIONS FOR PLATES IN CHAPTER 5	134
5.2	WAVELENGTHS AND INTENSITIES OF OBSERVED LINES IN CO_2	136
5.3	WAVELENGTHS, RADIATIVE RATES AND AUTOIONIZATION RATES FOR LINES USED IN CHAPTER 5	146
5.4	ELECTRON TEMPERATURE AND IONIZATION BALANCE OF CO_2S	150
5.5	SUMMARY OF RESULTS OBTAINED FROM CO_2	172
5.6	SUMMARY OF RESULTS OBTAINED FROM CO_2 WITHOUT PRE-IONIZATION	174
5.7	WAVELENGTHS AND INTENSITIES OF OBSERVED LINES IN NE	180
5.8	SUMMARY OF RESULTS OBTAINED FROM NE	187

ACKNOWLEDGEMENTS

I would like to thank my supervisor Dr R. J. Speer for suggesting this work, and for his help and support, particularly during the experimental phase of the project. I would also like to thank Bucker Dangor for his constant help and encouragement. Thanks should also go to Dr J. G. Lunney for much help and advice about the theory of plasma spectroscopy.

My collaborators in this project have been a constant source of help and friendship. Mrs Jing Liu deserves special thanks for her help in taking the results. Clive Challis must also be thanked for firing the pinch, particularly when his own project did not directly benefit.

I would also like to thank the people who have helped me in the writing of this thesis. In particular I wish to thank those who have helped with the proofreading and have given their advice.

The members of the spectroscopy and plasma physics groups have also given me much advice and friendship. All deserve special thanks, but space prevents me from mentioning them all by name.

Finally I would like to thank my husband Joe for his

constant love and support throughout this work, particularly in the more difficult phases of the project. I hope that I shall be able to support him in his future studies.

CHAPTER 1 INTRODUCTION

1.1 INTRODUCTION

For many years, there has been an interest in high density, high temperature plasmas, and there have been several devices to produce them. The initial interest in plasma sources stemmed from fusion research. Here, high temperatures are needed in order to sustain the fusion reaction, and a high density x containment time is needed in order to ensure that the Lawson criterion is satisfied (Haines,1982).

High temperature plasmas were also found to be good sources of x-rays, and further research has investigated their use as an x-ray source for various applications such as lithography, microscopy, studies of crystal structure, and x-ray lasers (AIP conf. proc., 1981). As the temperature increases, the wavelength of the peak of the free-free emission decreases, the plasma becomes more highly ionized, and hence the wavelength of line emission also decreases (de Michelis & Mattioli, 1981).

Related to this is the study of emission spectra of ions of high Z. This is of interest for diagnosis of fusion devices such as JET as well as the study of solar spectra, where much work has been done now it is possible to put spectrographs into space. Study of the soft x-ray solar

spectrum yields valuable information about the constituent elements in the sun, and also the conditions in both the corona and solar flares (Feldman, 1981). More recently, there has been much interest in the development of soft x-ray lasers (Matthews et al, 1985). High density plasmas have also been used to test models of ionization, radiation transport, and non-ideal plasma effects (de Michelis & Mattioli, 1981).

1.2 HIGH DENSITY, HIGH TEMPERATURE PLASMA SOURCES

The highest densities and temperatures achieved so far have been found in laser induced plasmas, where temperatures of a few keV and densities of over $10^{23}cm^{-3}$ have been reported (Kilkenny et al., 1980). The interest in these plasmas is for inertial confinement fusion, for which two methods have been proposed. For inertial confinement by indirect drive, the incident laser beam produces x-rays in the target, which in turn compress the pellet (IAEA conf. proc., 1984). The plasmas produced are small, typically between 1μm and 1mm. The lasers used in order to compress the pellet are very large; the largest producing 10kJ in 1ns. (Sigel, 1982) The conversion efficiency to x-rays is also high, typically 20%. Consequently there has been much interest in such sources for the development of x-ray lasers.

Smaller devices which produce high density and temperature

plasmas include the plasma focus (Mather, 1971), the vacuum spark (Elton, Lie, 1971), and the exploding wire device (Burkhalter et al, 1979). In all these devices, the plasma is ionized with an electrical discharge with stored energy of 10 - 100kJ. The efficiency of such devices is low (~1%) and they do not scale well with input energy. The plasmas produced are therefore of much lower density and temperature than laser produced plasmas.

There has been renewed interest recently in dense z-pinches as a source for high density and temperature plasmas, Although initially thought to be too unstable for a fusion reactor, recent work has suggested that they may indeed be suitable for fusion research (Haines 1982). In the z-pinch, the self azimuthal field produced by an axial current both compresses and heats the plasma. Of particular interest is the gas-puff z-pinch, in which the plasma is formed from a hollow shell of gas (Shiloh et al 1978). Plasmas with electron temperatures of a keV and densities of $10^{20}cm^{-3}$ have been reported from such devices (Burkhalter et al 1979). These devices have been found to be cheap, laboratory sources of x-rays with yields of up to 50kJ from the largest device (Spielman private communication). Conversion efficiencies to soft x-rays are of the order of 0.5%. For these reasons there has been much interest in them recently as sources for a photon pumped x-ray laser.

In the next section, the history of the gas-puff z-pinch will be described. The use of x-ray spectroscopy for diagnosis of plasmas will be reviewed, and then the gas-puff z-pinch at Imperial College will be described.

1.3 PREVIOUS EXPERIMENTS ON GAS-PUFF Z-PINCHES

The gas-puff z-pinch originated from a z-pinch device designed by Shiloh, Fisher and Rostoker (1978). In this device, a high pressure, collimated, solid jet of gas was injected through a hollow anode. This was then ionized, compressed and heated by a 2.8μF, 30kV capacitor bank, forming a plasma with a temperature of between 6 and 9 keV, and density of over $10^{18}cm^{-3}$. The device was found to be far more efficient in producing x-rays than either the vacuum spark or the plasma focus, and recent work has shown that the device can be scaled to higher energies (Spielman private communication).

Further experiments on the gas-puff showed that higher densities could be achieved by using a cylindrical hollow shell of plasma rather than a simple solid jet (Shiloh et al 1979). When the current flows, the interaction with its own azimuthal magnetic field gives rise to an inward force. This causes the plasma to collapse, creating a high density plasma. The temperature is raised by Joule heating, and the conversion of kinetic energy of the collapse.

With a hollow shell, a constant mass of gas is accelerated, so the kinetic energy of the collapsing shell can be large. Experiments with the hollow shell pinch showed that copious quantities of soft x-rays were emitted (Burkhalter et al 1979), in addition to harder x-rays (>200keV) (Shiloh et al 1978).

The initial observations of these experiments looked at the soft x-ray output using various gas loads (Burkhalter et al 1979). PIN diode traces indicated the time and duration of the pinch. Pinhole photographs filtered to >1keV indicated that most of the x-ray emission was emitted from a series of submillimetre localized regions, aligned along the axis of the discharge. More recent observations have confirmed the existence of an electron beam in an argon plasma (Kania, Jones to be published), using a Faraday cup with various thin foil filters in order to obtain the current, energy and duration of the beam.

X-ray spectra were reported using various crystal spectrographs, over the range 1keV to 3keV in argon (Bleach et al 1980). These have been analysed using a collisional-radiative equilibrium model to give the electron temperature based on line intensity ratios of H-like and He-like ions. Soft x-ray spectra in the range 100eV to 1 keV, from a grating spectrograph were reported, which were analysed using LTE and coronal models. These indicated peak elec-

tron temperatures of 1keV and densities of $2x10^{21}cm^{-3}$. No further analysis of x-ray spectra from gas-puffs has been reported.

Theoretical work on gas-puff z-pinches has attempted to model the dynamics of the collapse, and obtain synthetic soft x-ray spectra. Davies et al (1982) have used a collisional-radiative equilibrium model, together with density and temperature profiles from 1-D hydrocodes, in order to generate synthetic spectra of argon. Similar codes have also been used to investigate the effect of radiative cooling on the implosion dynamics (Maxon, Wainwright 1984).

1.4 X-RAY SPECTROSCOPY AS A DIAGNOSTIC TECHNIQUE

Soft x-ray spectroscopy of high temperature plasmas has been used for a number of years to both study plasmas and understand the soft x-ray spectrum. Previous to 1970, most of the work concentrated on the classification of soft x-ray lines, and used a variety of plasma sources (e.g. the vacuum spark device (Elton and Lie 1971); tokamaks (Gill 1981); and the plasma focus (Mather 1971)). This work has proved invaluable to the understanding of both the plasma physics of the devices, and the solar spectrum. More recent work has used the soft x-ray spectrum to obtain information about the electron density, electron temperature and ionization of the plasma. This work has recently

been reviewed by de Michelis and Mattioli (1981).

As the temperature of a plasma increases, the peak wavelength of the free-free continuum decreases according to:

$$\lambda_{max} = 6200 / kT_e \qquad 1.1$$

where λ_{max} is in Ångstroms, kT_e is the electron temperature in eV. The intensity of the continuum also scales with the electron density n_e^2. The wavelength of the more intense line emission from a particular transition in an ion of charge z scales:

$$\lambda \sim 1 / z^2 \qquad 1.2$$

The study of H-like and He-like ions of low Z elements (Z = 5-11) will thus fall in the soft x-ray region, and high temperatures are also needed in order to sufficiently ionize the plasma. The study of H-like and He-like ions is useful, not only because the atomic physics is simpler for these ions, but also because they provide a good indication of the conditions in the hottest part of the plasma.

1.4.1 SPECTROSCOPY OF TOKAMAKS

In low density plasmas ($\sim 10^{13} cm^{-3}$) such as tokamaks, the electron temperature and electron density are normally

found using Thomson scattering and interferometry. X-ray spectroscopy is then used for an independent measurement of kT_e and for an estimate of the impurity concentration and consequent radiated power losses.

An independent measurement of kT_e in a tokamak is useful because only a few measurements of kT_e can be made during the discharge if Thomson scattering is used. The two main methods are:

(i) Slope of the soft x-ray continuum (Jahoda et al, 1962)

(ii) Line intensity ratios (McWhirter, 1965).

In order to estimate the temperature, a coronal model is usually assumed. Local measurements can be found from spatially resolved intensities by an Abel inversion of the profiles (Griem, 1964).

An estimate of the impurity content of tokamak plasmas is important because they radiate away a significant portion of the total energy in a discharge. In order to avoid the difficult task of evaluating the absolute intensities of all the spectral lines and continua, it is usual to measure the absolute intensities of a few lines in order to measure the impurity content of the plasma. The radiated power loss can then be calculated using one of the published models.

1.4.2 SPECTROSCOPY OF LASER PLASMAS

The problems in high density plasmas ($n_e \sim 10^{21} - 10^{23}$ cm^{-3}) such as laser plasmas are quite different to those in tokamak-type plasmas. Here, x-ray spectroscopy is essential in providing a measurement of kT_e and n_e. This is because visible light is strongly absorbed for densities above $10^{19} cm^{-3}$, and hence Thomson scattering and interferometry cannot be performed. There are three basic features in high density plasmas which can be used for analysis:

(i) Line intensities and intensity ratios.

(ii) Continuum intensities and intensity ratios.

(iii) Line broadening.

Line intensity ratios from a high density plasma can give estimates of the electron temperature, the ionization, and electron density. The intensity ratios of lines from the same ionization stage can give the electron temperature if LTE is assumed. For lines from different ionization stages, this will give an estimate of the ionization of the plasma, which in turn gives kT_e (Griem 1964). The intensities of satellite lines relative to the parent resonance line also gives a measurement of electron temperature (Gabriel et al 1975). These dielectronic satellite lines are produced by the radiative decay of doubly

excited levels in an ion. The relative intensities of the satellites themselves give an estimate of the electron density (Jacobs Blaha 1980). This can also be found by the intensity ratio of the intercombination line and the resonance line of a helium-like ion (Vinogradov et al 1975). It should be noted however, that all these methods will fail if any of the lines used are optically thick. Hence it is important to chose high n series lines which are more likely to be optically thin.

The most important parameter that can be obtained from the soft x-ray continuum is the electron temperature. This is estimated from the slope of the continuum using the same method as is used in tokamaks (Jahoda et al 1962). Absolute intensity measurements of the continuum can also give either ion densities or the duration of emission of the plasma.

The broadening of spectral lines from high density plasmas is usually due to Stark or opacity broadening, and Doppler broadening is rarely significant. The initial way of estimating n_e in laser plasmas was to measure the widths of optically thin members of a series, and then estimate the opacity of the other lines. This gives the ion density x length product, which is important in thermonuclear fusion (Key et al 1979). More recent work has extended this method to fit a whole line series consistently (Kilkenny et al 1980). It is thus possible to estimate both n_e and

n_i without assuming the opacity of the lines used.

1.5 THE GAS-PUFF Z-PINCH AT IMPERIAL COLLEGE

The Imperial College gas-puff z-pinch is shown in figure 1.1. A cylindrical hollow shell of gas is produced by an electromagnetically driven valve, which causes the high pressure gas (~8 atmospheres) contained in the plenum to flow through the nozzle, producing a supersonic jet. This is in the form of a hollow gas shell of 3 or 5 cm radius (depending on the size of nozzle used), thickness 0.5 cm and length equal to the electrode separation of 2 cm. The flow of gas is detected by a spark gap, which is used to trigger a 9μF capacitor bank charged to 27kV. This ionizes the gas column, and creates a current which causes the gas to collapse radially inwards by the jxB force. As the shell is hollow, the collapse is more rapid than for a solid gas column, and the plasma achieves a greater kinetic energy. When the plasma stagnates on the axis, this directed kinetic energy thermalizes, thus forming a high density, high temperature plasma. The dynamics of the discharge can be controlled by varying the gas pressure, the applied voltage, and the delay between opening the valve and discharging the capacitor bank. The effect of pre-ionizing the gas will be investigated further in chapter 5.

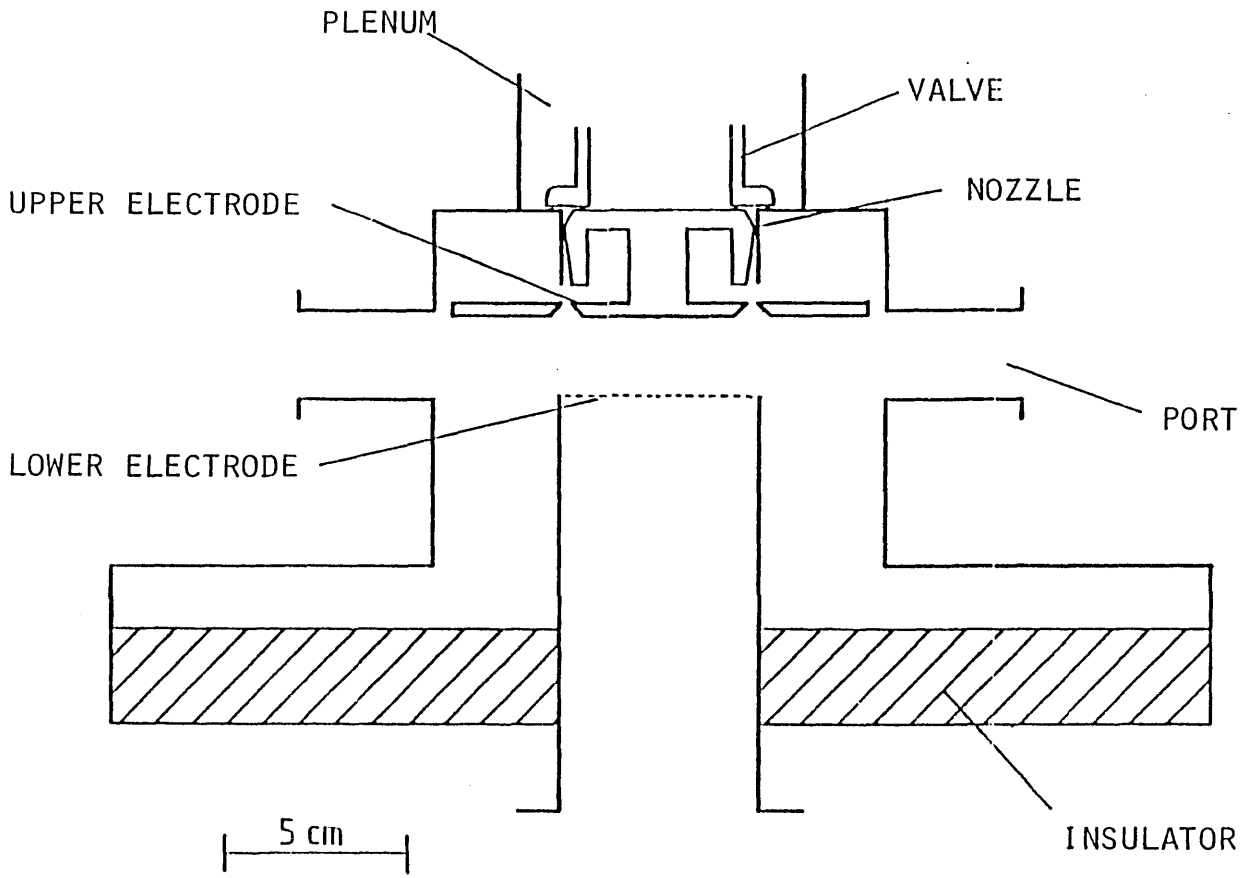
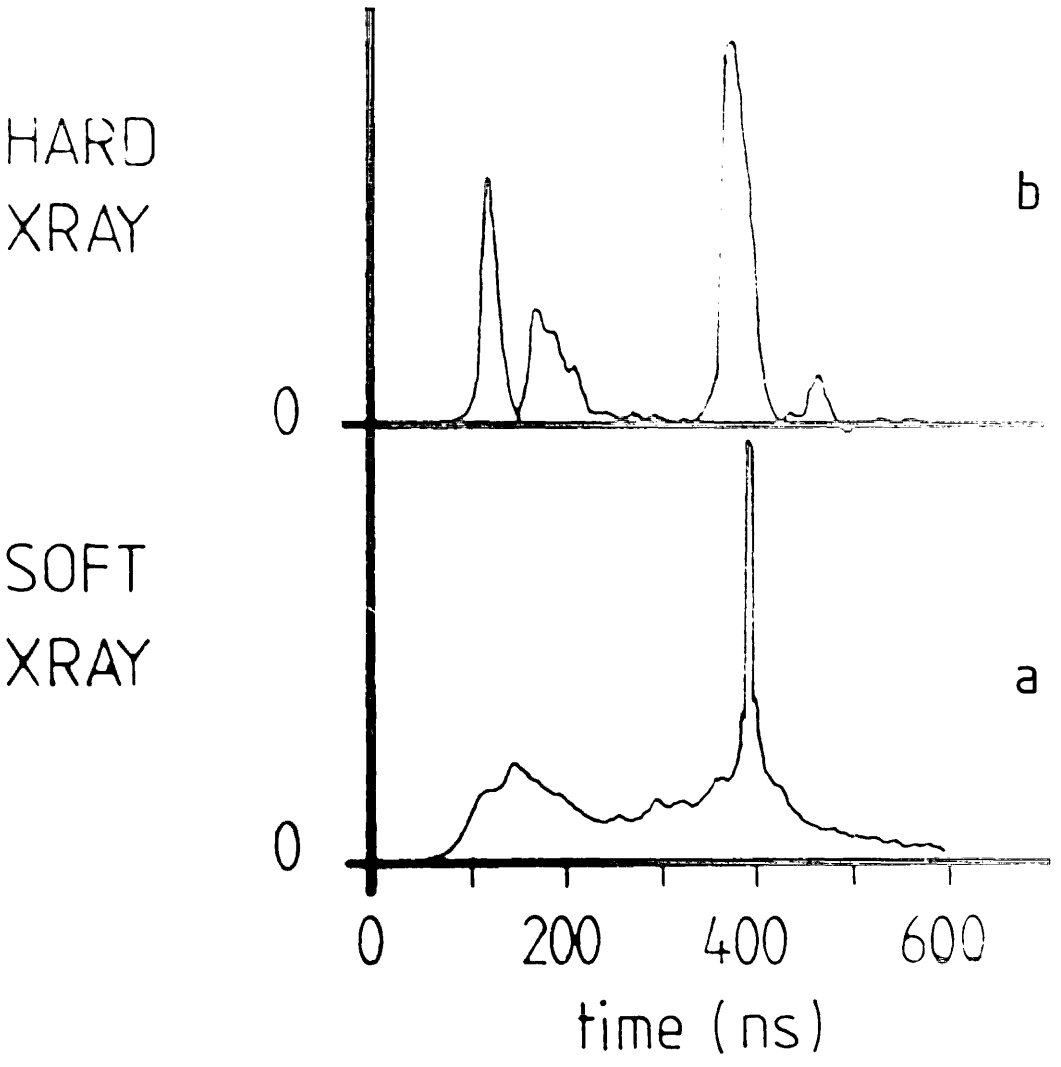


FIGURE 1.1 THE GAS-PUFF Z-PINCH AT IMPERIAL COLLEGE
Reproduced from Challis (1986)

Figure 1.2 XRD and PIN diode traces



31

Apart from soft x-ray spectroscopy, a variety of other work has been done on the gas-puff z-pinch. Much of this has studied the hard x-ray emission and its relationship with observed electron beams. However a variety of work has also studied the soft x-ray radiation emitted from the background plasma, and this will now be reviewed. Most of this work was conducted by C. D. Challis, and further details of it can be found in his thesis. (Challis 1986)

Figure 1.2a shows the time history of the soft x-ray emission as measured by a filtered x-ray diode. This was filtered with 5μ m of kimfoil ($C_{16}H_{14}O_3$) and responds mainly to radiation between 40 Å and 60 Å. It shows that soft x-rays were emitted for the entire lifetime of the plasma on axis, with peaks of emission typically separated by 100ns. The total duration of soft x-ray emission was 200ns.

Figure 1.2b shows the time history of harder x-ray emission using a PIN diode filtered to respond to radiation below 12Å. It shows that the harder radiation also comes in several peaks correlated to the peaks in the soft x-ray emission, of 10 ns duration.

The spatial extent of the plasma has been studied using both pinhole photography and optical streak photography. Figure 1.3 shows a pinhole photograph filtered with 12μ m of aluminized mylar to respond to radiation below 12Å.

32

Three localized hard x-ray emitting regions are shown, of 160 μm in diameter and 700μm long; usually referred to as 'hot-spots'. Hard x-rays are also emitted from the anode, and are shown at the top of the photograph. Optical streak photography indicates that the background plasma forms a column of diameter 2-3mm. The number of hot-spots observed usually correlates with the number of peaks in the hard x-ray emission monitored by the PIN diode, indicating that these are usually formed at the same time.

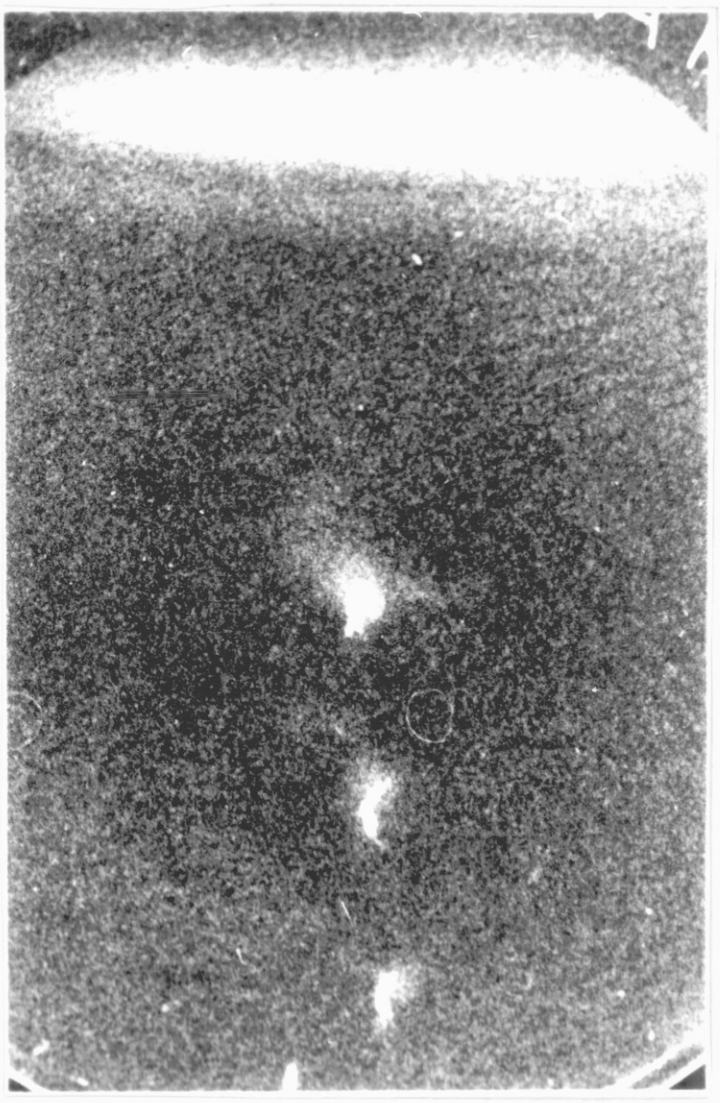
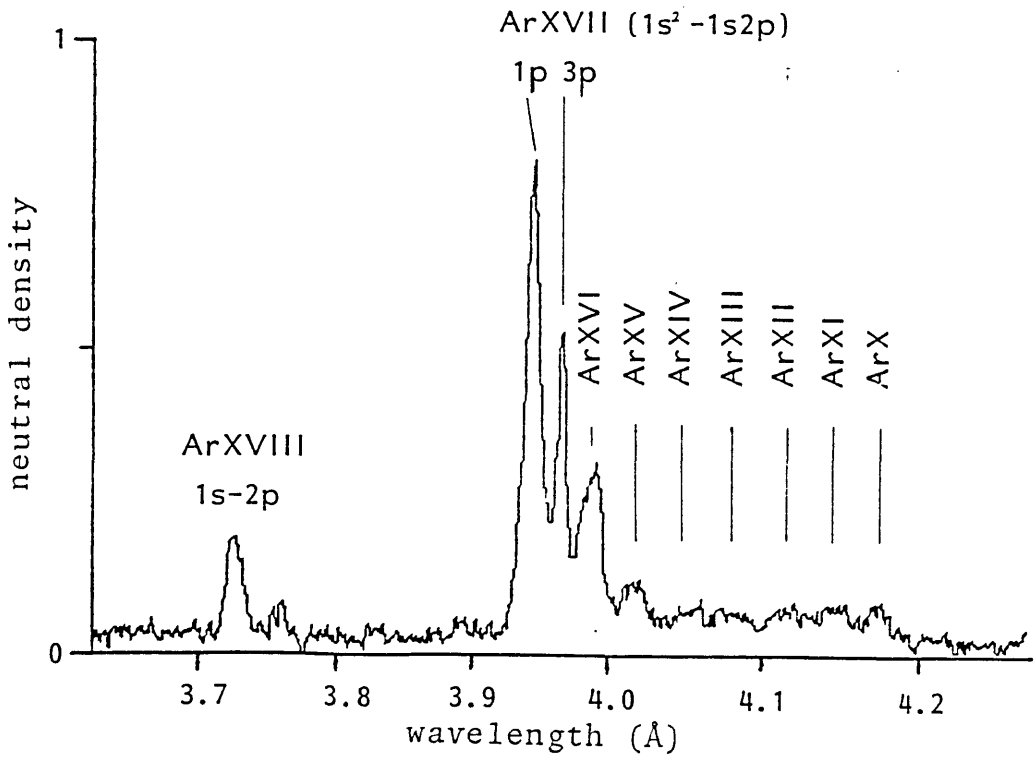


Figure 1.3
Pinhole photograph

Figure 1.4 shows the hard x-ray spectrum of argon obtained with a PET crystal spectrometer. It illustrates the dominant He-like $1s^2(^1S)$ - $1s2p(^1P)$ transition with the intercombination line and dielectronic satellites. On the right are the inner shell transitions which are probably the result of the interaction of an electron beam on the cool background plasma. The implied electron temperature from the ratio of the He-like to H-like resonance lines is 1keV, and the electron density from the intercombination to He-like resonance line ratio is $10^{21}cm^{-3}$. The dielectronic satellites however indicate a much higher electron density of $10^{23}cm^{-3}$, and it is probable that these satellites are affected more by the electron beam than by the surrounding plasma.

FIGURE 1.4 SPECTRUM OF ARGON OBTAINED WITH PET CRYSTAL SPECTROMETER



Reproduced from Challis (1986)

The implosion of an argon plasma shell has been theoretically modelled by C. D. Challis. The zero-dimensional model calculated the current history in the gas-puff assuming the initial mass of the shell, its length and the axial discharge current. This current history was then used to obtain a shell mass of 80μg from the observed collapse times. This in turn gives an ion density of 4 x $10^{19}cm^{-3}$, assuming a column diameter of 2mm, as observed from optical streak photography. The total kinetic energy of the collapsing shell was calculated from the shell mass, and was found to be 240J, roughly 7% of the electrical energy stored in the capacitor bank. Assuming the plasma thermalizes uniformly, the temperature was then calculated; firstly by assuming the energy is split between ionization energy and thermal energy; and secondly by assuming the plasma is fully ionized during collapse. The collisional-radiative model (Lee et al 1984) was used in both cases to give the ionization as a function of electron temperature. The estimated temperature was found to be 25eV using the first method, and 45eV using the second.

1.6 SOFT X-RAY SPECTROSCOPY OF THE GAS-PUFF Z-PINCH

There are several reasons for doing soft x-ray spectroscopy on the gas-puff z-pinch. Pinhole photography and x-ray diode traces suggest that the soft x-rays come from the background confined plasma rather than the hot spots, for which there are no other diagnostics. For low Z plas-

mas, hot spots do not appear to be formed, and the soft x-rays then provide a diagnostic of the peak density and temperature in the plasma. In high Z plasmas where electron beams are formed, soft x-rays are less liable to be affected by the high energy electron beams, and hence provide a diagnostic of the thermal plasma. Analysis of the spectra also provides a good test of the theoretical models used, which have not been tested in this region. Little analysis of soft x-ray spectra from previous gas-puff z-pinch experiments has been done. This would be of importance not only in the proposed use of gas-puff z-pinches as soft x-ray sources, but also in their proposed use for soft x-ray laser schemes.

1.7 THE WORK IN THIS THESIS

This thesis will describe the study of the soft x-ray spectrum of the gas-puff z-pinch at Imperial college. Chapter 2 will review the theory of the soft x-ray spectrum, showing how analysis of the line and continuum intensities can be used as temperature diagnostics. The use of line broadening theories and relative satellite line intensities will also be discussed. In chapter 3, the experiment will be described, together with a discussion of why a grazing incidence grating spectrograph was used, and a summary of the preliminary methods for analysing the resulting data. In chapter 4, example spectra of argon

will be presented, and it will be shown how the analysis gives information about both the diffuse background plasma, and also the confined thermal plasma. The effect of pre-ionizing the plasma will also be discussed. Chapter 5 will analyse the results obtained in low Z plasmas (carbon dioxide, nitrogen, neon) looking at one spectrum in detail, and summarizing the results of others. Studies of the effects of changing the gas used, pre-ionizing the gas, and changing the plenum gas pressure will be presented. These results will be compared to the theoretical models, and also to other hard x-ray diagnostics of the plasma.

CHAPTER 2 THEORY OF PLASMA SPECTROSCOPY

2.1 INTRODUCTION

As mentioned in the previous chapter, there are three important methods of analysing spectra that are useful for diagnosis of the plasma conditions. They are:

(i) Study of relative and absolute line intensities.
(ii) Study of relative and absolute continuum intensities.
(ii) Line broadening studies.

In most laboratory plasmas, the collective effects of the particles dominate over their individual character. This occurs when the Debye length is much greater that the inter-ion spacing (Griem 1964), and the mean electron - electron collision time is much less that the duration of the plasma. The electron velocity distribution will then be Maxwellian, with temperature T_e, defined as the electron temperature. Several different processes affect the populations of excited states of the ions. These are:

(i) Collisional excitation and de-excitation.
(ii) Radiative excitation and decay.
(iii) Radiative recombination and photo-ionization.
(iv) Collisional ionization and recombination.

Although the complete solution for the population of any particular level is very complex, it is possible to simplify the situation by ignoring some of these processes in order to formulate a model. The most important models used are:

(i) Local thermodynamic equilibrium. (LTE)
(ii) Coronal equilibrium.
(iii) Collisional-radiative equilibrium.

Although these models are strictly valid only in homogeneous, steady-state plasmas, they can be used with success to describe transient, radiating plasmas such as those found in the laboratory.

This chapter will review the way in which these models have been implemented in this thesis in order to obtain various plasma parameters such as the electron density and temperature. Section 2.2 will describe how each of the models can be used in order to calculate the electron temperature and state of ionization of the plasma, and discuss under what conditions each of the models is valid. In section 2.3, the mechanisms that determine the intensities of dielectronic satellite lines will be presented, and it will be shown how they can be used in order to obtain the electron density and temperature. Section 2.4

will describe how the observed intensities were analysed, and section 2.5 will discuss the intensities of continua. Section 2.6 will discuss the various mechanisms that broaden spectral lines, and it will be shown how observed line profiles were used in order to obtain electron and ion densities.

2.2 LINE INTENSITY RATIOS (EXCLUDING SATELLITES)

2.2.1 LINE INTENSITIES IN THE LTE MODEL

In the LTE model, it is assumed that all processes are accompanied by the inverse process (principle of detailed balance). Hence the level populations will be the same as those for a system in thermodynamic equilibrium, and if the plasma is optically thin, these will be determined purely by electron collisions. The populations are given by the Boltzmann and Saha equations (Griem 1964) :

$$\frac{n(p)}{n(q)} = \frac{g(p)}{g(p)} \exp\left(\frac{-E(p,q)}{kT_e}\right) \qquad 2.1$$

$$n_e \frac{n(z+1,g)}{n(z,g)} = \frac{g(z+1,g)}{g(z,g)} .2 \left(\frac{2\pi mkT_e}{h^2}\right)^{3/2} \exp\left(\frac{-E(z,g)}{kT_e}\right) \qquad 2.2$$

where n_e is the electron density; kT_e is the temperature in eV; n(p) and n(q) are the populations of ions in states p and q; n(z,g),n(z+1,g) are the populations of ionization stages z and z+1 in their ground state g;

g(p),g(q),g(z,g),g(z+1,g) are the statistical weights of the various levels; E(p,q) is the energy required to excite an ion from level q to level p; and E(z,g) is the ionization potential of an ion of charge z in eV.

The intensity of an optically thin line due to the radiative decay of a level p to level q is (McWhirter 1965) :

$$I(p,q) = \int n(p).A(p,q).E(p,q)\ dV \qquad 2.3$$

where A(p,q) is the transition probability for decay and the integral is over the volume of the plasma. Hence the intensity ratio for two lines of the same ionization stage is (Griem 1964):

$$\frac{I(p,q)}{I(q,g)} = \frac{A(p,g).E(p,g).g(p)}{A(q,g).E(q,g).g(q)} \exp \frac{E(p,g)-E(q,g)}{kT_e} \qquad 2.4$$

This is independent of both electron and ion density, and is a good temperature diagnostic if $E(p,g) - E(q,g) > kT_e$. This however, requires that the lines be well separated in wavelength, thus introducing problems if the spectrograph is not accurately calibrated for intensity.

For two lines of different ionization stages z and z+1, the line intensity becomes :

$$\frac{I(z,p)}{I(z+1,q)} = \frac{A(z,p,g)}{A(z+1,q,g)} \frac{E(z,p,g)}{E(z+1,q,g)} \frac{n(Z+1,g)}{n(z+2,g)} \frac{g(z+2,g)}{g(z+1,g)}$$

$$\frac{g(z,p)}{g(z+1,p)} \exp \frac{(E(z+1,q,\ ) - E(z,p,\ ))}{kT_e} \qquad 2.5$$

where $E(z,p,\infty)$ is the energy required to ionize an ion of charge z in level p. Now if $kT_e << E(z+1,q,\infty) - E(z,p,\infty)$, the exponential in equation 2.5 is large, and the intensity ratio is a highly sensitive function of kT_e. However if $kT_e >> E(z+1,q,\infty) - E(z,p,\infty)$, the intensity ratio is insensitive to temperature, and is a good diagnostic of the ionization of the plasma. Here, the separation between wavelengths of the observed transitions can be small, reducing the need for accurate intensity calibration of the spectrograph.

2.2.2 CRITERIA FOR LTE

For complete LTE to hold in a stationary, homogeneous plasma, the radiative decay rate must be much less that the collisional de-excitation rate for all the transitions in the ion. McWhirter (1965) gives the following criterion for complete LTE to hold within 10%:

$$N_e > 1.6 \times 10^{12} T_e^{1/2} E^3 \qquad 2.6$$

where E is the largest energy gap in the ion (For H-like and He-like ions, this is usually the $1^1S - 2^1P$ transition). However it is possible to partially satisfy LTE

in an ion if all the energy levels above a certain value are in LTE with higher ionization stages. (Griem 1964) In this case, the criterion 2.6 can be relaxed to :

$$N_e > 7 \times 10^{18} \frac{z^7}{n^{17/2}} \left(\frac{kT_e}{z^2 E_H} \right)^{1/2} \text{ cm}^{-3} \qquad 2.7$$

for a level n. The criteria can be further relaxed if the plasma is optically thick, which has the effect of reducing the importance of radiative decay. However any line intensities calculated assuming LTE must then be adjusted to take account of absorption. This will be elaborated in section 2.6. The minimum densities at which LTE holds are listed for various plasmas in table 2.1.

LTE can also be applied to transient plasmas provided that the time taken to reach equilibrium is sufficiently short for LTE to be established in the plasma. For partial LTE to hold **above** level n, the time t taken to reach equilibrium is (Griem 1964) :

$$t = 4.5 \times 10^7 \frac{z^3}{n^4 n_e} \frac{kT_e}{z^2 E_H} \exp \frac{2z^2 E_H}{n^3 kT_e} \text{ seconds} \qquad 2.8$$

The time for various different plasmas to reach equilibrium is listed in table 2.1.

Table 2.1 Criteria for LTE to hold in various plasmas (H-like)

Criteria	Carbon		Oxygen		Neon	
Max n_e /cm^{-3}	50 eV	100 eV	50 eV	100 eV	50 eV	100 eV
to level 3	5.5×10^{19}	7.8×10^{19}	3.1×10^{20}	4.4×10^{20}	1.2×10^{21}	1.7×10^{21}
to level 4	4.7×10^{18}	6.8×10^{18}	2.7×10^{19}	3.8×10^{19}	1.0×10^{20}	1.4×10^{20}
to level 5	7.2×10^{17}	1.0×10^{18}	4×10^{18}	5.7×10^{18}	1.5×10^{19}	2.2×10^{19}
time to reach equilibrium in level 3 /s	7×10^{-15}	4.6×10^{-15}	1.6×10^{-15}	5.7×10^{-16}	6.7×10^{-16}	2.4×10^{-16}

2.2.3 NON-LTE MODELS

The LTE model can only be fully satisfied at very high electron densities, so although partial LTE can be applied for many situations in high density, high temperature plasmas, a more complete model is needed in order to describe a spectrum. The coronal model is used at low densities, and assumes that collisional excitation is balanced purely by radiative decay or recombination. There is thus a gap between the region of validity of LTE and the region of validity of the coronal model, where the radiative and collisional rates are equally significant. Here, the collisional-radiative model must be used, which calculates the effect of both radiative and collisional processes. A graph of the ionization balance of oxygen in the collisional-radiative model is shown in figure 2.1, showing the region where each of the three models are valid.

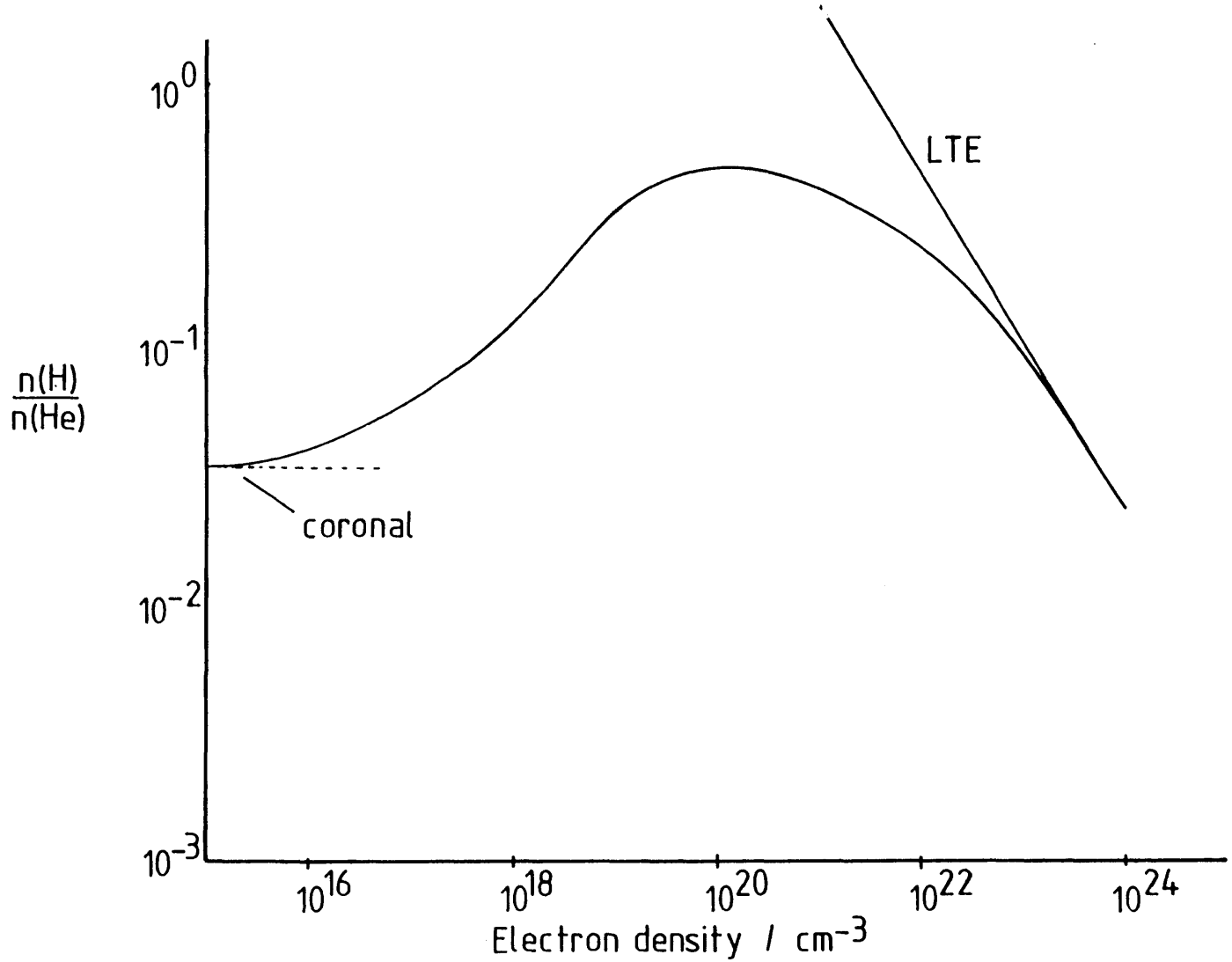


FIGURE 2.1 IONIZATION OF OXYGEN IN COLLISIONAL-RADIATIVE EQUILIBRIUM AT 150eV

2.2.3.1 THE CORONAL MODEL

The coronal model is most useful in low density, high temperature plasmas. It assumes that there is a balance between collisional excitation or ionization and radiative decay or recombination, with other collisional processes being insignificant. Hence unlike LTE, a full knowledge of the atomic data is needed in order to solve the model. It is assumed that the plasma is in a steady state, and is optically thin.

The ionization of the plasma can be expressed as (McWhirter 1965):

$$\frac{n(z\ ,g)}{n(z+1,g)} = \frac{\alpha(T_e,z+1,g)}{S(T_e,z,g)} \qquad 2.9$$

where α is the radiative recombination coefficient and S the collisional ionization coefficient. Expressions for α and S have been calculated by several authors and are summarized in McWhirter (1965). Use of these give :

$$\frac{n(z,g)}{n(z+1,g)} = 7.87 \times 10^{-9} E(z,g)^2 \left(\frac{E(z,g)}{kT_e}\right)^{3/4} \exp\frac{-E(z,g)}{kT_e} \qquad 2.10$$

This is thus a sensitive function of electron temperature when $E(z,g) > kT_e$.

The excited state populations of an ion in coronal equilibrium are given by :

$$n_e\, n(z,g)\, X(T_e,g,p) = n(z,p) \sum_q A(p,q) \qquad 2.11$$

where X(Te,g,p) is the collisional excitation rate. This has been calculated to be (see for example McWhirter, 1965) :

$$X(T_e,g,p) = 7.89 \times 10^{-6}\, g\, \frac{f(p,q)}{E(p,q)\, kT_e^{1/2}} \exp\left(\frac{-E(p,q)}{kT_e}\right) \qquad 2.12$$

where g is the effective mean Gaunt factor, calculated by Seaton (1962) to be 0.2. The intensity of a line in coronal equilibrium will thus be :

$$I(p,q) = \int n_e n(z,g)\, 7.89 \times 10^{-6}\, g\, \frac{f(p,q)}{kT_e^{1/2}} \exp \frac{-E(p,q)}{kT_e} \qquad 2.13$$

where the integral is over the volume of the plasma.

The coronal model is valid provided the sum of the radiative decay rates A(p,q) exceed the collisional de-excitation rate of any level, $n_e X(T_e,p,g)$. This can only be true for levels below a certain value at a given electron density.

2.2.3.2 THE COLLISIONAL-RADIATIVE MODEL

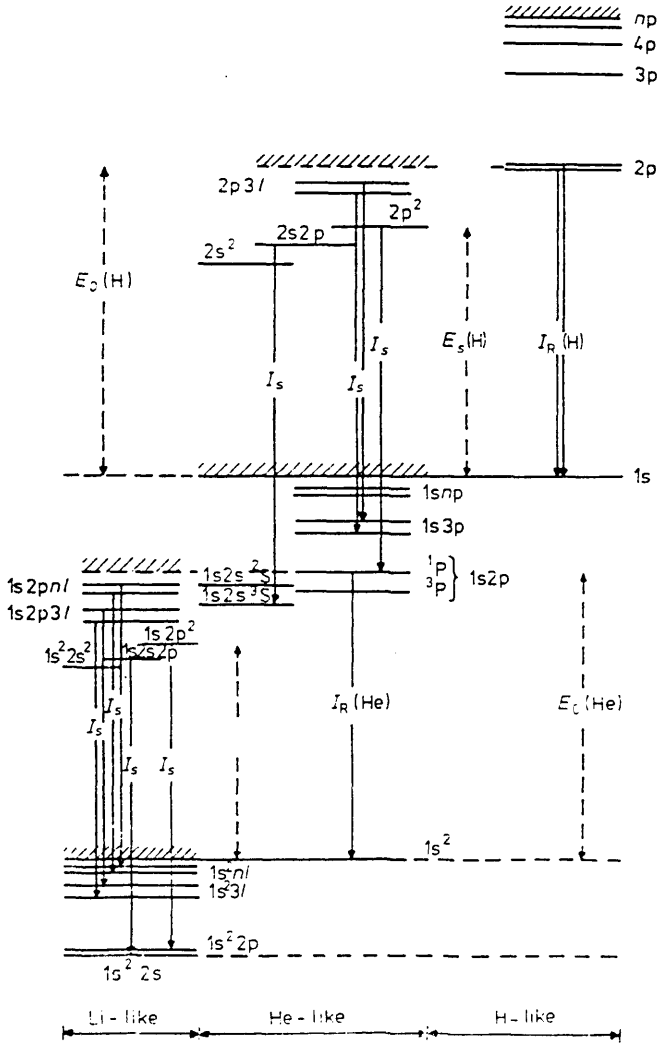
The collisional-radiative equilibrium model includes collisional excitation or ionization, collisional de-excitation or recombination, and radiative decay or recombination. Again it is assumed that the plasma is optically thin (thus neglecting radiative excitation or ionization). The population of any level is written as a differential equation in terms of all the other levels in the ion. This equation can be simplified somewhat, due to the fact that above a certain level, the populations can be described by an LTE model. Hence any processes involving levels above this limit can be replaced by the equivalent process in the LTE model. The model was first solved for hydrogenic ions by Bates (1962), and has subsequently been solved for non-hydrogenic ions by Duston and Davies (1980) for H-like, He-like and Ne-like ions; and by Lee et al (1984) for excited states of H-like, He-like, Li-like ions and ground states of the other ions. This latter model is outlined in section 2.4.

2.3 INTENSITIES OF DIELECTRONIC SATELLITE LINES

Dielectronic satellite lines most commonly result from the radiationless capture of a free electron by an excited ion, with z electrons to give a doubly excited ion with z+1 electrons in a bound state lying above the ionization limit of the ion. The radiative decay of this state to a

lower, singly excited state gives rise to a satellite line. These satellite lines lie on the long wavelength side of the resonance lines of the original z+1 electron ion. The most important dielectronic satellites are due to transitions of the type 2pnl - 1snl in helium-like ions, and 1s2pnl - $1s^2$nl in lithium-like ions. They appear as satellite lines to the 2p - 1s and 1s2p - $1s^2$ transitions in hydrogenic and helium-like ions respectively. An energy level diagram of these satellites is given in figure 2.2.

FIGURE 2.2 ENERGY LEVELS OF HE-LIKE AND LI-LIKE DIELECTRONIC SATELLITES.
Reproduced from Dubau, Volonte (1980)



In addition to dielectronic recombination described above, the upper levels of the satellite lines can also be populated by excitation of an inner shell electron to a higher level. The doubly excited ion can decay by producing the satellites (radiative decay) or by the opposite of dielectronic recombination, known as autoionization, where a doubly excited ion emits an electron, forming a singly excited ion below the ionization limit. These processes are further discussed in section 2.3.2

Dielectronic satellites can be used for diagnosing plasmas in several ways. Gabriel et al (1969, 1972, 1975) showed that when dielectronic recombination is the dominant mechanism for populating the doubly excited levels, the intensity ratio of a satellite to the resonance line is a sensitive temperature diagnostic. This is further discussed in section 2.3.3. Jacobs and Blaha (1980) later showed that electron collisional transitions between doubly excited levels of lithium-like ions caused the relative intensities of the satellites themselves to be a sensitive density diagnostic (see section 2.3.4). Relative intensities of helium-like to lithium-like satellites can also give an independent estimate of the ionization of the plasma. (J. G. Lunney unpub)

Satellites have several advantages when used for diagnosing plasmas. Firstly, because the lower level of the

transition is an excited state, its population is much less than that of the ground state, and hence the satellite is more likely to be optically thin. Secondly, experimental evidence from time-resolved spectra in laser produced plasmas (Kilkenny et al unpub) indicates that satellite line radiation is usually produced during peak compression, and hence gives a good measure of the peak temperatures and densities. Taken together, the helium-like and lithium-like satellites can be used over a wide range of temperatures and densities, particularly if the spectral resolution is sufficient to resolve the two sets of satellites produced from the ^3P states. Finally, their proximity in wavelength to the resonance line reduces the necessity for good intensity calibration of the spectrograph.

The notation used in this thesis for the lithium-like dielectronic satellites was first introduced by Gabriel (1972). A list of the wavelengths, autoionization rates and transition probabilities is given in table 2.2 (taken from L. A. Vainstein, U. I. Safranova 1978) for carbon, oxygen, nitrogen and neon.

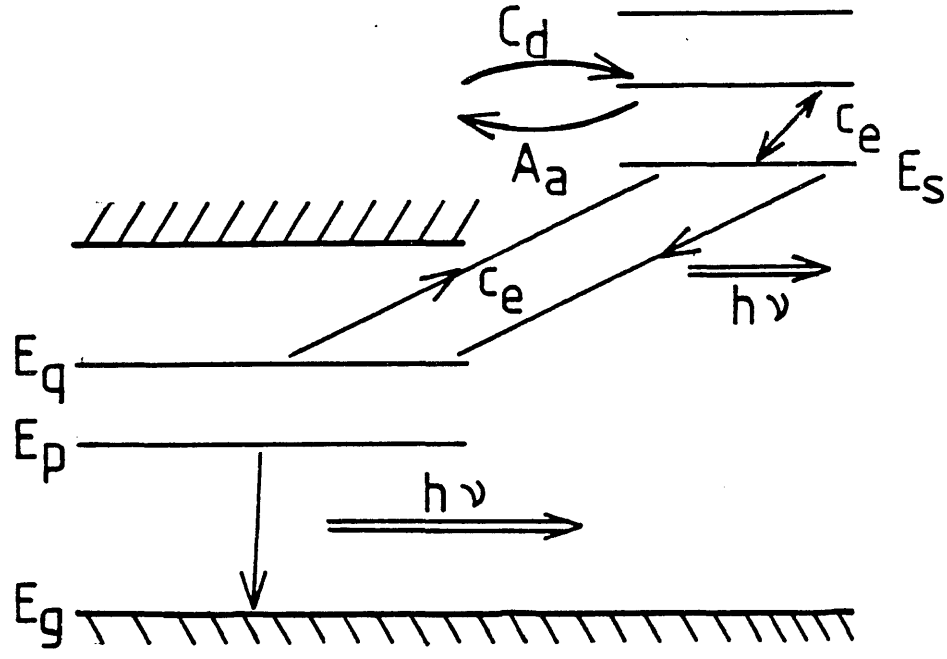


Figure 2.3 Processes involved in dielectronic satellite formation

2.3.1 POPULATIONS OF THE SATELLITE LEVELS

The doubly excited satellite levels can be populated and depopulated by 4 main processes, shown on figure 2.3 (Dubau, Volonte, 1980) :

(i) Dielectronic recombination : In this process, an ion captures an electron into an excited state, giving an ion with one less charge :

$$N(z,q) + e \rightarrow N(z-1,p) \qquad 2.14$$

The rate for this process is $n(z,g)\ n_e\ C_d$, where C_d is the dielectronic capture rate, and is determined using detailed balance from the in-

Table 2.2 Wavelengths, Radiative rates and Autoionizing rates for dielectronic satellites in Carbon, Oxygen and Neon λ in A;

Radiative rate A in s^{-1}: Autoionization rate Γ in 10^{13} s^{-1}

Transition	λ	$\tilde{q}$	A	Γ
Z=6				
R234-Y212	33732+2	000-0	810-1	000-0
R232-Y212	33737+2	000-0	810-1	000-0
F111-B133	33884+2	100-0	108-0	143+1
C133-A111	34312+2	225-0	753-1	202+2
F155-B335	34377+2	670-4	134-4	373+2
C335-A313	34526+2	337-0	709-1	135+1
C333-A313	34529+2	202-0	709-1	135+1
C331-A313	34530+2	673-1	709-1	135+1
F335-B333	34587+2	203-1	356-1	459-2
F335-B335	34588+2	220-1	106-0	459-2
F333-B333	34590+2	000-0	356-1	000-0
F333-B331	34590+2	000-0	475-1	000-0
F333-B335	34591+2	000-0	594-1	000-0
F331-B333	34591+2	244-3	142-0	244-3
F155-B133	34709+2	716+0	143-0	373+2
F335-B133	34925+2	491-4	984-5	459-2
F333-B133	34928+2	000-0	106-5	000-0
E111-B133	35576+2	301-1	301-1	347+2
Z=8				
R234-Y212	18965+2	000-0	256-0	000-0
R232-Y212	18970+2	000-0	256-0	000-0
C133-A313	18983+2	410-4	136-4	202+2
F111-B133	19039+2	290-0	356-0	155+1
C133-A111	19214+2	719+0	242-0	202+2
F155-B335	19236+2	102-2	204-3	373+2
C335-A313	19304+2	990+0	231-0	135+1
C333-A313	19307+2	594+0	231-0	136+1
C331-A313	19309+2	197-0	231-0	135+1
F335-B333	19333+2	910-1	116-0	215-1
F335-B335	19335+2	101-0	348-0	215-1
F333-B331	19336+2	000-0	155-0	000-0
F333-B333	19336+2	000-0	116-0	000-0
F331-B333	19338+2	141-2	465-0	142-2
F333-B335	19338+2	000-0	193-0	000-0
F155-B133	19393+2	230+1	467-0	373+2
F335-B133	19494+2	721-3	145-3	215-1
F333-B133	19497+2	000-0	181-4	000-0
F331-B133	19499+2	350-4	358-4	142-2
C333-A111	19546+2	387-4	129-4	136+1
E111-B333	19605+2	918-4	918-4	345+2
E111-B133	19771+2	982-1	985-1	345+2
Z=10				
F111-B333	12087+2	139-4	139-4	166+1
R234-Y212	12130+2	000-0	627+0	000-0
R232-Y212	12135+2	000-0	626+0	000-0
C133-A313	12136+2	366-3	122-3	202+2
F111-B133	12172+2	582+0	895+0	166+1
C133-A111	12260+2	174+1	599+0	202+2
F155-B335	12269+2	897-2	179-2	372+2
C335-A313	12305+2	202+1	578+0	135+1
C333-A313	12308+2	121+1	577+0	136+1
C331-A313	12310+2	405-0	577+0	135+1
F335-B333	12321+2	301-0	290-0	761-1
F335-B335	12323+2	349-0	867+0	761-1
F333-B331	12323+2	000-0	386-0	000-0
F333-B333	12324+2	000-0	269-0	000-0
F331-B333	12325+2	533-2	115+1	536-2
F333-B335	12326+2	000-0	482-0	000-0
F155-B133	12355+2	563+1	116+1	372+2
F335-B133	12409+2	619-2	126-2	761-1
F333-B133	12412+2	000-0	165-3	000-0
F331-B133	12414+2	301-3	319-3	536-2
C333-A111	12435+2	349-3	116-3	136+1
E111-B333	12463+2	859-3	859-3	344+2
E111-B133	12553+2	241-0	243-0	344+2

Transition	λ	$\tilde{q}$	A	Γ
Z=6				
R133-Y111	40279+2	000-0	904-1	000-0
F212-B232	40711+2	227-1	114-1	229+1
R335-Y111	40711+2	000-0	000-0	000-0
F212-B234	40713+2	461-1	233-1	229+1
R333-Y111	40714+2	000-0	299-5	000-0
C232-A212	40875+2	158-1	794-2	116+2
C234-A212	40875+2	306-1	766-2	116+2
K234-A212	41360+2	251-0	719-1	492-0
K232-A212	41361+2	126-0	716-1	520+0
F234-B232	41438+2	108-1	190-1	315-2
F234-B234	41440+2	122-1	993-1	315-2
F232-B232	41440+2	112-4	790-1	564-5
F232-B234	41442+2	112-4	393-1	564-5
S313-Y111	41464+2	000-0	000-0	000-0
F254-B232	41563+2	135-0	338-1	186+2
F254-B234	41565+2	239-1	599-2	186+2
F256-B234	41567+2	238-0	398-1	186+2
K436-A212	42148+2	000-0	000-0	000-0
E212-B232	43792+2	251-2	125-2	157+2
E212-B234	43794+2	498-2	249-2	157+2
Z=8				
R133-Y111	21603+2	000-0	333-0	000-0
F212-B232	21781+2	842-1	428-1	243+1
F212-B234	21783+2	175-0	907-1	243+1
R335-Y111	21796+2	000-0	000-0	000-0
R333-Y111	21799+2	000-0	549-4	000-0
C234-A212	21841+2	111-0	278-1	116+2
C232-A212	21841+2	615-1	308-1	116+2
K234-A212	22024+2	697+0	276-0	472-0
K232-A212	22025+2	365-0	273-0	551+0
F234-B232	22062+2	496-1	698-1	150-1
F234-B234	22064+2	580-1	382-0	150-1
F232-B232	22065+2	119-3	303-0	597-4
F232-B234	22067+2	119-3	149-0	597-4
S313-Y111	22095+2	000-0	000-0	000-0
F254-B232	22125+2	523+0	131-0	186+2
F254-B234	22127+2	800-1	200-1	186+2
F256-B234	22129+2	902+0	151-0	186+2
F436-B234	22330+2	948-4	159-4	201-2
F434-B234	22331+2	416-4	119-4	814-4
K436-A212	22371+2	000-0	000-0	000-0
K434-A212	22373+2	288-4	970-5	282-4
E212-B232	23028+2	954-2	477-2	156+2
E212-B234	23031+2	187-1	936-2	156+2
Z=10				
R133-Y111	13447+2	000-0	892+0	000-0
F212-B232	13536+2	215-0	112-0	253+1
F212-B234	13539+2	462-0	254-0	253+1
R335-Y111	13548+2	000-0	000-0	000-0
R333-Y111	13551+2	000-0	525-3	000-0
C234-A212	13564+2	280-0	705-1	117+2
C232-A212	13565+2	174-0	878-1	115+2
K234-A212	13652+2	110+1	757+0	431-0
K232-A212	13654+2	663+0	740+0	600+0
F234-B232	13672+2	167-0	177-0	549-1
F232-B232	13675+2	635-3	832+0	318-3
F234-B234	13675+2	208-0	105+1	549-1
F232-B234	13678+2	635-3	401-0	318-3
S313-Y111	13697+2	000-0	000-0	000-0
F254-B232	13707+2	146+1	372-0	186+2
F254-B234	13710+2	171-0	429-1	186+2
F256-B234	13711+2	242+1	412-0	186+2
F432-B232	13819+2	430-4	708-4	309-4
F436-B234	13819+2	969-3	165-3	764-2
F434-B234	13820+2	363-3	115-3	429-3
K436-A212	13833+2	000-0	000-0	000-0
K434-A212	13835+2	239-3	101-3	145-3
K432-A212	13836+2	627-4	410-4	132-3
E212-B232	14160+2	261-1	130-1	155+2
E212-B234	14163+2	500-1	250-1	155+2

A: $1s2s$ B: $1s2p$ C: $2s2p$ E: $2s^2$ F: $2p^2$
234, 212, etc.: Values of $2S+1$, $2L+1$, $2J+1$

R: $2p$ Y: $1s$ R234–Y212 means $2p^2P_{3/2}$–$1s^2S_{1/2}$

A: $1s^22s$ B: $1s^22p$ C: $1s(2s2p^1P)$ K: $1s(2s2p^3P)$
133, 111, etc.: Values of $2S+1$, $2L+1$, $2J+1$

E: $1s2s^2$ F: $1s2p^2$ R: $1s2p$ S: $1s2s$ Y: $1s^2$
R133–Y111 means $1s2p\,^1P_1$–$1s^2\,^1S_0$

Reproduced from Vainstein & Safranova (1978)

verse process of autoionization :

$$C_d = A_a \frac{4\pi^{3/2} a_o^3 \, g(z-1,p)}{T^{3/2} g(z,g)} \exp \frac{-(E(z-1,p) - E(z,g))}{kT_e} \qquad 2.15$$

(ii) Autoionization : This is the inverse process of dielectronic capture. It is determined by the autoionizing rate A_a. Values of A_a are given by several authors (eg Vainstein & Safranova 1978; Seely 1981), and are tabulated in table 2.2.

(iii) Radiative decay : Here, the autoionizing level emits a photon and decays to a lower lying state:

$$N(z,p) \rightarrow N(z,q) + h\nu \qquad 2.16$$

The radiative rate A_r is tabulated in table 2.2 for several satellite transitions.

(iv) Inner shell excitation : At higher electron densities, a doubly excited level may also be populated by collisional excitation from a lower level :

$$N(z,g) + e \rightarrow N(z,p) + e \qquad 2.17$$

The rate for this is $n(z,g)n_e C_e$ where C_e is the excitation coefficient. It is less important

than dielectronic recombination in He-like ions, as it needs 2 electrons to be simultaneously excited, whereas in Li-like ions, there need only be one excitation.

An alternative process is :

$$N(z,s) + e^- \rightarrow N(z,s') + e^- \qquad 2.18$$

namely electron induced transitions between the satellite levels. This is important for all satellite levels as it depends on n_e. This is further discussed in section 2.3.4.

There are two basic ways in which the dielectronic satellites can be used for plasma diagnostics. The first uses their intensity relative to a resonance line in order to deduce the electron temperature; and the second uses the relative intensities of the satellites themselves in order to deduce the electron density.

2.3.2 SATELLITE / RESONANCE LINE INTENSITY RATIOS

At low densities both inner shell excitation and collisional redistribution among the satellite levels can be ignored in calculating the satellite intensity. Thus the intensity I_s of the satellite will then be determined by

dielectronic recombination, autoionization and radiative decay, giving : (Gabriel, Paget, 1972)

$$I(s,q) = n(z+1,g) n_e C_d h\nu \frac{A_r}{A_a + A_r} \qquad 2.19$$

substituting for the capture rate C_d from equation 2.15 :

$$I(s,q) = n(z+1) n_e A_a 4\pi a_o^3 \frac{g(s)}{g(z,g)} \frac{A_r}{A_a + A_r} h\nu \exp \frac{-E_s}{kT_e} \qquad 2.20$$

where $E_s = E(z,s,p) - E(z+1,g)$: the energy of the upper satellite level relative to the ground state of the next higher ionization stage.

The intensity I(p,g) of a resonance line in coronal equilibrium is given by equation 2.13. This intensity is proportional to the electron density. As I(s,q) is also proportional to the electron density, the intensity ratio is density independent, and depends only on the electron temperature, scaling as :

$$\frac{I(s,q)}{I(p,g)} \propto \frac{1}{T_e} \exp \frac{(E(p,g) - E_s)}{kT_e} \qquad 2.21$$

This method of finding kT_e is useful provided that $E(p,g) - E_s \sim kT_e$.

In high density plasmas such as those found in the gas-

puff z-pinch, the resonance line is often optically thick, thus invalidating this method. One solution to this is to use one of the higher order resonance lines, which is more likely to be optically thin, and is also in LTE. The intensity of a resonance line in LTE is:

$$I(p,g) = A(p,g)h\nu\, n(z,g)\, \frac{g(p)}{g(g)}\, \exp\frac{-E(z+1,p,g)}{kT_e} \qquad 2.22$$

Now relating n(z,g) to n(z+1,g) using Saha's equation :

$$I(p,g) = A(p,g)h\nu(p,g)n(z+1,g)n_e\, \frac{1}{2}\left(\frac{2\ mkT_e}{h^2}\right)^{-3/2} \frac{g(z,p)\ g(p)}{g(z+1,g)\ g(z+1,g)} \exp\frac{-E(z,p,\ )}{kT_e} \qquad 2.23$$

and hence the intensity ratio can be written :

$$\frac{I(s,q)}{I(p,g)} = \frac{h\nu(s,q)g(z,s)A_r(z,s,q)}{h\nu(p,g)g(z,p)A_r(z,p,g)A_a + A_r}\, \frac{A_a}{}\, \exp\frac{E_s - E(p,\infty)}{kT_e} \qquad 2.24$$

This is again a useful temperature diagnostic if $E_s - E(p,\infty) \sim kT_e$.

The ionization of the plasma can be obtained from the ratio of a helium-like satellite to a lithium-like satellite (Lunney,unpub) :

$$\frac{I(He)}{I(Li)} = \frac{h\nu(He)\,n(H,g)\,g(He,g)\,g(He,j)\,A_r(He,j)\,A_a(He,j)}{h\nu(Li)\,n(He,g)\,g(H,g)\,g(Li,j)\,A_r(Li,j)\,A_a(Li,j)} \qquad 2.25$$

$$\frac{A_a(Li,j) + A_r(Li,k,j)}{A_a(He,j) + A_r(Li,k,j)} \exp \frac{-E(He,j) - E(Li,j)}{kT_e}$$

2.3.3 RATIO OF THE SATELLITE INTENSITIES

At high electron densities, it may no longer be possible to ignore either the effect of inner shell excitation or of electron collisional redistribution of the doubly excited level populations described in section 2.3.2. Jacobs and Blaha (1980) showed that this would be particularly the case for the 'a-d' satellites to the helium-like 2^1P - 1^1S line, which are metastable to autoionization. The ''jkl' satellite intensities however, is determined largely by dielectronic recombination, due to its high autoionization rate. Hence the ratio of these satellites will be a sensitive function of the effect of collisional redistribution, and hence of the electron density. In practise, it is difficult to resolve the 'a-d' satellites from the 'qr' satellites. These 'qr' satellites however, are also affected by electron collisions, but to a lesser extent. The ratio 'ad' + 'qr' / 'jkl' is thus used in practise, and this is graphed for oxygen in figure 2.4.

Vinogradov et al (1977) and Seely et al (1981) showed that a similar situation exists for the helium-like 2s2p (^3P) states and the $2p^2$ (^3P) states, where the latter states

FIGURE 2.4 RATIO $\frac{AD + QR}{JKL}$ FOR OXYGEN

calculated from Lee Whitten Strout (1984)

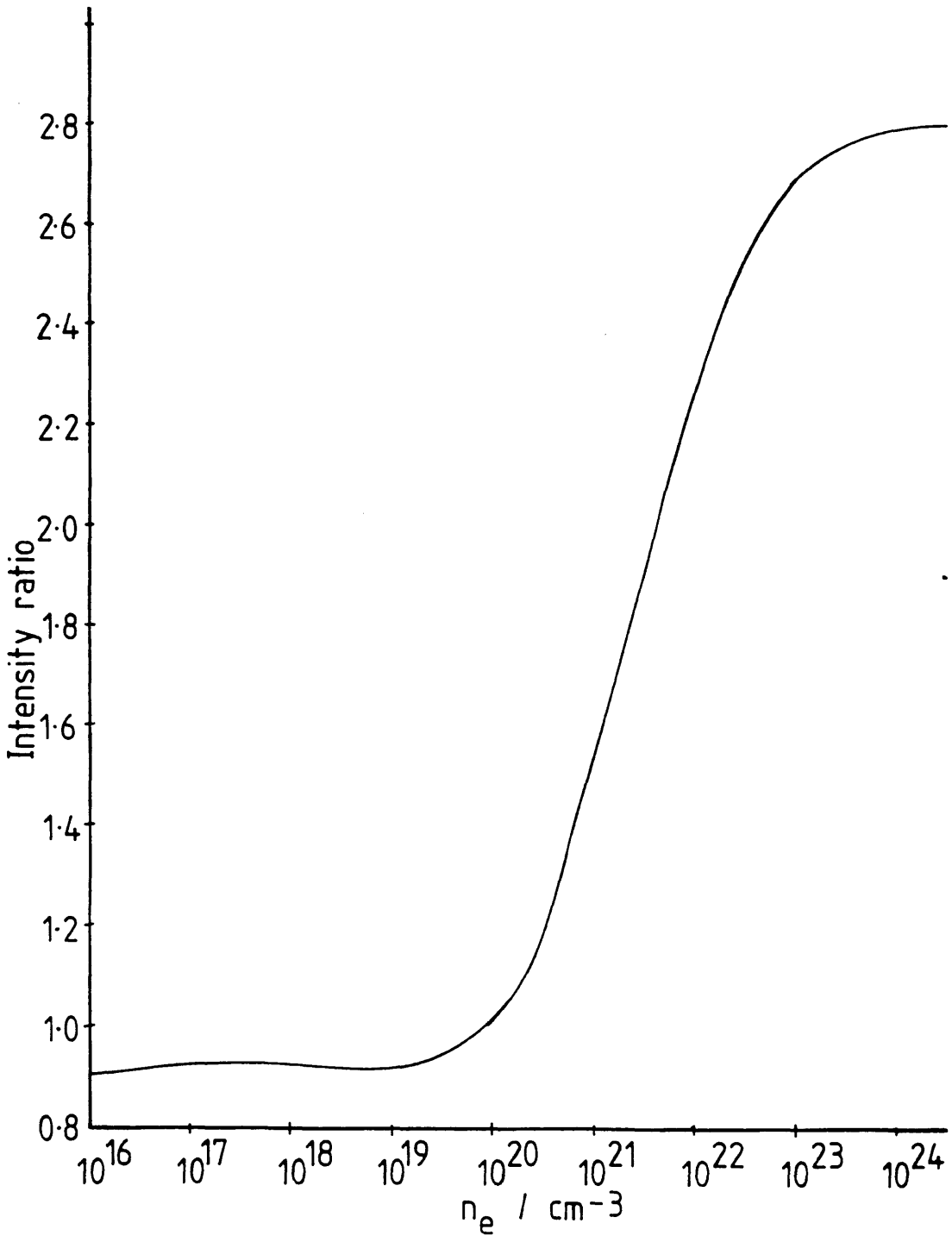
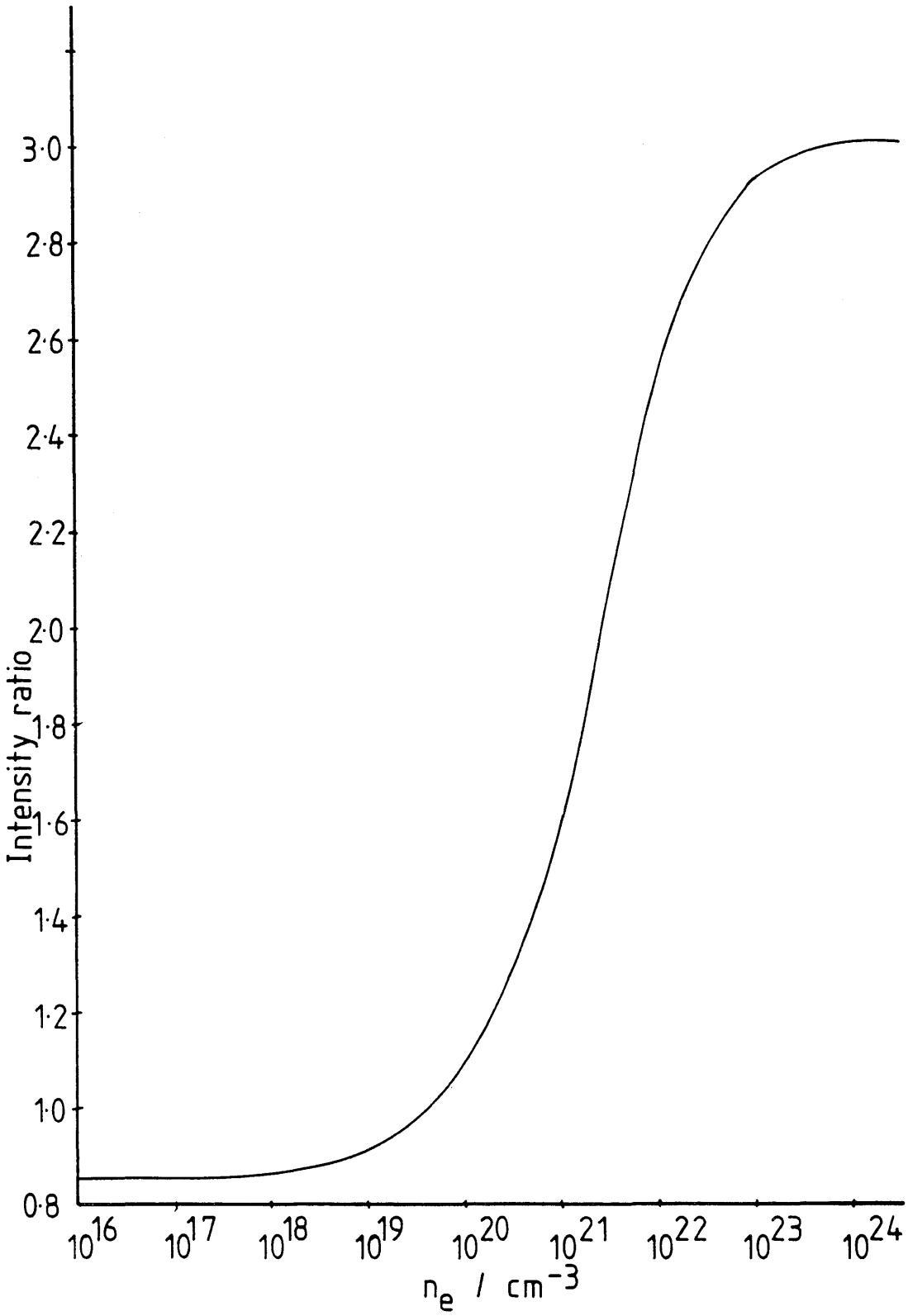


Figure 2.5 Intensity ratio $\frac{2s2p(^3P)-1s2s \; + \; 2p^2(^3P)-1s2p}{2p^2(^1D)-1s2p}$

calculated from Lee Whitten Strout (1984)



are affected by collisions. At higher densities however, both these states are collisionally populated, and the more useful ratio is :

$$\frac{((2s2p\ (^3P) - 1s2s\ (^3S) + 2p^2\ (^3P) - 1s2p(^3P))}{(2p^2(^1D) - 1s2p(^1P)} \qquad 2.26$$

This ratio is graphed for oxygen in figure 2.5.

2.4 THE COLLISIONAL-RADIATIVE MODEL AND INTERPRETATION OF OBSERVED INTENSITIES

In the gas-puff z-pinch, the densities and temperatures lie between the values for which the coronal model is valid, and those where LTE is valid. For interpreting most of the intensities, a collisional-radiative model must thus be used. The model used in this thesis is by Lee et al (1984). This calculates the level populations of the ground state and 23 excited states of hydrogenic and helium-like ions. Also included are the major autoionizing levels which give rise to the dielectronic satellites lines. The levels included in the code are listed in table 2.3. In calculating the level populations, account is taken of collisional excitation and de-excitation; ionization and dielectronic recombination; radiative decay and recombination; and autoionization. Again the plasma is assumed to be optically thin.

Ion State	Spectroscopic Specification	Comment	Source Number for Reference
Be-like ion	Ground States		Kelly and Harrison[20]
Li-like	$1s^2 2s\ ^2S$	ground state	
	$1s^2 2p\ ^2P$	excited state	Clark et al.[21]
	$1s2s^2\ ^2S$	mixed; auto-ionizing (OP)	Gabriel[22]
	$1s2p(^1P)2s\ ^2P$	mixed; auto-ionizing (QR)	Gabriel[22]
	$1s2p(^1P)2s\ ^2P$	mixed; auto-ionizing (ST)	Gabriel[22]
	$1s2p^2\ ^2D$	mixed; auto-ionizing (KL)	Gabriel[22]
	$1s2p^2\ ^2P$	mixed; auto-ionizing (ABCD)	Gabriel[22]
	$1s2p^2\ ^2S$	mixed; auto-ionizing (MN)	Gabriel[22]
He-like	$1s^2\ ^1S$	ground state	
	$1s2s\ ^3S$		extrapolation
	$1s2s\ ^1S$	dipole-forbidden	Clark et al.[21]
	$1s2p\ ^3P$	intercombination	
	$1s2p\ ^1P$	resonance	Scofield[23]
	$1s3\ell$	lumped state	Scofield[23]
	$1s4\ell$	lumped state	Scofield[23]
	$1s5\ell$(etc)	lumped state	Scofield[23]
	$2s^2\ ^1S$	Autoionizing	Vainshtein and Safranova[6]
	$2s2p\ ^3P$	Autoionizing	Vainshtein and Safranova[6]
	$2p^2\ ^3P$	Autoionizing	Vainshtein and Safranova[6]
	$2p^2\ ^1P$	Autoionizing	Vainshtein and Safranova[6]
	$2p^2\ ^1S$	Autoionizing	Vainshtein and Safranova[6]
	$2s2p\ ^1P$	Autoionizing	Vainshtein and Safranova[6]
Hydrogenic	n = 1 through 5	Lumped	Scofield[23]

Table 2.3 Levels included in the Collisional-Radiative Code from Lee Whitten Strout (1984)

In calculating the intensities, A-values and wavelengths for the satellites were taken from Vainstein and Safranova (1978), and those for the resonance lines were either extrapolated for H-like ions, or taken from Wiese, Smith and Glennon (1966). In calculating the electron temperature and ionization, high n resonance lines were taken to minimize the effects of opacity. The intensities calculated assuming LTE (equations 2.4, 2.5 and 2.13) will be compared with those using the model described above in chapter 5.

In order to obtain n_e, the ratios of the satellites were found by fitting the experimental satellite feature in the following manner. The level populations were first multiplied by the radiative rates and a gaussian instrument

profile centred around the listed wavelength of the line. The resulting theoretical satellite spectrum was then compared with the experimental spectrum, and the density varied until a good fit was obtained. The quality of fit Q was quantified using a least squares technique :

$$Q = \frac{(I(expt) - I(theor))^2}{(I(theor))^2} \qquad 2.27$$

Q varied between 0.01 for a good fit, and 0.1 for a poorer fit. The results were plotted out using the SIMPLE graphics package (ICCC bulletin 1982). All the calculations were carried out on a Cyber 855 computer.

In interpreting the line intensities, it was assumed that the plasma was optically thin, homogeneous and time independent. The assumption of opacity can be easily checked using the methods described in the following section on opacity broadening. However the assumptions of homogeneity and time independence are less easy to verify, as none of the spectra are temporally resolved, and few are spatially resolved. The theories used calculate the equilibrium values of intensities at each electron density and temperature. However this assumption is the least artificial assumption that can be made without having a good model of the time history of the plasma.

2.5 CONTINUUM INTENSITIES

Soft x-ray continua are formed by two different processes. Bremsstrahlung is formed by the scattering of free electrons by ions. The wavelength of the emission depends on the electron temperature, and the intensity upon the x-ray emission. (see equations 1.1 and 1.2) The recombination continuum is formed by the recombination of an electron and a free ion, and is thus formed at wavelengths at, and below that corresponding to the ionization limit of the final ion. Both types of continua are useful for diagnosing the electron temperature of a plasma as they obey:

$$I(\nu) \propto \exp(-h\nu/kT_e) \qquad 2.28$$

and are thus useful if $h\nu \sim kT_e$. They are rarely affected by opacity and have the added advantage that they are usually formed during the hottest phase of the plasma, due to the high energy needed to ionize a highly charged ion.

2.6 LINE BROADENING PROCESSES

There are several processes that can cause the broadening of spectral lines in a plasma. The most important are :

(i) Natural broadening

(ii) Doppler broadening.

(iii) Stark broadening.

(iv) Opacity broadening.

(v) Instrumental broadening.

Each of these processes is considered in the following sections.

2.6.1 NATURAL AND DOPPLER BROADENING

A transition occurring in an isolated motionless atom will be broadened by natural broadening due to the finite lifetime of the upper state of the transition. This causes an uncertainty in the energy of the transition of $\Delta E \simeq A\hbar$, where A is the transition probability. The resulting lineshape is a Lorentzian of half width half maximum (hence referred to as HWHM) $\Delta\nu_N$:

$$F(\nu) = \frac{\Delta\nu_N}{\pi} \frac{2}{2(\nu - \nu_o)^2 + 0.5\Delta\nu_N^2} \qquad 2.29$$

where ν_o is the central frequency of the transition.

If the ion is in motion however, it will also be subject to broadening by the Doppler effect. If the velocity of the ion is thermal, the lineshape will be :

$$F(\nu) = \frac{c}{\nu_o}\left(\frac{M}{2\pi kT}\right)^{1/2} \exp\left(\frac{-Mc^2}{2kT_e}\frac{(\nu-\nu_o)^2}{\nu_o^2}\right) \qquad 2.30$$

with a HWHM :

$$\Delta\nu_D = \nu_o\sqrt{\frac{2kT\ \ln 2}{Mc^2}} \qquad 2.31$$

where M is the mass of the ion.

For the ions and transitions in this thesis, typical transition probabilities will be 10^{12} s^{-1}, so the natural linewidth will be of the order of 2×10^{-5} A. The Doppler HWHM for the Lyman transition in carbon at a temperature of 60eV will be 6mA. The observed profiles however, have a HWHM of the order 50mA. Hence neither Doppler nor natural broadening contribute significantly to the observed profiles.

2.6.2 STARK BROADENING

In a high density plasma, the interaction of a radiating atom with the surrounding particles causes another source of spectral line broadening which frequently dominates all other broadening processes. This is generally known as pressure broadening, and can be divided into several different types, depending on the nature of the perturbing particles. The most important type in a plasma is Stark broadening, caused by the fluctuating electric field produced by the ions and electrons. The subject of Stark broadening has been widely reviewed (see for example Griem 1974 ; Baranger 1962).

There are several ways of treating the Stark broadening of spectral lines. The most widely used is Fourier decomposition theory. The usual treatment here is to use two approximations for the electric field. (Griem 1964). The first is the quasi-static approximation, which treats the electric field as being essentially static, and ignores the motion of the perturbers. It is most useful for considering the electric fields produced by the ions, and is valid when the frequency separation from line centre obeys

$$\Delta\omega >> v/p \qquad 2.32$$

where v is the velocity of the perturbers and p the impact parameter of a collision. Hence it is used in the line wings. Holtsmark (1919) produced an approximation for the field strength F_o due to the ion, neglecting all interactions :

$$F_o = 1.25 \times 10^{-9} N_e^{2/3} \qquad 2.33$$

and the field strengths used in practise are of the order $3F_o$. (see for example Tighe and Hooper 1977). The line wings then decay as $\lambda^{-5/2}$.

The second approximation is the impact approximation, and assumes that all the collisions are completed within the

lifetime of the upper level of the transition. It is thus valid when :

$$\Delta\omega \ll v/_p \qquad 2.34$$

(ie the line centre) and is mostly used for calculating the broadening due to electron impacts. For a Maxwellian electron distribution, the line profile near line centre is roughly Lorentzian in shape. More detailed calculations of the line profile have been published by Kepple and Griem (1978) and include both electron and ion broadening in the appropriate approximations. These profiles are the ones used in this thesis.

In hydrogenic ions, it is found that the electric fields not only broaden the lines, but shift the degenerate components of the lines. This causes the lines produced from even upper levels to have a triplet structure with a strong central unshifted component; and those from odd n upper levels to have two equal shifted components. The odd n levels are thus more sensitive to the electron density than the even n levels, as the level splitting contributes to the apparent broadening. Higher n levels are also affected more than low n levels, the line width roughly varying with n^2.

This splitting of the levels causes a problem if the electron density is estimated by measuring just the half

width. This is because the central component of the Lyα and the Lyγ lines is very narrow and insensitive to electron density. It is thus rarely resolved by a spectrograph which integrates the intensity over a much larger instrumental width. If the line is optically thick, it complicates the line profile further by reducing the intensity of the central spike. These problems are overcome in this thesis by fitting the line profiles of a whole line series, taking into account opacity and instrumental broadening as well as Stark broadening.

2.6.3 EFFECT OF OPACITY

All the equations in the preceding sections have assumed that radiation emitted from the plasma will escape without interacting with any particles. However this is rarely the case in high density plasmas, especially at the centre of the strongest resonance lines. In order to calculate the effect of re-absorption of radiation, it is necessary to relate the local emissivities $\varepsilon(\nu)$ and absorption coefficients $k(\nu)$ to the observed intensity. This is done with the equation of radiative transfer (de Michelis and Mattioli 1981) :

$$\frac{dI(\nu)}{d\tau} = S(\nu) - I(\nu) \qquad 2.35$$

where $S(\nu)$ is the source function, defined by :

$$S(\nu) = \varepsilon(\nu) \; / \; k(\nu) \qquad 2.36$$

$\tau(\nu)$is the optical depth defined by :

$$\tau(\nu) = \int k(\nu) \; dl \qquad 2.37$$

A plasma with an optical depth of less than 1 is defined to be optically thin, and one with an optical depth greater than 1 is optically thick. A general solution of this equation is difficult to obtain, because re-absorption of the radiation in a optically thick plasma alters the level populations, thus invalidating the equilibrium model used. However for a homogeneous, steady state slab of plasma in LTE, the source function approximates to a blackbody function $B(\nu)$, and the solution is (de Michelis & Mattioli 1981):

$$I(\nu) = B(\nu) \; (\; 1-e^{-\tau(\nu)} \;) \qquad 2.38$$

$$B(\nu) = \frac{2h\nu^3}{c^2} \left[\exp\left(\frac{h\nu}{kT_e}\right) - 1 \right]^{-1} \qquad 2.39$$

The optical depth of a slab of plasma of thickness 1 is (Thorne 1974) :

$$\tau(\nu) = \frac{e^2}{4\varepsilon_o mc} f \; N_i \; 1 \; L(\nu) \qquad 2.40$$

where f is the absorption oscillator strength, N_i the

density of ions in the lower state, and $L(\nu)$ the line shape. This solution is the same as that for a sphere of diameter 1.5 x 1 (Kilkenny et al 1980).

This solution will be valid provided that the source function is independent of frequency. This is least likely to be valid in the centre of the Lyman profile. Kilkenny et al (1980) showed that the effect of this was to create a trough in the centre of the line which, when convolved with the instrument profile effectively broadened the line still further.

2.6.4 INTERPRETATION OF OBSERVED LINE PROFILES

In interpreting the line profile observed, the following procedure was adopted :

1 Optically thin Stark broadened profiles of Lyman lines of carbon and oxygen were taken from Kepple and Griem (1978) where they are listed in terms of the reduced wavelength , given by :

$$\alpha = \frac{\Delta\lambda}{F_o} \qquad 2.41$$

$$S(\nu) = L(\nu) \frac{d\Delta\nu}{d\alpha} \qquad 2.42$$

where $\Delta\lambda$ and $\Delta\nu$ are the wavelength and frequency separation from line centre, and F_o is the

Holtsmark field strength given by equation 2.33. From these, the area normalized line profile $L(\nu)$ was calculated in terms of wavelength.

2 The area normalized line profile was substituted into equation 2.40 to calculate the opacity at each point in the line, and from this, the resulting intensity calculated using equation 2.38.

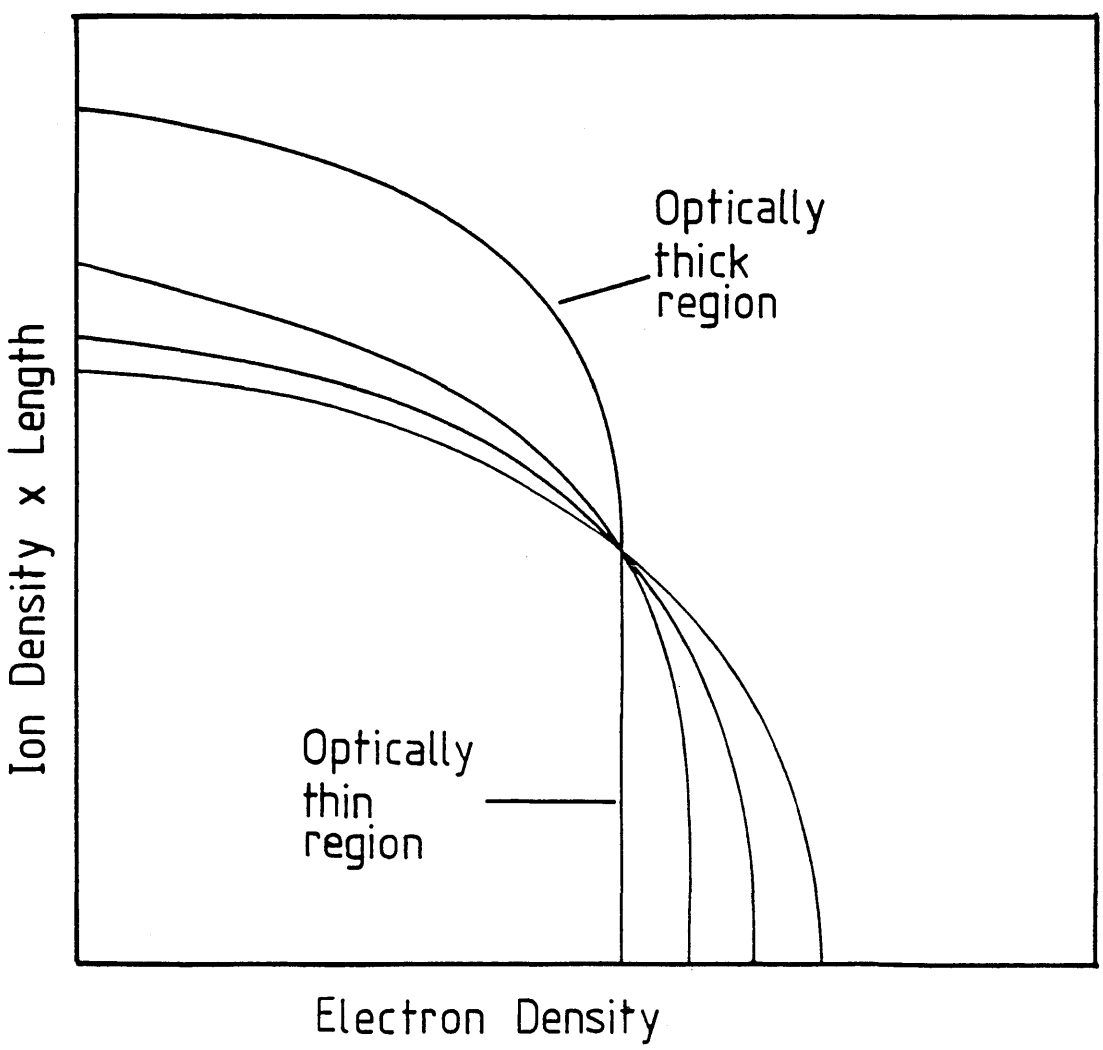
3 The optically thick line profile was then convolved with a gaussian instrument function and compared to the experimental profile. Again the quality of fit was determined using equation 2.27.

4 This process was repeated for a series of electron densities and ion density x length products, so obtaining a series of parameters where the lines fit best.

Examination of the optically thick line profile in equation 2.38 shows that it is a function both of the electron density and the ion density x length product (Kilkenny et al 1980). As the details of the line shape are not resolvable by the spectrograph used, it is found that there are a series of values of electron density and ion density x length for which a good fit is obtained. As higher order Lyman lines are more likely to be optically thin than

lower order lines, it is possible to plot a graph of the ion density x length product against electron density, each line representing the points at which a given Lyman line fits best. The shape of this should be as illustrated in figure 2.6. The plasma conditions at which the Lyman lines were formed can be deduced from the region where the lines on the graph intersect. This can be compared with the electron density from the satellites, and the expected ion density x length product from the known ionization of the plasma and the observed diameter from spatially resolved spectra.

FIGURE 2.6 IDEALIZED LINES OF BEST FIT FOR A LINE SERIES



2.7 CONCLUDING REMARKS

It is thus possible to get a good idea of the plasma conditions from the observed soft x-ray emission spectra. Although it is in principle possible to obtain a theoretical spectrum at one set of conditions, it must be remembered that the experimental plasma is neither homogeneous nor time independent, and hence comparison with the experimentally observed spectra will not always be possible. The different methods, used in chapter 5, for obtaining the plasma parameters are summarized in table 2.4.

Table 2.4 Different methods for finding kT_e and n_e

Method and equation number	Suitable lines	Parameter measured
Satellite/resonance line ratio 2.24	He-like, Li-like resonance lines $2p^2\ ^1D$, jkl satellites.	kT_e
Continuum slope 2.28	Recombination continuum	kT_e
Relative line intensities (in LTE) 2.5	H-like, He-like resonance lines	Ionization Bare/H-like
Relative line intensities (in Coronal) 2.13, 2.10	Any coronal line	Ionization kT_e
Satellite/satellite line ratio 2.25	$2p^2\ ^1D$ -1s2p jkl satellites	Ionization H / He-like
Relative satellite intensities. section 2.3.4	all He, Li-like satellites	n_e
Stark, Opacity broadening section 2.6.5	H-like resonance lines	n_e, n_i x l
Absolute line intensities 2.13	Any coronal line	n_e

CHAPTER 3 THE EXPERIMENT

3.1 INTRODUCTION

There are 5 basic criteria in choosing a spectrograph for soft x-ray spectroscopy :

(i) Wavelength range
(ii) Efficiency
(iii) Wavelength resolution
(iv) Spatial resolution
(v) Temporal resolution

The study of low z plasmas of high temperatures involves wavelengths from 10 Å up to about 50 Å. Crystal spectrographs are limited to wavelengths below 25 Å. This is because the Bragg equation for the dispersion of a crystal:

$$n\lambda = 2d \sin\theta \qquad 3.1$$

has no solution for wavelengths twice the interplane spacing d of the crystals. Although some organic crystals have interplane spacings as great as 50 Å, crystals of reasonable efficiency and resolution are limited to working below 25 Å (eg KAP). Hence a grazing incidence grating spectrograph was chosen for this work.

Gratings are restricted to working at grazing incidence in the soft x-ray region, due to the low reflectivity of most substances at normal incidence. There has been much progress recently in improving the efficiencies of spherical gratings working at grazing incidence, particularly with those of moderate resolutions. The efficiencies of gratings with 300 l/mm and 600 l/mm now approach 25% diffracted into the first order. However the efficiencies of higher resolution gratings remains low. Hence a better way to obtain good wavelength resolution is to use a larger radius grating such as the 5m radius gratings used in this thesis.

The optimum slit width S_{opt} for an error-free instrument is such that the beam diffracted by the slit fills the grating. This is given by :

$$S_{opt} = \lambda / \text{ f number} \qquad 3.2$$

where the f number is the angle of acceptance of the spectrograph. For an f number of 1/125, the optimum slit width in the soft x-ray region is then less than 1μm. As slit widths of this size are difficult to manufacture, most grazing incidence spectrographs are slit width limited.

Spatial resolution in a grazing incidence grating spectrograph is usually achieved by placing a cross-slit over the

main slit of the spectrograph. Hence the spatial resolution is determined by the size of this slit, which should be large enough to allow sufficient light for a well exposed spectrum. Temporal resolution is, at present impossible on a high resolution spectrograph, due to the poor efficiency of detectors. However for low wavelength resolution, flat field transmission gratings have been used with an x-ray streak camera, to obtain 20ps resolution for a spectrum from 0.1 - 1.5 keV (Ceglio et al, 1981). A wavelength scanning photon counting detector module has been made for the 5m spectrograph used in this theses (Mrowka, 1983). This is currently in use by G. S. I. Darmstadt on quasi-DC sources. However it requires a major effort on fast detectors (lns) before it could be used with the gas-puff z-pinch.

3.2 GEOMETRY OF ROWLAND CIRCLE SPECTROGRAPHS

For an ideal grazing incidence grating spectrograph, the wavelength λ of an observed transition can be found by the grating equation

$$n\lambda = d\,(\cos\alpha - \cos\beta) \qquad 3.3$$

where n is the order of diffraction from the grating, d is the grating spacing; α is the angle of incidence; and β the angle of diffraction. (see figure 3.1) The slit,

grating and image lie on a circle of radius equal to half the grating radius R, called the Rowland circle. Reference to the diagram shows that the angles of diffraction β and incidence α are:

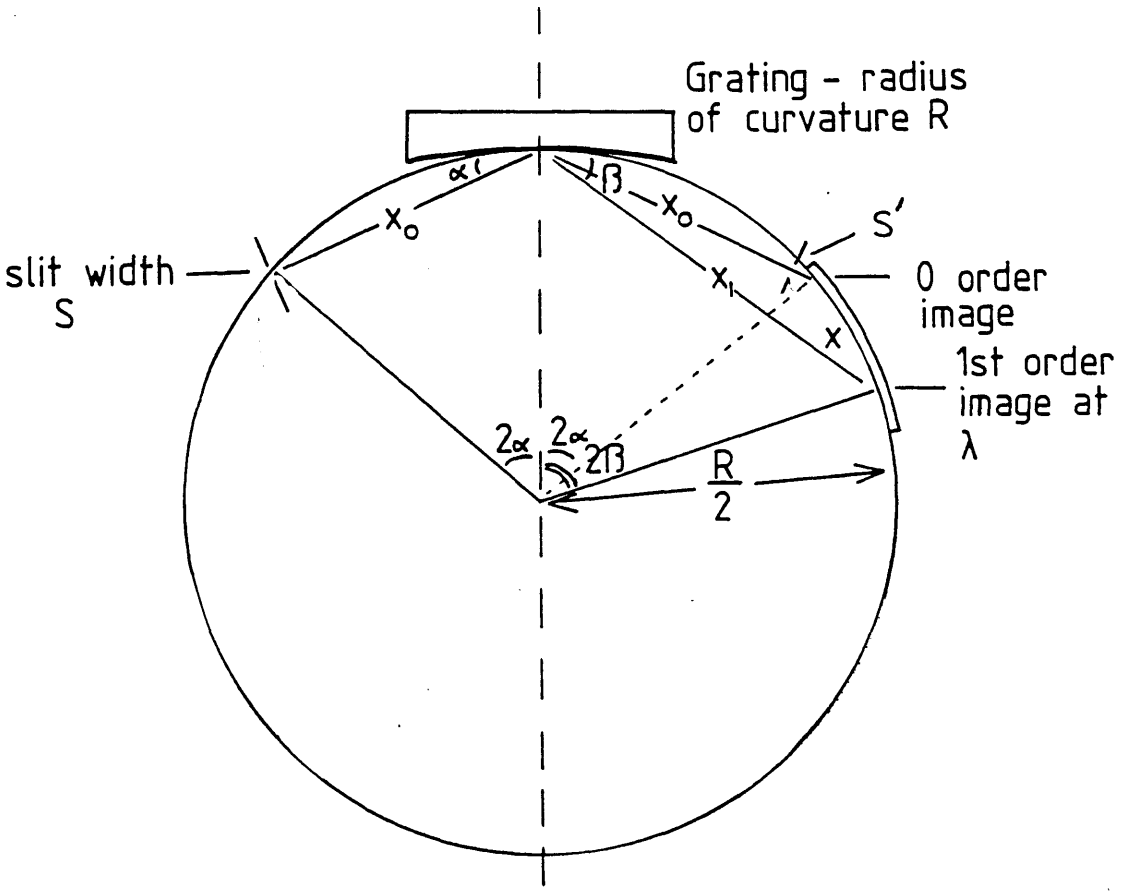


FIGURE 3.1 THE ROWLAND CIRCLE

$$\beta = \alpha + x/R \qquad 3.4$$

and

$$\alpha = x_o / R \qquad 3.5$$

where x is the distance between the observed line and the zero order. Differentiating equation 3.3 and using equation 3.4 gives the resolution of the spectrograph for a

given slit width:

$$\Delta\lambda = d \sin\beta \frac{\Delta x}{R} \qquad 3.6$$

Here, Δx is the width of the image of the line on the Rowland circle. Differentiating equation 3.3 with respect to α and β gives :

$$-d \sin\alpha d\alpha + d \sin\beta \; d\beta = 0 \qquad 3.7$$

Reference to figure 3.1 shows that :

$$d\alpha = \frac{S}{R \sin\alpha} \qquad 3.8$$

$$d\beta = \frac{S}{R \sin\beta} \qquad 3.9$$

and hence geometrical images have unit magnification. As the image is at an angle of β to the Rowland circle :

$$\Delta x = \frac{S}{\sin\beta} \qquad 3.10$$

Thus from equation 3.6

$$\Delta\lambda = \frac{S\, d}{R} \qquad 3.11$$

The practical limit on the resolution of the spectrograph

is also determined by how well the spectrograph is focused. Resolutions achieved will thus only be within a factor of 2 of this ideal case.

3.3 THE SPECTROGRAPH

The spectrograph is shown in figures 3.2 and 3.3. The spectrograph used was a 5m grazing incidence grating spectrograph manufactured by Grating Measurements Ltd, on loan from the Rutherford Appleton laboratory. The spectrograph was designed so that both the angle of incidence and the grating can be easily changed without the need for refocusing (however see section 3.4). It consists of a 1m long Meehanite beam with 2450mm radius rails on which modules for the slit, grating and photographic plate can be mounted (Speer 1976).

The angle of incidence can be determined using equation 3.5, and adjusted by moving the relative positions of the slit and grating. In order to do this with the minimum of adjustments, and retaining the line of sight to the source, the slit was placed on the fulcrum of the spectrograph's cradle. This was then moved up or down until the slit was aligned with the source. The back of the spectrograph was then adjusted each time the angle of incidence was changed, in order to keep the grating aligned with the slit and the source.

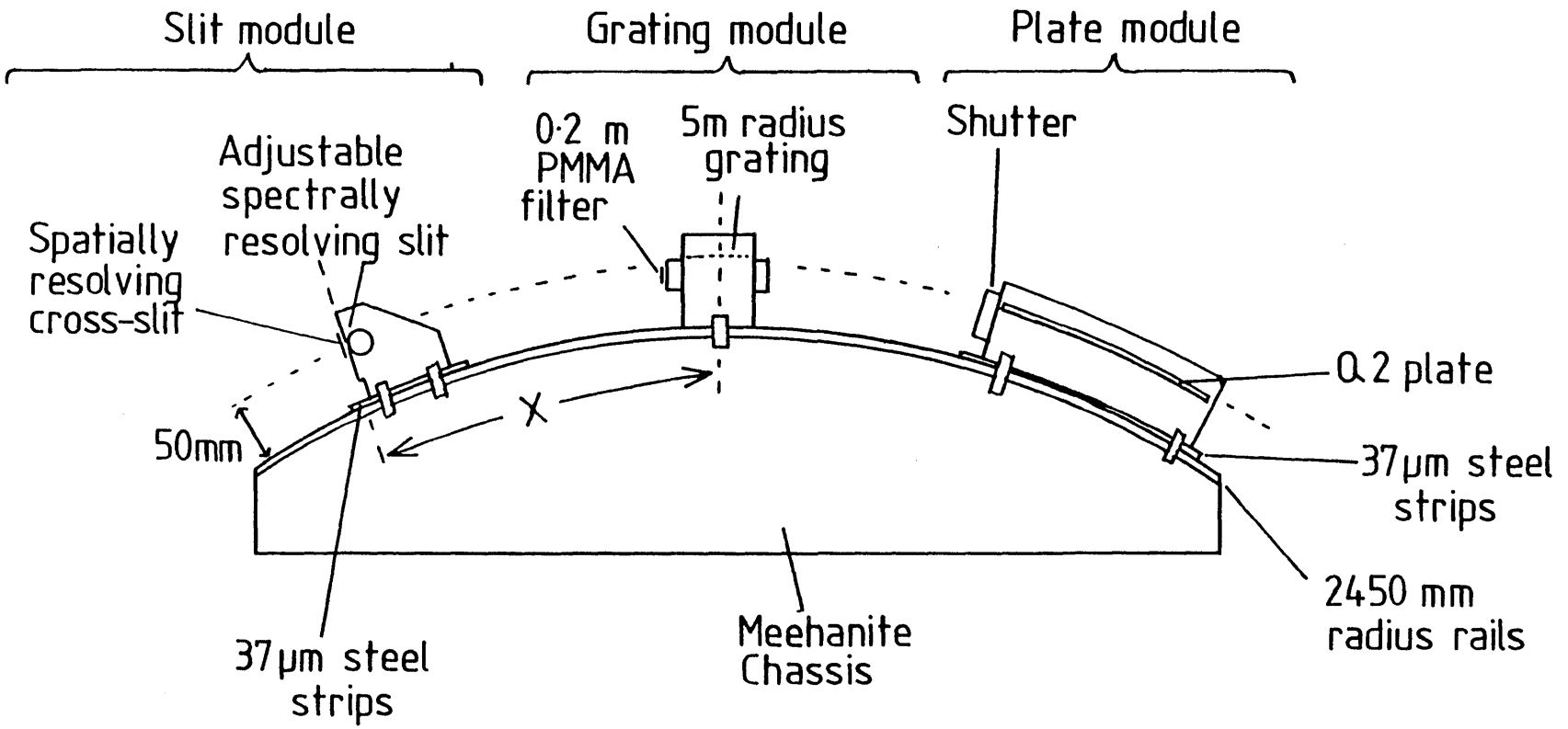


FIGURE 3.2 DIAGRAM OF THE GML5M GRAZING INCIDENCE GRATING SPECTROGRAPH

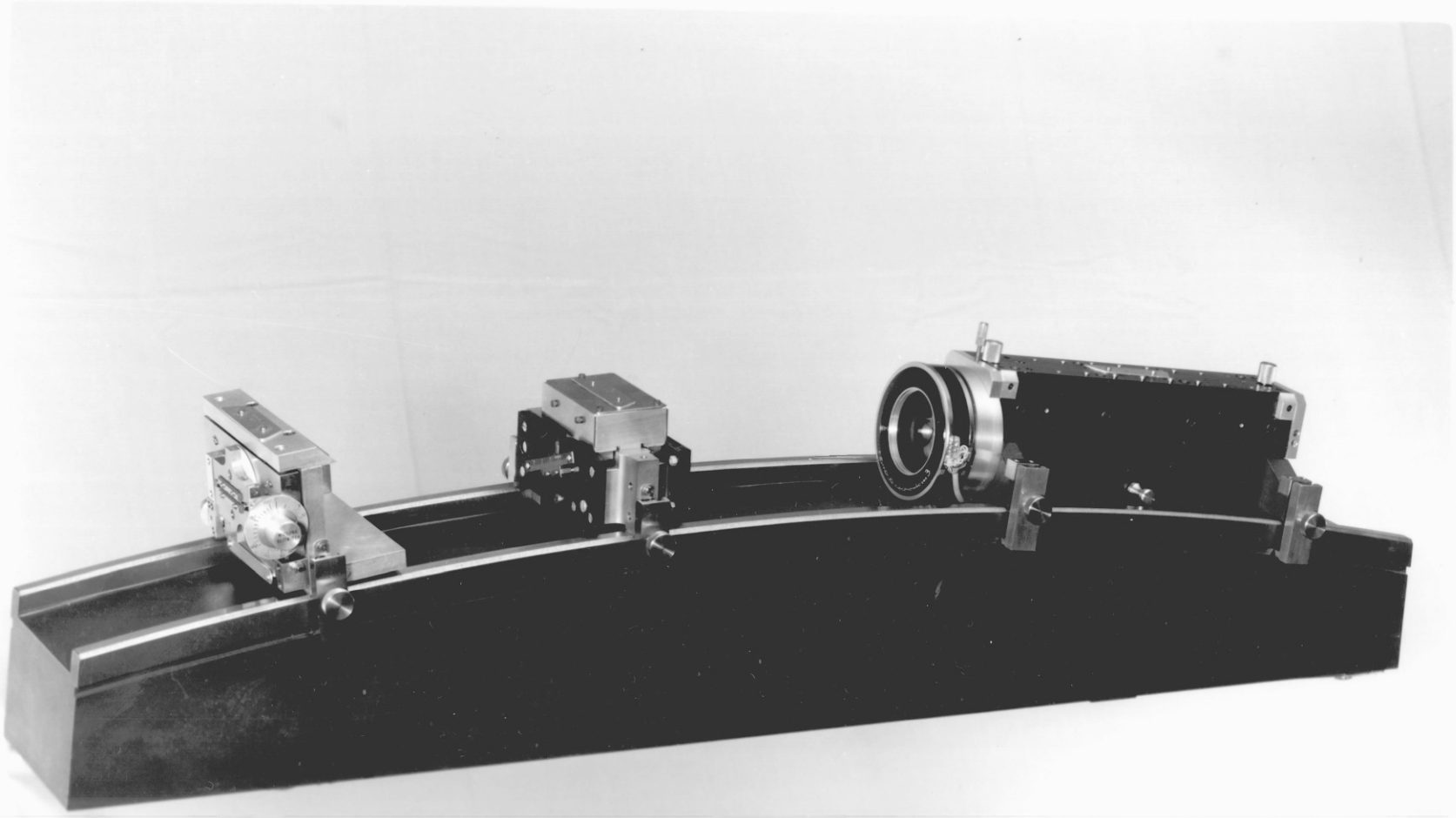


Figure 3.3 The GML5m Spectrograph

FIGURE 3.4 EFFICIENCY OF GRATING 2 AS A FUNCTION OF ANGLE

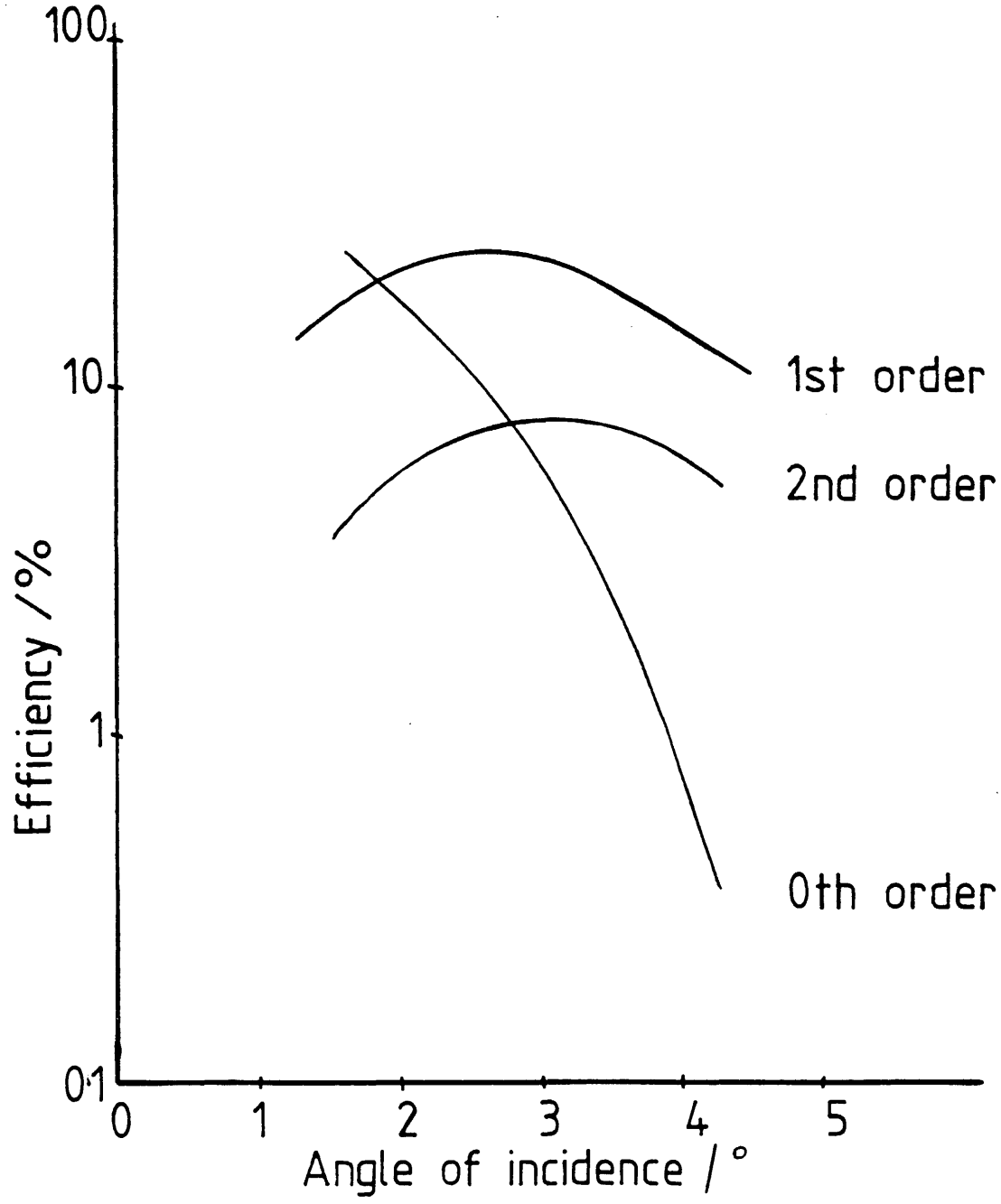


FIGURE 3.5 EFFICIENCY OF GRATING 1 AS A FUNCTION OF ANGLE in 1st order

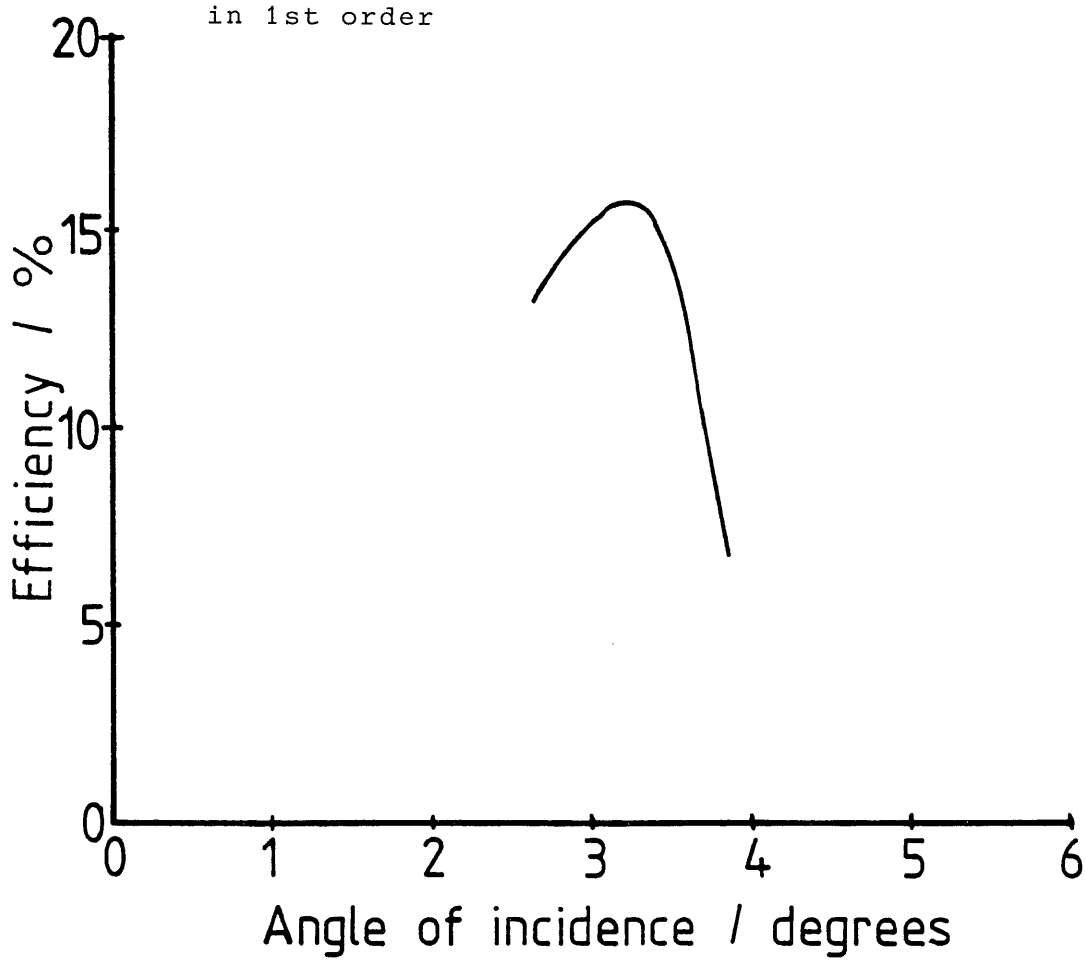
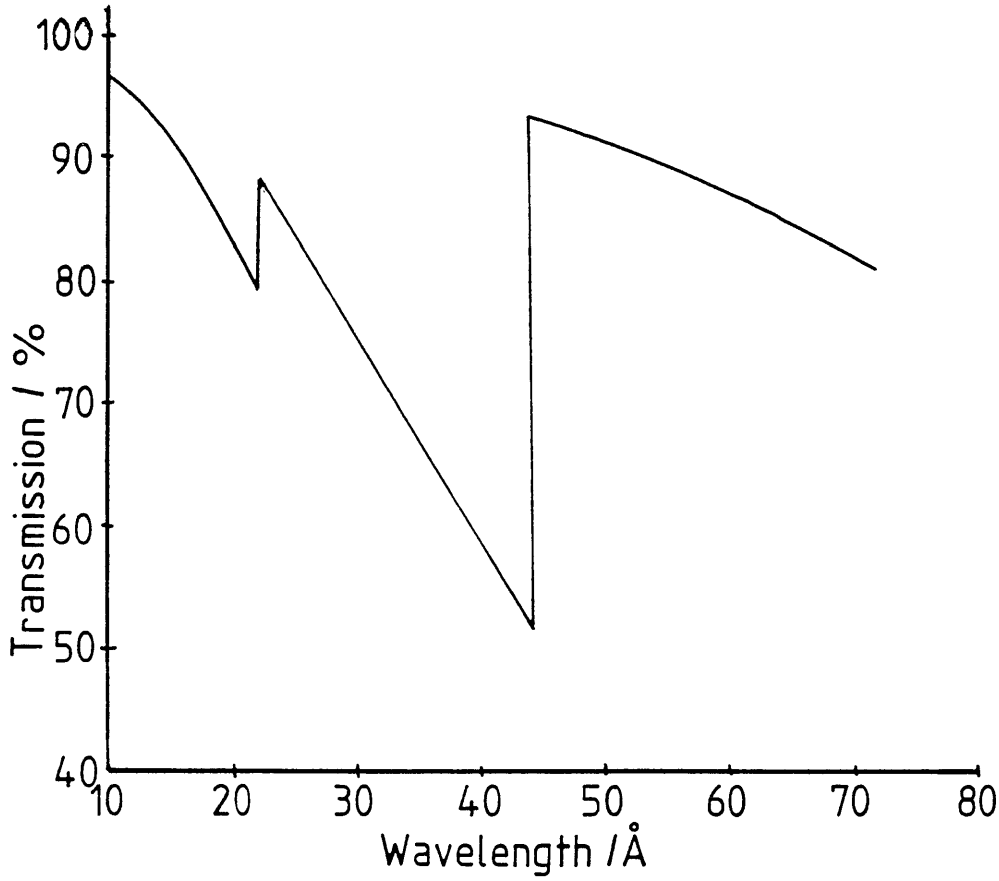


FIGURE 3.6 PERCENTAGE TRANSMISSION OF 0.2 μM PMMA FILM AS A FUNCTION OF WAVELENGTH



3.3.1 GRATINGS USED

Two gratings were used and these were 5m radius, gold plated, ruled gratings with 300l/mm. The efficiencies $G(\lambda)$ were measured at 44 A at the Imperial college grating test facility (Speer 1976), and are shown in figures 3.4 and 3.5.

The gratings were protected from debris from the source by a thin film of PMMA (polymethyl methacrylate), made by floating the polymer on water and siphoning the water away until the film came to rest on a small washer. The film was measured using an interference microscope to be 0.2 ± 0.05 μ m. The transmission curve $T(\lambda)$ for the film was calculated from the known composition of the film, and mass absorption coefficients (Henke, Shattenburg, 1975), and is given in figure 3.6.

3.3.2 PHOTOGRAPHIC PLATES

The photographic plates used were Ilford Q2 plates. These were developed in D19 developer for 4-5 minutes, and fixed in Ilford hypam for 2 minutes. The sensitivity of these plates $P(\lambda)$ has been measured by Peacock and Hobby (1973). Their results show a linear response with intensity for densities up to 0.2D, of 1.51×10^3 density J^{-1} m^2 at 10Å. Typical errors were estimated to be 10%, depending on the

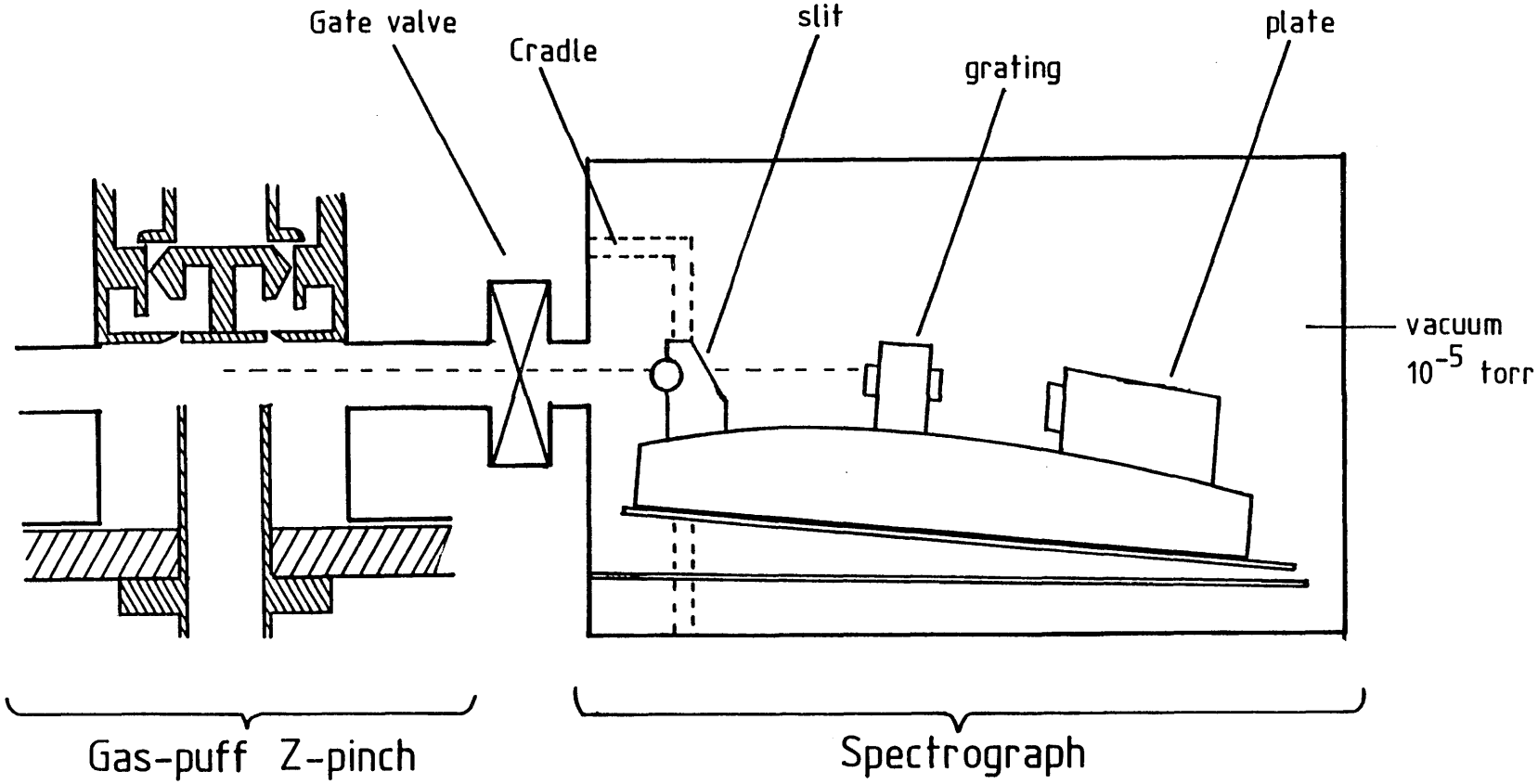


FIGURE 3.7 THE EXPERIMENTAL ARRANGEMENT

age of the film.

3.4 FOCUSING AND ADJUSTMENT OF THE SPECTROGRAPH

The experimental arrangement is shown in figure 3.7. The spectrograph was aligned to 2mm below the centre of the pinch; the rough position of the hot spots. The spectrograph slit was 60cm from the source. As the f number of the spectrograph is 125, a 5mm length of plasma was seen. Spatial resolution was achieved by placing a 120μm cross-slit, formed from two razor blades, over the main slit of the spectrograph.

As mentioned in section 3.3.1, the spectrograph was designed for perfect focus with a 5m radius grating. However grating radii can deviate from that specified by up to 30mm, so it was found that small adjustments had to be made to the focus of the instrument. This was done by raising the slit and plate modules with 37μm strips of steel until a good focus was obtained at a chosen wavelength. The results were compared to the theoretical deviation, and are shown in figure 3.8 (Mrowka 1983).

3.5 CALIBRATION OF THE SPECTROGRAPH

The spectrograph was absolutely calibrated for intensity by separately calibrating the components of it (Peacock and Hobby 1972). If the source emits $N(\lambda)$ photons be-

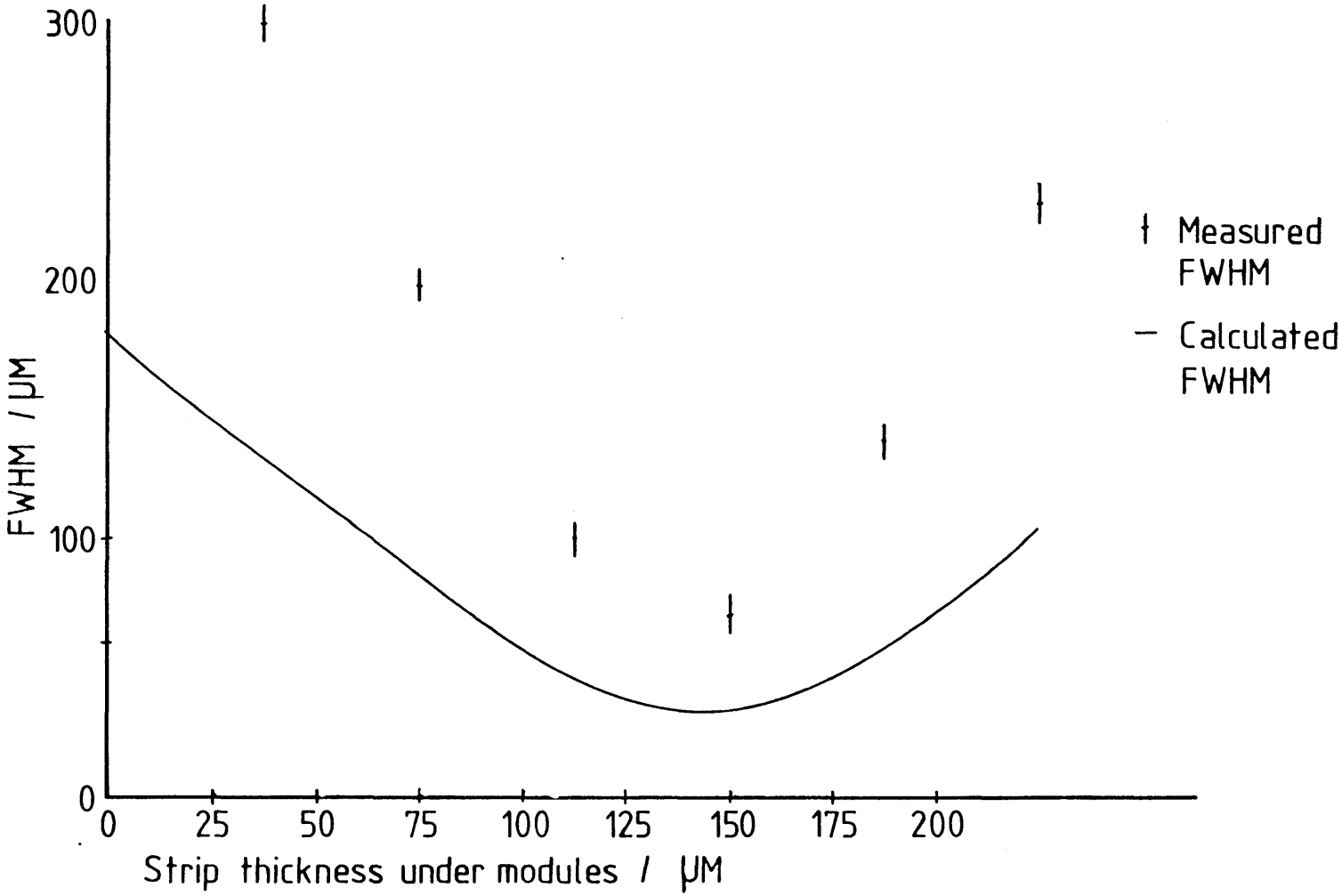


FIGURE 3.8 FWHM OF AR IX LINES AS A FUNCTION OF THE FOCUS OF THE SPECTROGRAPH

tween λ and $\lambda + \Delta\lambda$ per shot; the slit width is S and height is S´; and its distance from the source is l, then the number of photons entering the spectrograph is given by :

$$N(\lambda)\Delta\lambda \frac{S \times S'}{4\pi l^2} \qquad 3.12$$

These form an image of length :

$$\frac{S'}{l}(1 + R(\sin\alpha + \sin\beta)) \qquad 3.13$$

and width :

$$\frac{R\,\Delta\lambda}{d \sin\beta} \qquad 3.14$$

The final plate density D will then be :

$$D = \frac{N(\lambda)\, P(\lambda)\, T(\lambda)\, G(\lambda)\, S\, d \sin\beta}{4\pi l\, R(1 + R(\sin\alpha + \sin\beta))} \qquad 3.15$$

where $G(\lambda), T(\lambda), P(\lambda)$ are given in sections 3.3.1 and 3.3.2. The resulting calibration is shown in figure 3.9. Values of the parameters in equation 3.15 are given in table 3.1. Estimated errors in the calibration are due to the grating efficiency $G(\lambda)$, the plate sensitivity $P(\lambda)$, and the transmission of the film $T(\lambda)$. These total to

FIGURE 3.9 INTENSITY CALIBRATION CURVE FOR THE SPECTROGRAPH

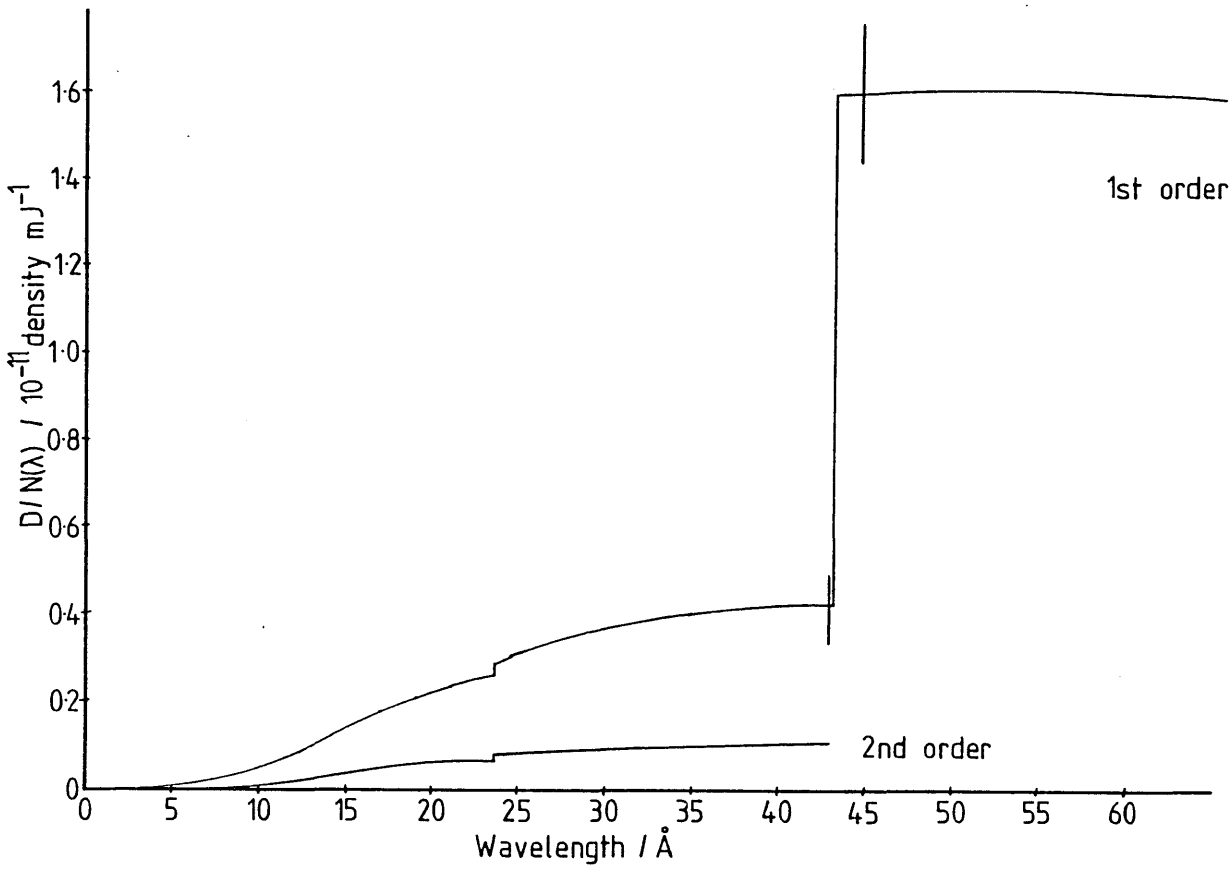


Table 3.1 Parameters for the GML5m Spectrograph

Slit Width	S = 2μm
	S´= 10 mm
Angle of incidence	$\alpha = 2^{\circ}$
Source-slit distance	l = 0.63m
Radius of grating	R = 5m
Grating spacing	d = 3.33 μm for grating 2

about 30%, and are discussed in the sections 3.3.2 and 3.3.3.

3.6 ANALYSIS OF THE SPECTRA

In order to identify lines on a plate, it was found to be easier to approximate equation 3.3 by a third order Chebyshev polynomial in x. Even ignoring errors due to aberrations in the grating, the grating equation can only be successfully used if α, d and R are well known. The most difficult of these parameters to determine is α, which is obtained using equation 3.5, by measuring the distance between the slit and the pole of the grating. This can only be practically determined to within 1%, giving an error of 0.2 Å in the wavelength. Equation 3.3 can be approximated to a third order polynomial to within 0.002%, an error of 0.4mÅ at a wavelength of 20Å.

The following procedure was adopted in order to analyse the plates :

(i) The spectra were traced with a Joyce Lobel mark 3 digital densitometer, using the shallowest wedge of range 0 - 0.497 D. The exit slit of the densitometer and the digitizing step were matched to the theoretical instrumental FWHM. This was determined using equation 3.10 to be 40μm. A suite of programs written by A. Dymoke

- Bradshaw gave the density at each point as a number between 0 and 5000 linearly related to the density, where 5000 represents a density of 1.

(ii) The data files were sent to a Cyber 855 main-frame computer for analysis.

(iii) The spectra were plotted on the screen with the aid of the 'SIMPLE' plotting library (ICCC bulletin, 1982). The wavelengths of the dominant lines in the spectrum were roughly determined using the grating equation, and these were identified using Kelly and Palumbo (1973). The positions and wavelengths of these lines were entered, and a data file produced containing the position, wavelength and intensity of the known lines.

(iv) This data file was used to calculate the coefficients of a Chebyshev polynomial of degree 3.

(v) The Chebyshev polynomial was then used to fit a wavelength scale to the spectrum, and hence obtain the wavelengths of unknown lines.

A documentation of the programs involved in steps (iii), (iv) and (v) is in the appendix.

CHAPTER 4 SPECTRA OF ARGON DISCHARGES

4.1 INTRODUCTION

This chapter presents the spectra obtained in argon plasmas, and explains how they were calibrated in terms of wavelength and intensity. A listing of the wavelengths and intensities of observed lines is presented and discussed. Spatially resolved spectra in both the radial and axial direction are presented in order to determine the region of emission of the ionization stages. A coronal model is then used in order to obtain temperatures of each of the regions of plasma. The electron density of the background plasma is obtained, and an estimate of the peak density of the core plasma given.

4.2 RESULTS

Examples of the soft x-ray spectra taken are shown in figures 4.1 to 4.3. Experimental conditions for each of the plates are given in table 4.1. The plates were densitometer traced and analysed as described in chapter 3. A trace of the plate in figure 4.1 is given in figure 4.4. A listing of the wavelengths and intensities observed on this plate is given in table 4.2. Roughly 60 standards were used to calculate the Chebyshev polynomial. The error on the wavelengths is 20 mÅ.

Table 4.1 Experimental Conditions for the spectra in chapter 4

Figure number	Plate number	α/°	S/μm	grating	number of shots	nozzle size / cm	charging voltage /kV	pressure /atmos	pre-ionization
4.1	74	2	2	2	1	5	27	8.5	Yes
4.2A	50	3.2	2	1	9	3	25	5	No
4.2B	56	3.2	2	2	2	5	26	8.5	No
4.3A	30	2	5	1	1	3	35	6	No
4.3B	65	2.7	2	2	3	5	27	8.5	Yes
4.5A	35	2	10x127	1	1	3	35	6	No
4.5B	94	2	4x400	1	5	5	27	8.5	No

Due to the complexity of the spectra, and the blending of spectral lines, accurate values for the absolute intensity were not calculated. The listed intensities were obtained by taking the peak measured density of each of the lines. The intensity was then calculated using the sensitivity of the spectrograph (equation 3.15), and assuming an instrumental FWHM of 40 mÅ. The intensities of blended lines are thus lower than is listed in the tables, and the quoted energy should be regarded as an upper maximum.

Although some of the unidentified lines observed in the spectra corresponded in wavelength to impurity lines of iron, copper and air, the much brighter transitions of impurity ions were not seen. Also, none of the questionable lines were seen in any spectra of other plasmas. Hence it is concluded that all of the lines seen in the spectra are due to argon.

A wide range of ionization stages are observed in the spectra, from Ar IX up to Ar XIII. These cannot, however exist at the same time and space in the plasma, and good values of the electron temperature can only be inferred for space and time-resolved spectra. In addition the plate in figure 4.1 shows a bright series of lines between 24Å and 28Å, which are possibly due to Ar XV.

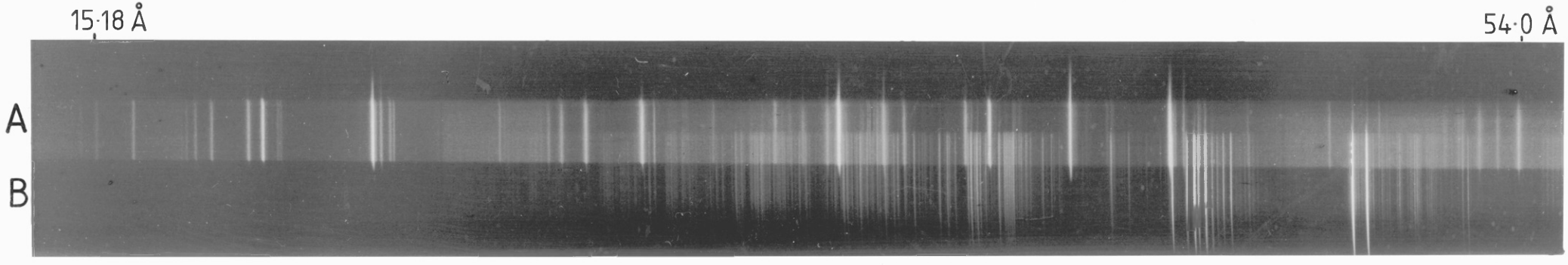
The plate in figure 4.3a shows a bright series of lines between 24Å and 28Å, which were not listed in the tables

of Kelly and Palumbo (1978). These were identified with the aid of Fawcett's (1984) theoretical predictions of the wavelengths and intensities of lines due to Ar XV, many of which have not previously been seen. The wavelengths of these lines were found using standards from the Ar IX and Ar X lines observed in the background plasma listed in table 4.2. The accuracy of the resulting wavelengths is thus 20mÅ, the same as the accuracy of the standards used. The agreement between the theoretical and experimental wavelengths is within the experimental error in all cases. A listing of the observed wavelengths and intensities is given in table 4. with the theoretical wavelengths and identifications.

The total energy of all the lines in the spectrum listed in table 4. was 28J, though as stated above, this is probably in excess of the actual radiated energy due to the blending of lines. A list of the total number of lines of each ionization stage seen together with the total energy per ionization stage is given in table 4.3. It can be seen that the dominant ionization stage in the spectra is Ar XII.

Figure 4·1 A Carbon dioxide spectrum

B Argon spectrum



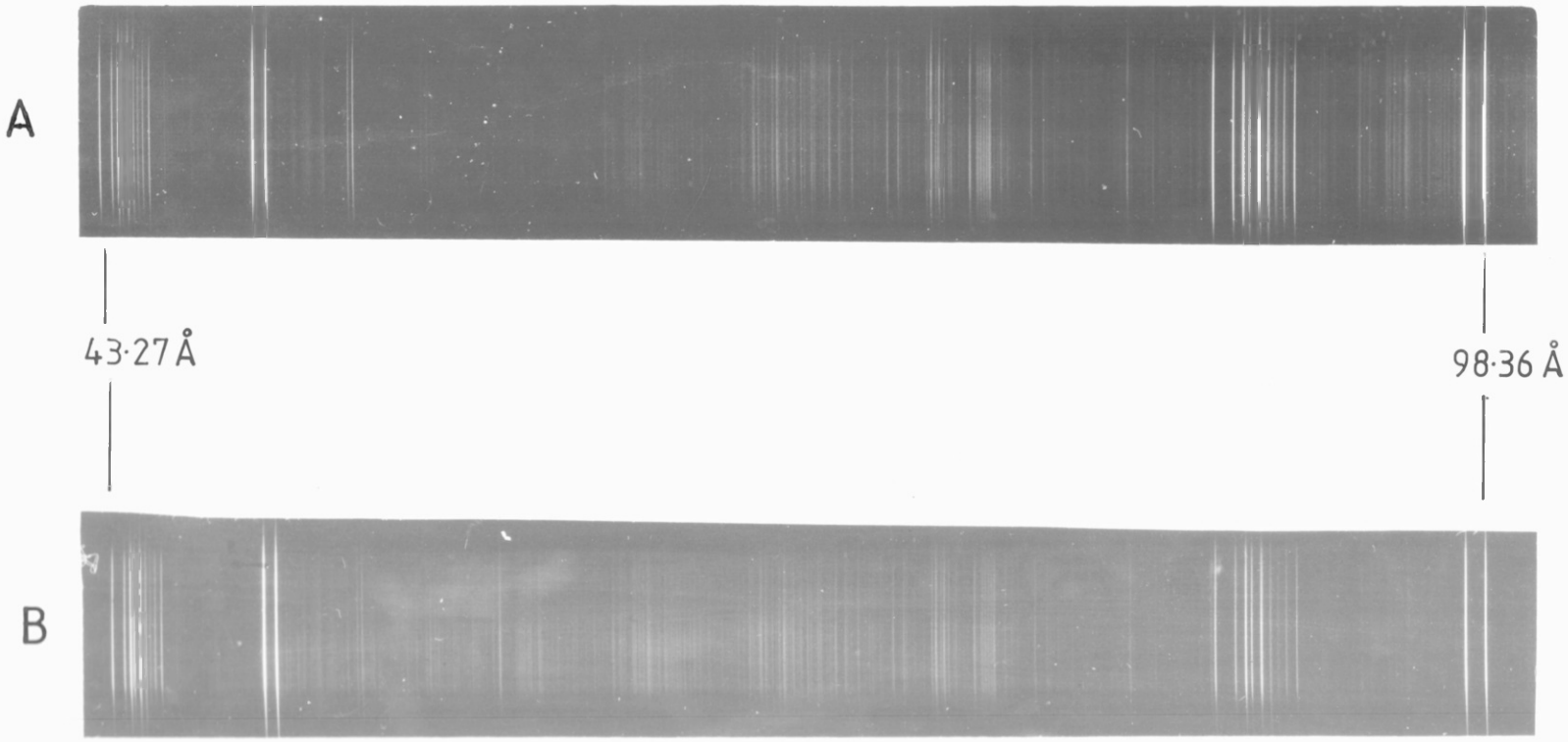


Figure 4·2 Argon spectra A 3cm nozzle

B 5cm nozzle

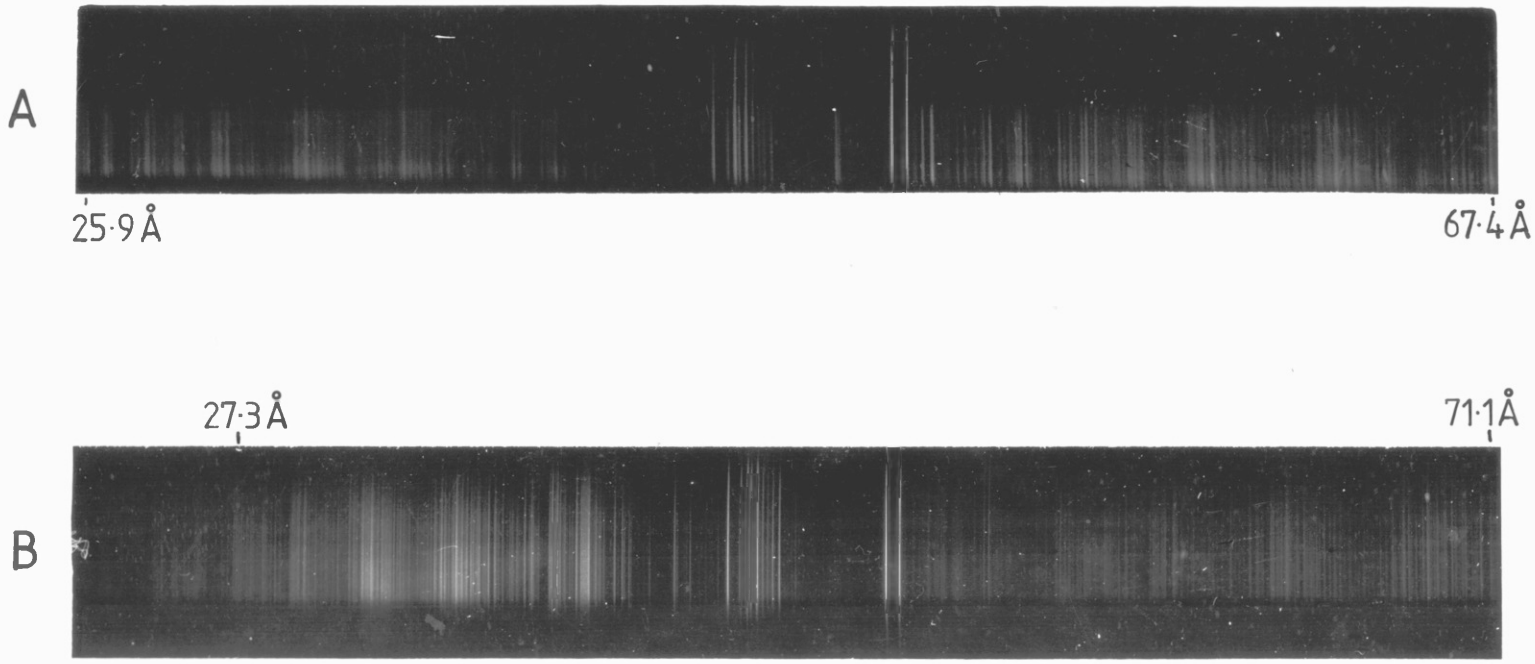


Figure 4·3 Argon spectra

A 35 kV charging voltage

B 25 kV charging voltage + pre-ionization

FIGURE 4.4 DENSITOMETER TRACE OF ARGON SPECTRUM IN FIGURE 4.1

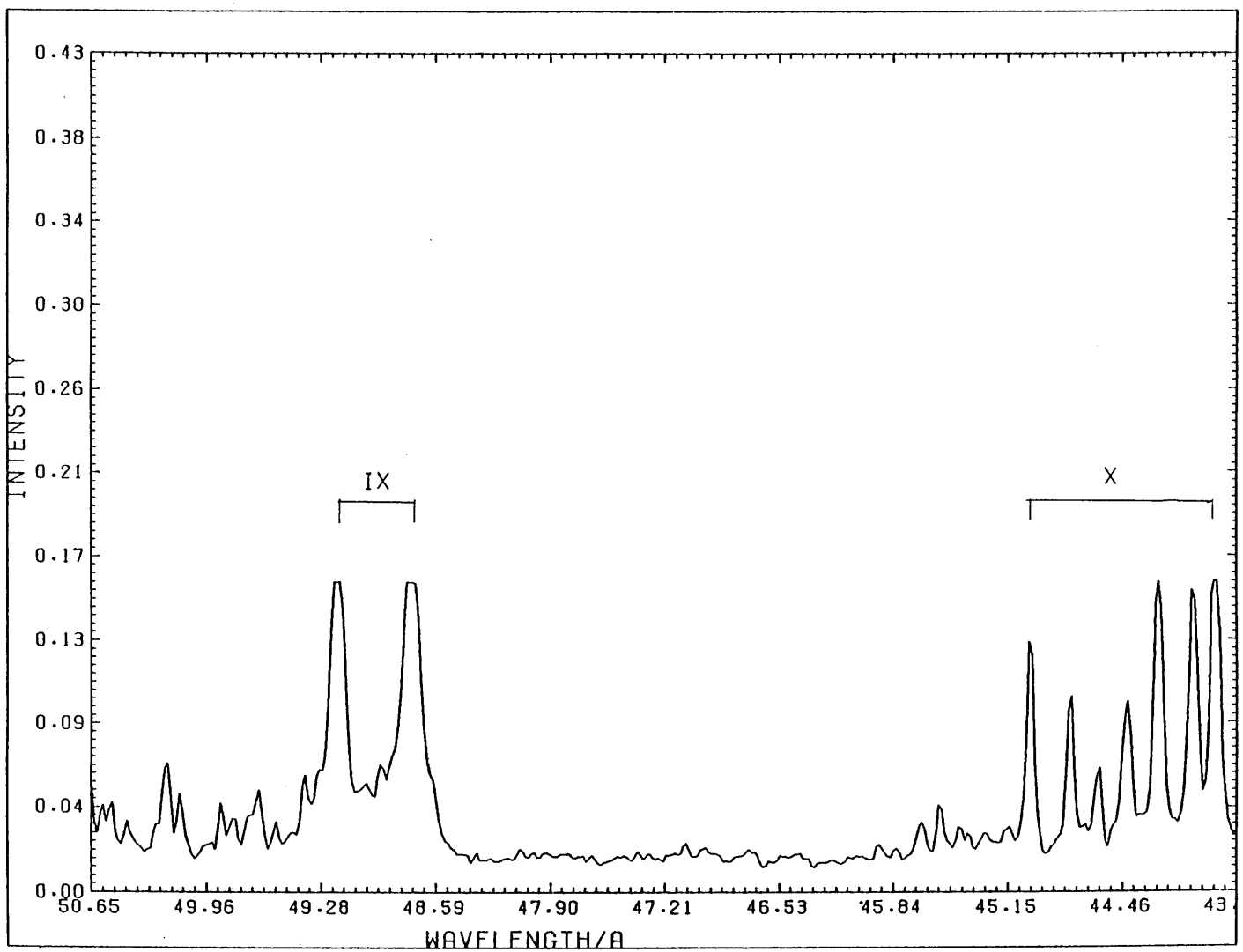


Figure 4.4 continued

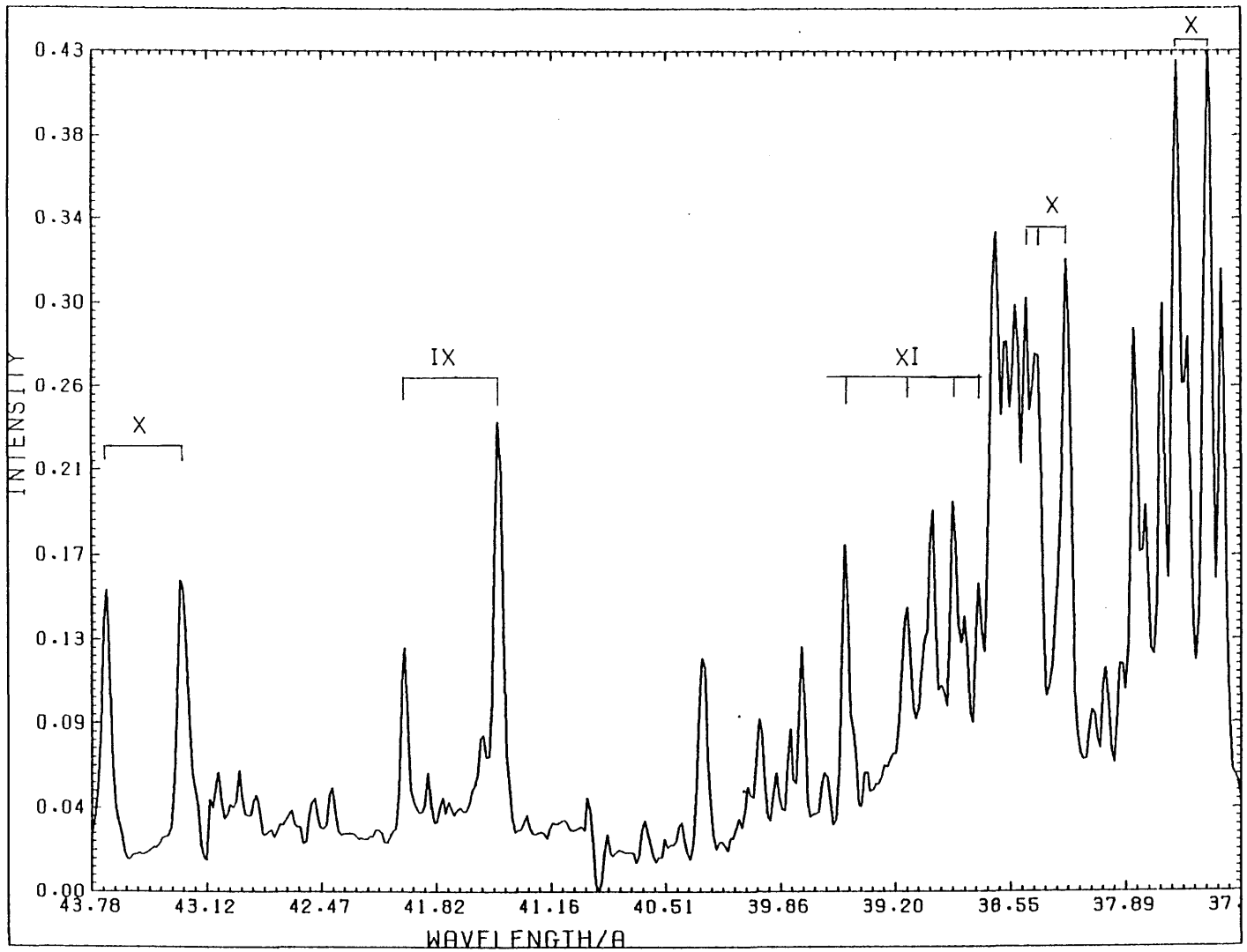


Figure 4.4 continued

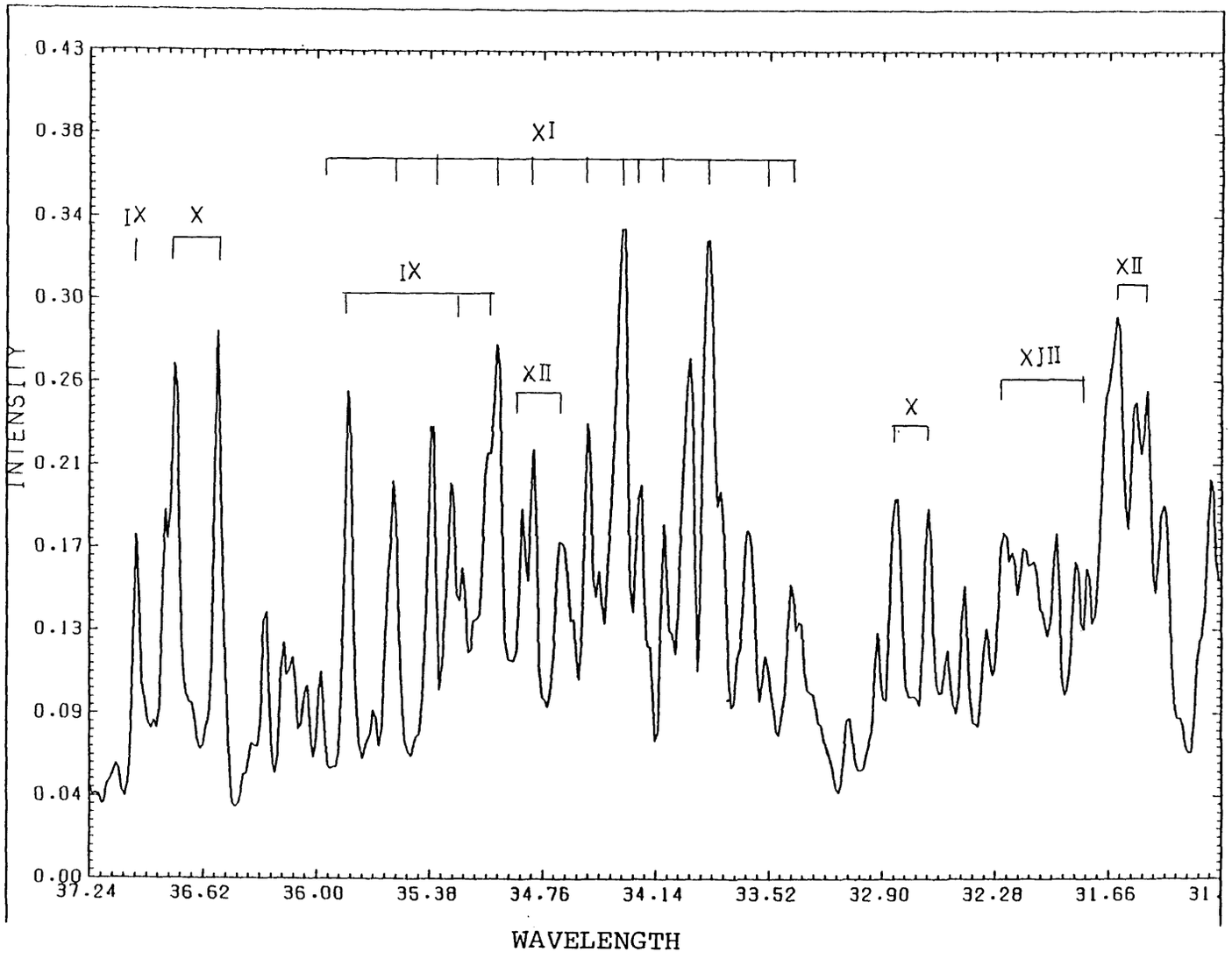


Figure 4.4 continued

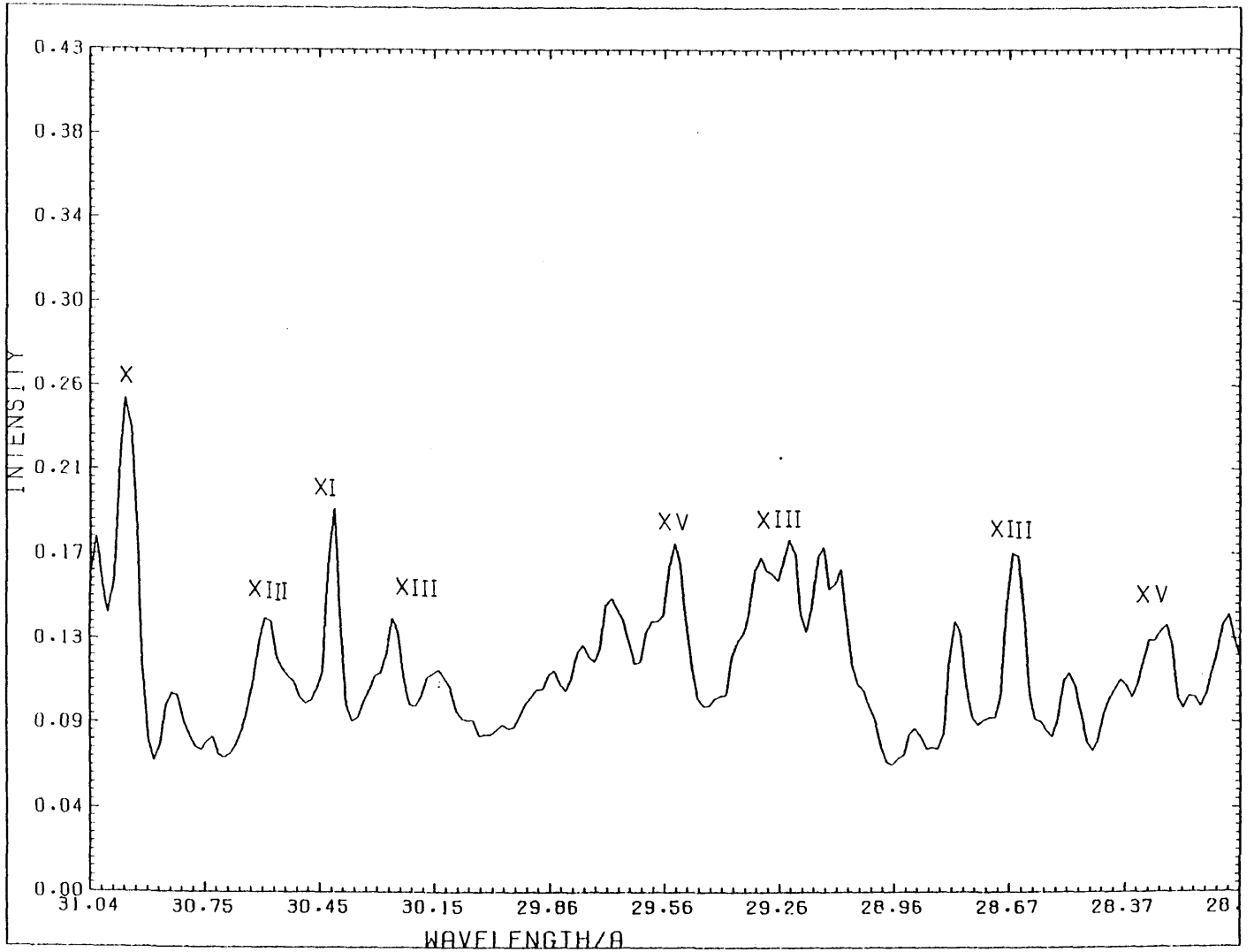


FIGURE 4,5 DENSITOMETER TRACE OF ARGON XV SPECTRUM

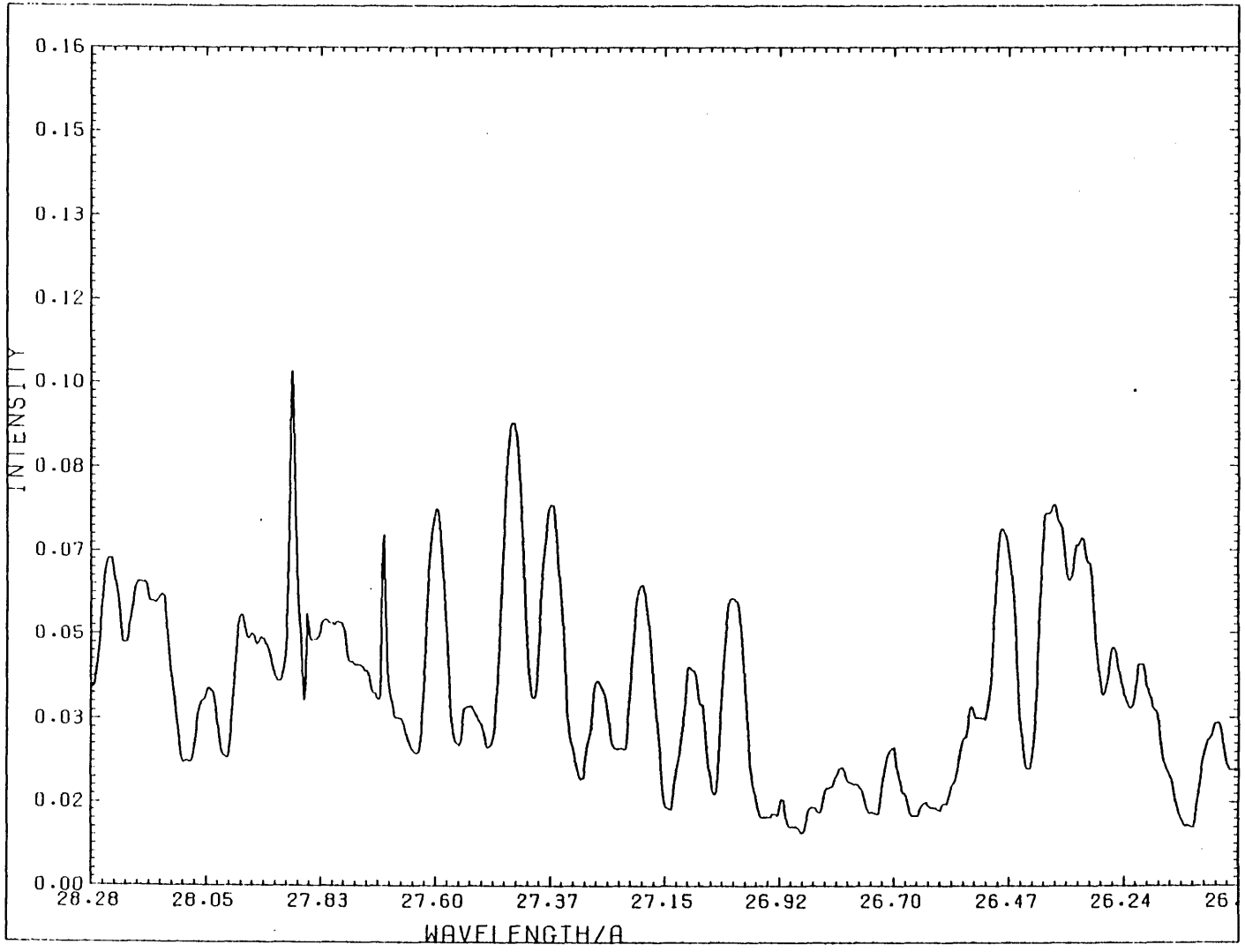


Figure 4.5 continued

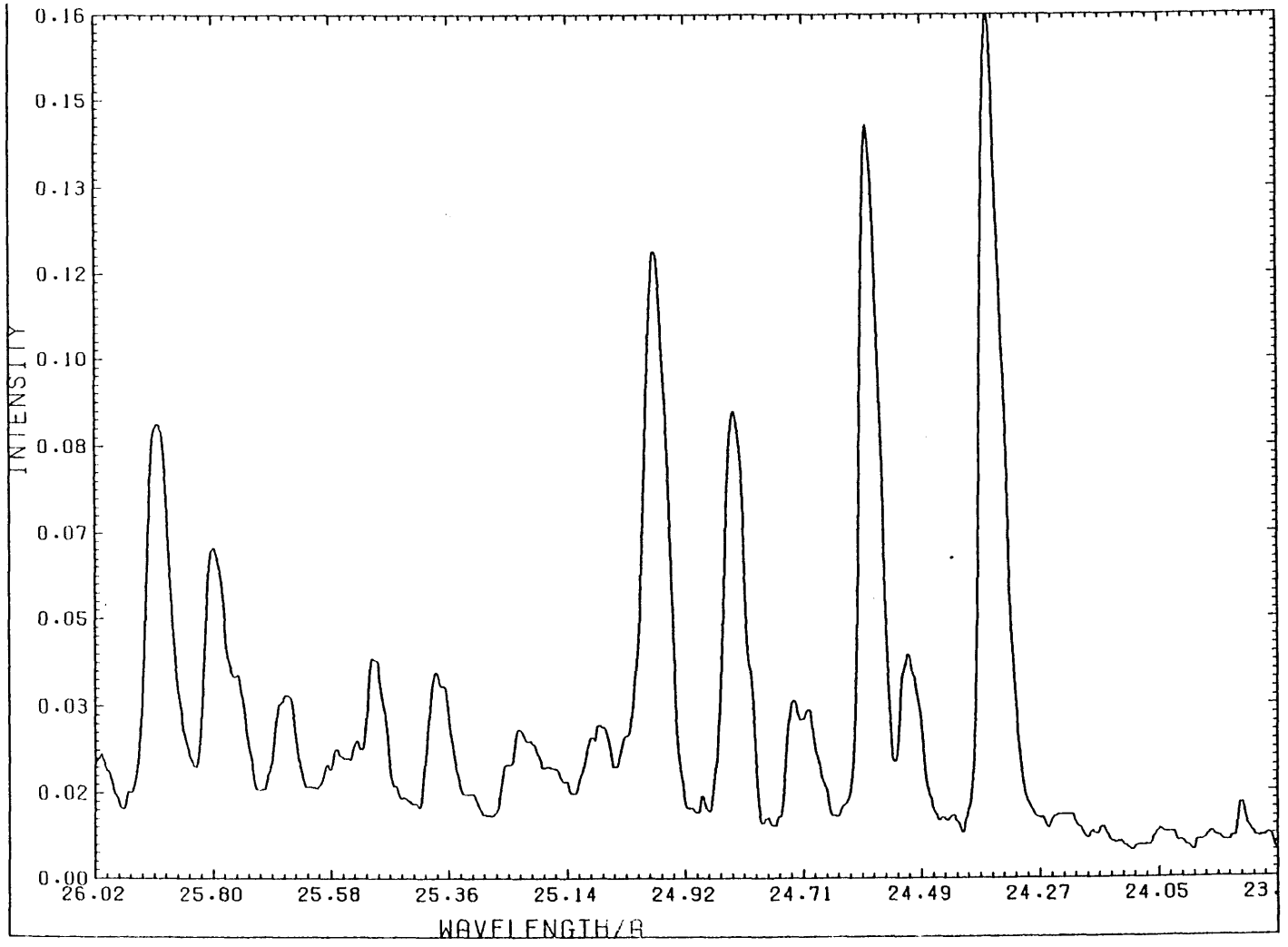


Table 4.2 Wavelengths and intensities of observed lines
Intensities measured in 1st order. 2nd order intensities agree within error

Wavelength / Å			Intensity	Ion	Configuration	Term	J-J
1st order	2nd order	theor-etical	/mJ				
	24.69	24.61	250	XIII	$2p^2$-2p4s	^1S-^2P	0-1
	24.72		130				
	24.77		150				
	24.82		220				
	24.85		160				
	24.90		150				
	24.96		190				
	24.98		100				
	25.06	25.05	200	XV	$2s^2$-2s3p	$g\,^1S$-^3P	0-1
	25.10		270				
	25.22	25.19	150	XII	$2p^3$-$2p^2$4d		
	25.26	25.24	190	XII	$2p^3$-$2p^2$4d		
	25.29		180				
	25.33		270				
	25.37		280				
	25.40	25.42	250	XIV	$2s^2$2p-2s2p3p	$g\,^2P$-^2P	$\frac{1}{2}$-$\frac{1}{2}$
	25.53		170				
	25.57	25.58	170	XIV	$2s^2$2p-2s2p3p	$g\,^2P$-^2P	$\frac{3}{2}$-$\frac{3}{2}$
	25.60	25.60	190	XV	2s2p-2s3d	^3P-^1D	2-2
	25.63		140				
	25.67		110				
	25.74	25.72	110	XV	2s2p-2s3d	^3P-^3D	0-1
	25.84	25.84	100	XV	2s2p-2s3d	^3P-^3D	1-2

Wavelength / Å			Intensity /mJ	Ion	Configuration	Term	J-J
1st order	2nd order	theor-etical					
	25.90		100				
	26.02	26.00	89	XV	2s2p-2s3d	$^3P-^3D$	2-3
	26.08		190				
	26.18		260				
	26.22		120				
	26.32	26.30	100	?			
	26.98		110				
	27.04		90				
	27.12	27.14	80	XV	2s2p-2s3s	$^3P-^3S$	2-1
	27.19	27.17	90	XIII	$2s^22p^2-2s2p^23p$	$^1D-^1D$	2-2
	27.21	27.22	90	XIV	$2s2p^2-2s2p^23d$	$^2D-^2F$	
	27.30		100				
	27.35		90				
	27.38	27.41	90	XIV	$2s2p^2-2s2p3d$	$^2D-^2D$	
27.45	27.45	27.47	170	XIV	$2s^22p-2s^23d$	g^2P-^2D	
	27.52		90				
27.55	27.55		140				
	27.60	27.60	90	XIII	$2s^22p-2s2p^23p$	g^3P-^3D	
27.63		27.63	100	XIV	$2s^22p-2s^23d$	g^2P-^2D	
27.69	27.68		100				
27.78	27.77	27.79	90	?			
	27.81		140				
	27.87		100				

Wavelength / Å			Intensity	Ion	Configuration	Term	J-J
1st order	2nd order	theor-etical	/mJ				
27.91	27.92	27.90	100	?			
	27.97		100				
27.99	27.99		120				
28.11	28.09		100				
28.27	27.26	28.26	100	XV	$2s2p-2s3s$	$^1P-^1S$	1-0
28.32	28.30	28.32	100	XV	$2s2p-2s3s$	$^1P-^1S$	1-0
28.39	28.36		100				
	28.46		120				
28.52	28.51		100				
28.66	28.65	28.68	130	XIII	$2s^22p^2-2s2p^23p$	$^1S-^1P$	0-1
28.81	28.78		110				
28.92			60				
29.11	29.10	29.1	130	X	$2p^5-2p^45d$	$g\,^2P-^2D$	
29.16	29.15		130				
29.24	29.24	29.2	140	XIII	$2p^2-2p3d$	$g\,^3P-^3P$	1-0
29.31	29.33	29.32	120	XIII	$2p^2-2p3d$	$g\,^3P-^3P$	2-1
	29.37	29.37	130	XIII	$2p^2-2p3d$	$^3P-^3P$	2-2
29.54	29.52		140				
29.60	29.58	29.57	110	XV	$2p^2-2s3p$	$^1D-^1P$	2-1
29.70	29.71		110				
29.77	29.79		100				
29.85		29.85	80	XIII	$2p^2-2p3d$	$^1D-^1P$	2-1
	29.90	29.90	100	XIV	$2s2p^2-2s2p3d$	$^2P-^2D$	
	30.06		100				

Wavelength / Å			Intensity	Ion	Configuration	Term	J-J
1st order	2nd order	theor-etical	/mJ				
30.15	30.11		90				
	30.17	30.21	110	XIII			
30.26	30.26	30.24	110	XIII			
	30.33	30.34	120	XIII	$2p^2$-2p3d	^1D-^1D	2-2
30.42	30.42	30.40	120	XI	$2s^22p^4$-$2s2p^43p$	$g\,^3P$-^3P	2-2
	30.49		120				
30.59	30.59	30.58	110	XIII			
	30.68	30.68	110	XIII	$2p^2$-2p3d	^1S-^3P	0-1
30.73	30.76	30.77	75	XIII			
30.83	30.81	30.84	87	XIII			
	30.85		100				
30.95	30.96	30.96	180	X	$2p^5$-$2p^44d$	$g\,^2P$-^2D	
31.03	31.02	31.08	120	X	$2p^5$-$2p^44d$	$g\,^2P$-^2D	
31.11	31.10	31.10	140	XI	$2s^22p^4$-$2s2p^43p$	^1S-^1P	0-1
31.17	31.17	31.18	100	XII			
	31.20		110				
31.27			61				
31.37	31.35	31.35	140	XII	$2p^3$-$2p^23d$	$g\,^4S$-^4P	
	31.38	31.39	160	XII			
31.46	31.46	31.47	180	XII			
31.52	31.53	31.55	170	XII	$2p^3$-$2p^23d$	$g\,^4S$-^4P	
31.63	31.63	31.65	210	XII	$2p^3$-$2p^23d$	^2D-^2F	
31.68	31.68	31.70	170	XIII	$2p^2$-2p3s	$g\,^3P$-^3P	2-1
	31.74		130				

Wavelength / Å			Intensity	Ion	Configuration	Term	J-J
1st order	2nd order	theor-etical	/ mJ				
31.78	31.78	31.78	130	XIII	$2p^2$-2p3s	$g\,^3P$-^3P	2-2
31.85	31.84	31.86	130	XIII	$2p^2$-2p3s	$g\,^3P$-^3P	1-0
31.96	31.97	31.99	130	XII	$2p^3$-$2p^2$3d	^2D-^2D	
32.08	32.08		130				
32.13	32.11		130				
	32.16	32.16	130	XII	$2p^3$-$2p^2$3d	^2D-^2D	
32.20	32.20	32.20	130	XII	$2p^3$-$2p^2$3d	^2D-^2D	
32.24	32.27	32.25	140	XIII	$2p^2$-2p3s	^1D-^1P	2-1
32.34	32.36	32.35	110	XII	$2p^3$-$2p^2$3d	^2D-^2F	
32.46	32.42	32.45	140	X	$2s^22p^5$-$2s2p^5$3p	$g\,^2P$-^2P	
	32.46		140				
32.55		32.55	90	X	$2s^22p^5$-$2s2p^5$3p	$g\,^2P$-^2D	
	32.63	32.61	110	X	$2s^22p^5$-$2s2p^5$3p	$g\,^2P$-^2D	
32.65	32.66	32.64	140	IX	$2p^6$-$2p^5$5d	$g\,^1S$-	
	32.76	32.74	90	X	$2s^22p^5$-$2s2p^5$3p	$g\,^2P$-^2D	
32.83	32.85		140				
32.93	32.94		100				
33.09	33.01	33.03	70	XI?			
	33.14		90				
33.28	33.30		90				
33.35	33.37		100				
33.41	33.43		120				
33.55	33.53	33.53	100	XI	$2p^4$-$2p^3$3d	$g\,^3P$-^3D	1-1
33.64	33.63	33.65	130	XI	$2p^4$-$2p^3$3d	$g\,^3P$-^3D	2-3

Wavelength / Å			Intensity	Ion	Configuration	Term	J-J
1st order	2nd order	theor-etical	/ mJ				
	33.66		150				
33.69	33.71		103				
33.79	33.76		160				
33.86	33.87	33.84	210	XI	$2p^4-2p^3 3d$	$g\,^3P-^3D$	1-2
	33.89		160				
33.96	33.97	33.95	190	XIII	$2p^2-2p3s$	$^1S-^1P$	2-1
	34.01		140				
	34.06		100				
34.09	34.12	34.10	140	XI	$2p^4-2p^3 3d$	$g\,^3P-^3S$	2-1
34.18	34.18		100				
34.23	34.25	34.24	150	XI	$2p^4-2p^3 3d$	$g\,^3P-^3P$	2-2
34.33	34.34	34.33	230	XI	$2p^4-2p^2 3d$	$g\,^3P-^3D$	1-2
	34.43		120				
34.47	34.46		120				
34.52	34.53	34.52	180	XI	$2p^4-2p^2 3d$	$g\,^3P-^3D$	2-1
34.61	34.61		100				
	34.65		100				
34.67	34.68	34.67	130	XII	$2p^3-2p^2 3s$	$g\,^4S-^4P$	
34.82	34.82	34.80	160	XI	$2p^4-2p^3 3d$	$^1D-^1F$	2-3
34.88	34.89	34.88	140	XII	$2p^3-2p^2 3s$	$g\,^4S-^4P$	
35.01	35.03	35.02	190	IX	$2p^6-2p^5 4d$	$g\,^1S-{}^{1(3)}_{2(2)}$	
35.07	35.10	35.07	150	XI	$2p^4-2p^3 3d$	$^1D-^1D$	2-2
35.14			100				
35.21	35.20		120				

Wavelength / Å			Intensity	Ion	Configuration	Term	J-J
1st order	2nd order	theoretical	/ mJ				
35.27	35.27	35.28	170	IX	$2p^6-2p^5 4d$	$g\,^1S-\frac{3}{2}(\frac{3}{2})$	
35.37	35.38	35.37	170	XI	$2p^4-2p^3 3d$	$g\,^3P-^3D$	2-3
35.59	35.58	35.58	150	XI	$2p^4-2p^3 3d$	$g\,^3P-^3D$	2-3
	35.62		100				
35.69	35.69	35.70	80	XI	$2p^4-2p^3 3d$	$^1S-^1P$	0-1
35.72	35.76		70				
35.83	35.84	35.82	170	IX	$2s^2 2p^6-2s 2p^6 3p$	$g\,^1S-^1P$	0-1
35.98	35.97	35.96	90	XI	$2p^4-2p^3 3d$	$^1S-^1P$	0-1
	36.03		90				
36.06	36.07		100				
36.13	36.14		100				
36.18	36.18	36.16	90	XI			
36.28	36.29		110				
36.35	36.34	36.31	80	XI			
36.39		36.39	40	X?			
	36.44		80				
36.54	36.55	36.56	200	X?			
36.68	36.70	36.69	80	X	$2p^5-2p^4 3d$	$g\,^2P-^2D$	
36.78	36.76	35.78	190	X	$2p^5-2p^4 3d$	$g\,^2P-^2D$	
36.82	36.82		140				
36.89	36.89		80				
	35.94		100				
36.99	36.98	36.96	120	IX	$2p^6-2p^5 4s$	$g\,^1S-\frac{3}{2}(\frac{3}{2})$	
	37.02		80				

Wavelength / Å			Intensity	Ion	Configuration	Term	J-J
1st order	2nd order	theor-etical	/mJ				
37.10	37.12	37.10	60	X?			
37.20	37.18		50				
	37.27		70				
37.35	37.34		210				
37.44	37.42	37.43	283	X	$2p^5-2p^4 3d$	$g\,^2P-^2D$	
	37.52		160				
37.55	37.59		210				
37.62		37.60	340	X	$2p^5-2p^4 3d$	$g\,^2P-^2D$	
37.69	37.68		208				
37.79	37.78	37.79	130	XI	$2p^4-2p^3 3d$	$^1D-^1F$	2-3
37.85	37.83		180				
	37.90		90				
37.92	37.97		90				
38.01	38.05	38.00	90	XI	$2p^4-2p^3 3s$	$g\,^3P-^3P$	
38.09	38.09		80				
38.24	38.22	38.23	230	X	$2p^5-2p^4 3d$	$g\,^2P-^2D$	
	38.36	38.33	150	XI	$2p^4-2p^3 3s$	$^1D-^1P$	2-1
38.40	38.38	38.40	190	X	$2p^5-2p^4 3d$	$g\,^2P-^2P$	
38.46	38.44		210				
	38.49		185				
38.52	38.51	38.51	190	X	$2p^5-2p^4 3d$	$g\,^2P-^2D$	
38.58	38.55		190				
38.64	38.62	38.62	220	XI	$2p^4-2p^3 3s$	$g\,^3P-^3D$	2-3
38.73			130				

Wavelength / Å			Intensity	Ion	Configuration	Term	J-J
1st order	2nd order	theor-etical	/mJ				
38.81		38.79	120	XI	$2p^4-2p^3 3s$	$g\,^3P-^3D$	2-3
38.87		38.87	160	XI	$2p^5-2p^4 3d$	$g\,^2P-^4D$	
38.94			90				
39.04			100				
39.13			120				
39.37			60				
39.43			60				
39.48		39.49	150	XI	$2p^4-2p^3 3s$	$^1D-^1D$	
39.59		39.64	50	XI	$2p^4-2p^3 3s$	$^1D-^3D$	2-2
39.73		39.75	100	XI	$2p^4-2p^3 3s$	$g\,^3P-^3S$	2-1
39.80		39.79	70	XI?			
39.90			50				
39.97		39.98	70	XI	$2p^4-2p^3 3s$	$^1D-^1P$	1-1
40.04		40.04	45	XI	$2p^4-2p^3 s$	$^1S-^1P$	0-1
40.30			100				
40.42			30				
40.63			30				
40.85			20				
40.95			40				
41.30			40				
41.47		41.48	207	IX	$2p^6-2p^5 3d$	$g\,^1S-\frac{1}{2}(\frac{3}{2})$	
41.56		41.57	70	X	$2p^5-2p^4 3s$	$g\,^2P-^2S$	
41.78			40				
41.86		41.89	50	X	$2p^5-2p^4 3s$	$g\,^2P-^2S$	

Wavelength / Å			Intensity	Ion	Configuration	Term	J-J
1st order	2nd order	theor-etical	/mJ				
42.00		42.02	100	IX	$2p^6-2p^5 3d$	$g\,^1S-\frac{3(3)}{2(2)}$	0-1
43.26		43.27	130	X	$2p^5-2p^4 3s$	$g\,^2P-^2D$	
43.69		43.69	130	X	$2p^5-2p^4 3s$	$g\,^2-^2P$	
43.90		43.92	130	X	$2p^5-2p^4 3s$	$g\,^2P-^2P$	
44.04		44.05	130	X	$2p^5-2p^4 3s$	$g\,^2P-^2P$	
44.25		44.27	130	X	$2p^5-2p^4 3s$	$g\,^2P-^2P$	
44.44		44.45	80	X	$2p^5-2p^4 3s$	$g\,^2P-^4P$	
44.61		44.63	50	X	$2p^5-2p^4 3s$	$g\,^2P-^4P$	
44.78		44.79	80	?			
45.02		45.03	100	X	$2s2p^6-2s2p^5 3s$	$^2S-^2P$	
45.16			30				
45.29			20				
45.39		45.38	20	XII			
45.44		45.49	30	XII	$2p^3-2p^2 3s$	$^2D-^2D$	
45.56			40				
45.66			30				
45.81			20				
45.91			20				
48.73		48.73	130	IX	$2p^6-2p^5 3s$	$g\,^1S-$	0-1
48.92			60				
49.00			50				
49.17		49.18	130	IX	$2p^6-2p^5 3s$	$g\,^1S-$	0-1

Table 4.3 Summary of table 4.2

Ionization stage	No. of lines	Total Energy /J
Ar IX	9	1.22
Ar X	29	3.88
Ar XI	30	3.86
Ar XII	16	2.28
Ar XIII	24	2.95
Ar XIV	7	1.10
Ar XV	10	1.11
Other	108	12.1
Total	233	28.5

Table 4.4 Wavelengths and Intensities of observed Ar XV lines

Wavelength /Å	Int-ensity /mJ	Theoretical Wavelength /Å	Ion	Configur-ation	Term	J-J
23.49	56					
23.53	35					
24.51	32	24.534	XV	2s2p-2p3p	^3P-^3P	2-3
24.70	22	24.697	XV	$2s^2$-2s3p	^1S-^1P	0-1
24.73	23	24.734	XV	$2s^2$2-2s3p	^1S-^3P	0-1
24.84	77					
24.99	105					
25.09	15	25.086	XV	2s2p-2p3p	^1P-^1S	1-0
25.11	10					
25.19	9					
25.22	12					
25.25	17					
25.37	24					
25.39	24	25.42	XV	2s2p-2p3p	^1P-^1D	1-2
25.51	27					
25.67	18					
25.77	23	25.78	XV	2s2p-2s3d	^3P-^3D	0-1
25.80	45	25.822	XV	2s2p-2s3d	^3P-^3D	1-2
25.90	70	25.921	XV	2s2p-2s3d	^3P-^3D	2-3
26.01	10	26.034	XV	2s2p-2p3p	^1P-^1P	1-1
26.07	19					
26.21	32	26.234	XV	$2p^2$-2p3d	^3P-^3P	1-1

Wavelength /A	Intensity /mJ	Theoretical Wavelength /A	Ion	Configuration	Term	J-J
26.27	32					
26.33	58	26.343	XV	$2p^2$-2p3d	^3P-^3P	2-2
26.39	64	26.412	XV	$2p^2$-2p3d	^3P-^3D	2-3
26.49	54	26.501	XV	$2p^2$-2p3d	^1D-^1F	2-3
26.55	19					
26.70	13	26.671	XV	$2p^2$-2p3d	^3P-^3F	2-3
26.80	10					
27.02	45	27.045	XV	2s2p-2s3d	^1P-^1D	1-2
27.10	28	27.087	XV	$2p^2$-2p3d	^1D-^1D	2-2
27.21	45	27.206	XV	$2p^2$-2p3d	^1D-^3F	2-2
27.28	31					
27.38	54					
27.46	70					
27.54	9	27.559	XV	$2p^2$-2p3s	^3P-^3P	0-1
27.61	46	27.591	XV	$2p^2$-2p3d	^1S-^1P	0-1
27.71	18	27.733	XV	$2p^2$-2p3s	^3P-^3P	2-1
27.79	27	27.797	XV	$2p^2$-2p3s	^1D-^1P	2-1
27.95	22					
27.96	23					
27.99	27					
28.04	14					

4.3 SPATIALLY RESOLVED SPECTRA

Examples of the radially and axially resolved spectra are shown in figure 4.6. These were taken with a 100 μm cross-slit placed on the spectrally resolving slit of the spectrograph. The conditions for these spectra are listed in table 4.1.

The radially resolved spectrum shows that most of the lines were emitted from a small central region. with a diameter of 0.4 ± 0.2 mm. This corresponds roughly to the region of emission of the harder x-rays, shown in figure 1.3, using pinhole photography. The spectrum also shows however, that two groups of Ar IX and Ar X lines come from a much wider region of the plasma, corresponding to a more diffuse background plasma, of 11.0 ± 0.1 mm in diameter (figure 4.6). Hence these two groups of lines will be analysed separately from the rest in order to obtain a temperature for the background plasma.

The axially resolved spectrum again shows that the two groups of Ar IX and Ar X lines come from a broader region of plasma, of length 8±1 mm. The rest of the radiation comes from three regions of length <100μm, limited by the spatial resolution of the spectrograph, which are assumed to correspond to the hot spots. The spectral resolution of this spectrum is poor, and hence it is difficult to observe the ionization stages present.

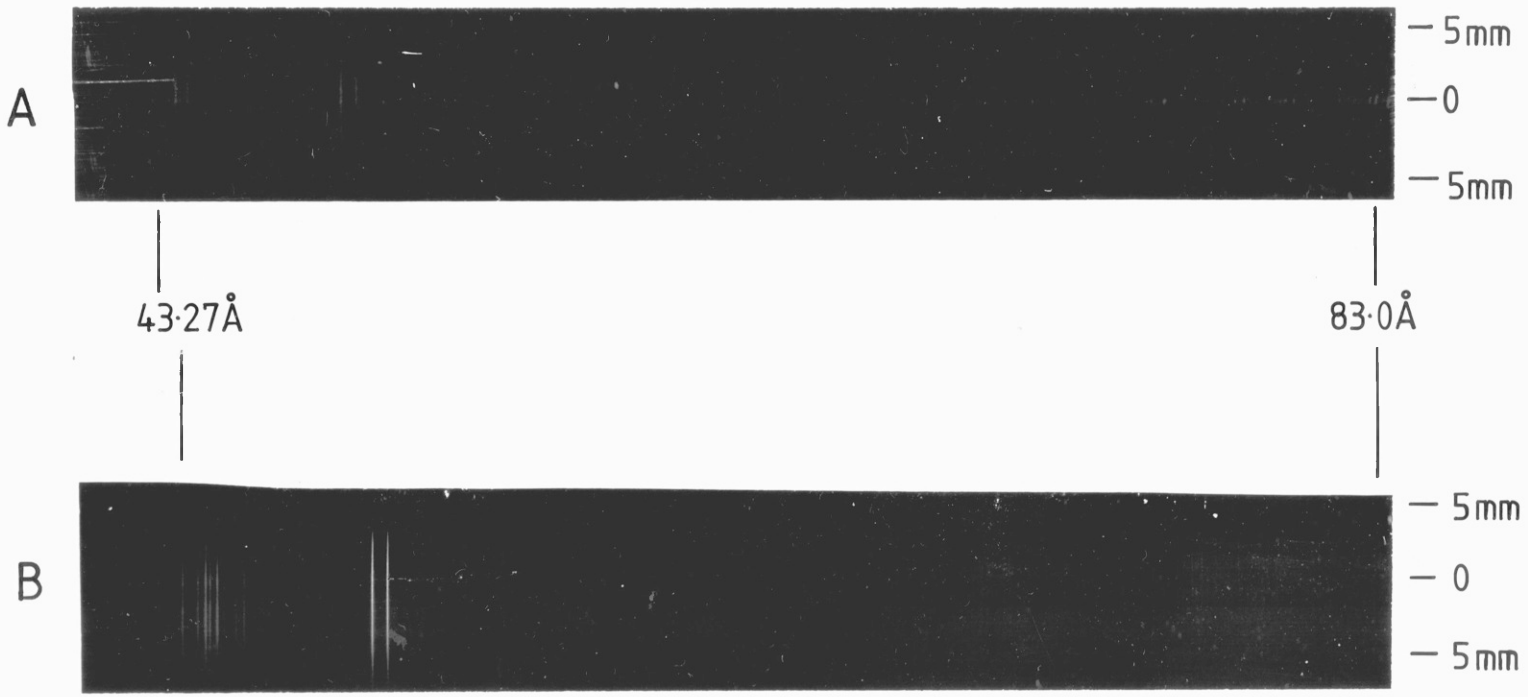


Figure 4·6 Argon spectra A Radially resolved

B Axially resolved

4.4 ANALYSIS OF THE SPECTRA

Only a limited amount of analysis of these spectra can be done, partly due to their complexity, but also due to the lack of atomic data for the observed transitions. The theoretical ionization of the plasma at a given temperature can be found by assuming a coronal model, and can be compared to the observed distribution of species. Electron densities by can be found assuming a coronal model for the ionization stages for which atomic data exists (Ar IX and Ar XV). This atomic data is given in table 4.5.

Table 4.5 Wavelengths and Oscillator strengths for argon lines

Ion	Configuration	Wavelength /Å	f-value	Energy /eV
IX	$2p^6-2p^5 3s$	48.73	0.14	254.4
IX	$2p^6-2p^5 3s$	49.18	0.052	252.1
XV	2s2p-2s3d	25.921	0.43	478
XV	2s2p-2s3d	27.045	0.36	458
XV	$2p^2-2p3d$	27.591	0.44	449

At a given electron density, any ion can exist only over a certain range of temperatures (see figure 4.7). If several ions are observed in the same spatial region of the plas-

ma, the possible temperature of that plasma is limited. Although it is not certain that all the lines observed in each region of the plasma are emitted at the same time, this assumption would enable one to obtain a good estimate of the electron temperature.

Populations for the ions were taken from the collisional-radiative model (Lee, Whitten, Strout, 1985). By comparing the predicted populations of ions at both low densities (10^{14} cm^{-3}) where the coronal model would be expected to apply, and at the higher densities, the amount by which the coronal model holds can be found. At a temperature of 50eV, the two values differ by 20% for electron densities up to 10^{21} cm^{-3}. In the absence of better estimates of the electron density, the coronal model can be assumed to give a good description of the plasma conditions.

The results of this analysis of the central pinched plasma and the background plasma are presented in table 4.6. Two factors appear to affect the temperature in the plasma : the charging voltage; and pre-ionization. Pre-ionization in general appears to give a plasma with a higher temperature core of the order 100 - 130 eV. Plate 30 was taken with a smaller diameter nozzle, higher charging voltage, and no pre-ionization. Here lines between 24Å and 28Å have been positively identified as being due to Ar XV, and thus a temperature of 200eV must be present at some stage in the discharge. Lines due to Ar X and Ar XI are much fainter

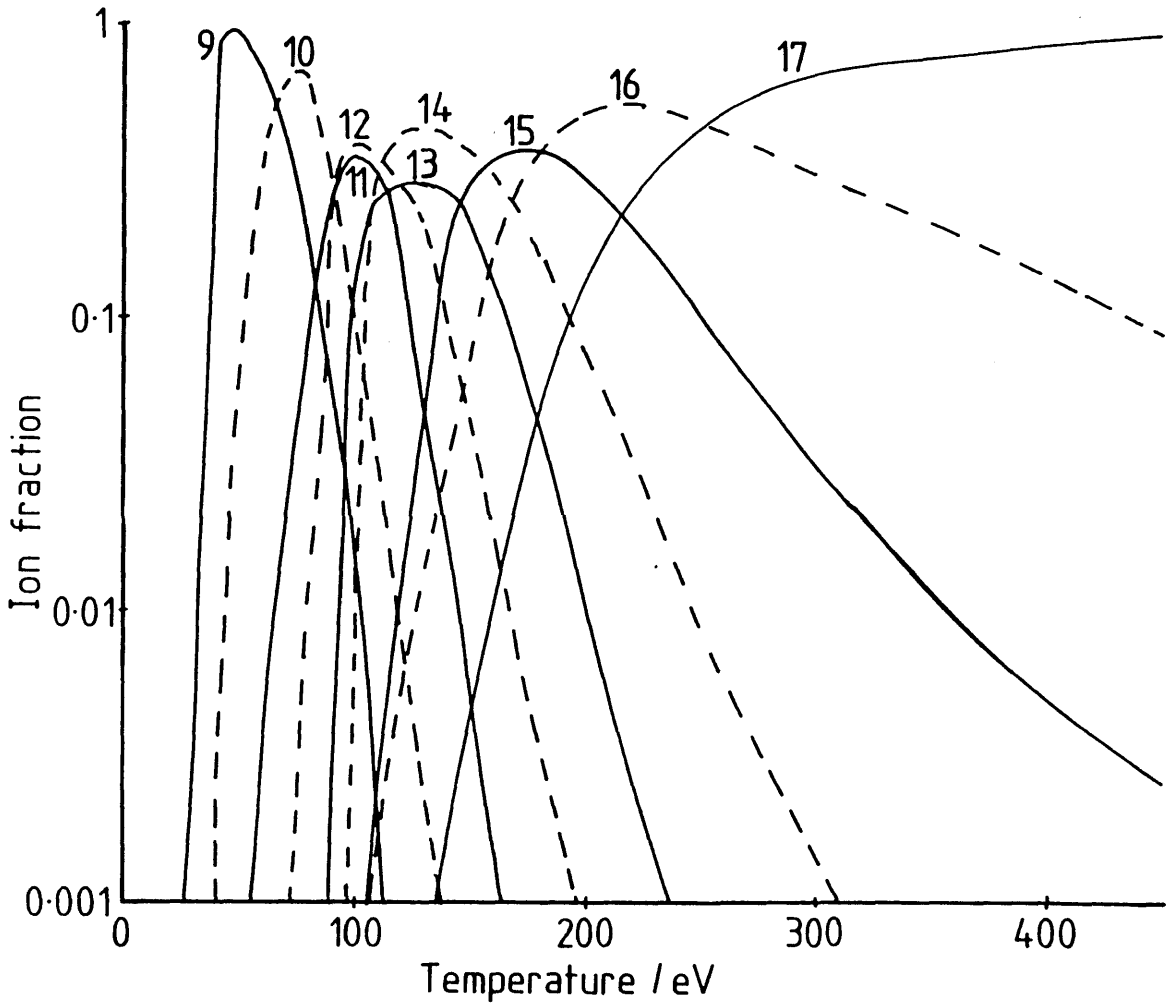


FIGURE 4.7 IONIZATION BALANCE FOR ARGON ASSUMING CORONAL EQUILIBRIUM

in this spectrum, implying a much higher core temperature. Comparison of the plates in figure 4.2 shows that the 5cm nozzle gives a slightly higher temperature with a brighter spectrum, implying the energy is dumped more efficiently into the plasma.

Table 4.6 Calculated temperatures for Plates in Figures 4.1-4.5

Figure No.	Plate	Species	Position in plasma	Temperature /eV
4.1	74	IX-X	background	70±20
		XI-XIII	centre	120±20
		XV?	centre	170±30
4.2A	50	IX-X	background	70±20
		X-XI	centre	90±20
4.2B	56	IX-X	background	70±20
		XI-XIII	centre	120±20
4.3A	30	IX-X	background	70±20
		XII-XIII	centre	120±20
		XV	centre	180±20
4.3B	65	IX-X	background	70±20
		XI-XIII	centre	120±20
4.5A	35	IX-X	background	70±20
		XII-XIII	centre	120±20
		XV	centre	180±20

The two Ar IX lines whose A-values are known, can be analysed to give an electron density. The absolute intensity of the lines can give the density of ions in the upper state of the transition using equation 2.3. 2.11 can then be used to give the ground state population, assuming the coronal model, and using the collisional excitation rate given by equation 2.12. The electron density can then be found with the aid of Lee´s calculations of the ionization of the plasma.

The results of this calculation are given in table 4.7. These results were calculated using plate 74, but as the intensities of these emission lines are similar for all the plates, similar results can be expected for the other plates described. The discrepancy may be due to uncertainty in the transition rates which are known only to within 50%, and the approximate expression used for the collisional excitation rate.

An electron density can also be found from the Ar XV lines seen in plate 30. Here A-values were taken from Fawcett (1984). The electron density was calculated by the same method, and was found to be of the order 10^{19} cm^{-3}, assuming a temperature of 150eV.

The validity of this method can be checked by comparing

the collisional excitation rate $X(T_e,g,p)$ with the radiative rate $A(p,q)$, giving the criterion :

$$n_e < \frac{A(p,s)}{X(T_e,g,s)} \qquad 4.1$$

For the levels in question, $n_e < 7 \times 10^{22}$ cm^{-3} for the coronal model to be satisfied at 100eV. Hence the coronal model is applicable to this plasma.

Table 4.7 Calculated electron densities for plate 30 (figure 4.3A) for duration 200 ns

Wavelength of line /Å	Intensity /J	$n_e n(z,g)$ /cm^{-6}	n_e /cm^{-3}	Plasma size/mm
48.73	0.13	8.8×10^{34}	3×10^{17}	11
49.18	0.13	2.3×10^{35}	5×10^{17}	11
25.92	0.072	2.3×10^{36}	1×10^{20}	0.4
27.05	0.042	1.4×10^{36}	1×10^{20}	0.4
27.59	0.047	1.2×10^{36}	2×10^{20}	0.4

CHAPTER 5 SPECTRA OF LOW Z DISCHARGES

5.1 INTRODUCTION

This chapter presents and analyses the spectra obtained from low Z plasmas (Z = 6 - 10). In addition to providing information about the plasma, the spectra provide good tests of both lineshape theory and the theory of satellite line wavelengths and intensities.

Spectra of CO_2, N_2 and Ne were obtained from the gas-puff. Section 5.2 analyses one particular CO_2 plate in detail and illustrates the main methods of analysis used. One of the most significant changes in the plasma parameters was caused by pre-ionizing the gas before the main discharge. The results and reasons for them are discussed in section 5.4. The spectra of neon are be discussed in section 5.5.

5.2 ANALYSIS OF CO_2 SPECTRUM

Two examples of the CO_2 spectrum from the gas-puff z-pinch are shown in figure 5.1, together with densitometer traces in figure 5.2. A listing of the lines seen together with their energies is given in table 5.1. The major resonance lines of both hydrogen-like and helium-like ions are seen together with helium-like and lithium-like dielectronic satellites.

Table 5-1 Wavelengths and intensities observed in CO_2

Wavelength /Å	Intensity /J	Ion	Transition
15.18	0.12	OVIII	4-1
16.01	0.27	OVIII	3-1
17.2	0.098	OVII	$1s6p-1s^2$
17.39	0.19	OVII	$1s5p-1s^2$
17.77	0.36	OVII	$1s4p-1s^2$
18.63	0.57	OVII	$1s3p-1s^2$
18.97	1.05	OVIII	2-1
19.32	0.16	OVII	2s2p-1s2p
19.39	0.11	OVII	$2p^2-1s2p$
21.60	1.24	OVII	$1s2p(^1P)-1s^2$
21.80	0.33	OVII	$1s2p(^3P)-1s^2$
22.02	0.25	OVI	$1s2s2p-1s^22s$
22.11	0.17	OVI	$1s2p^2-1s^22p$
24.78	0.11	NVII	2-1
24.95	0.044	NVI	$1s3p-1s^2$
25.87	0.077	CVI	7-1
26.03	0.18	CVI	6-1
26.36	0.357	CVI	5-1
26.99	0.8	CVI	4-1
28.47	0.89	CVI	3-1
28.63	0.15	CV?	
15.176	0.12	OVIII	4-1
31.7	0.046	?	

Wavelength /Å	Intensity /J	Ion	Transition
32.188	0.055	CV	$1s7p-1s^2$
32.4	0.098	CV	$1s6p-1s^2$
32.75	0.26	CV	$1s5p-1s^2$
33.43	0.45	CV	$1s4p-1s^2$
33.74	1.3	CVI	2-1
34.31	0.078	CV	2s2p-1s2s
34.53	0.10	CV	2s2p-1s2s
34.59	0.08	CV	$2p^2-1s2p$
34.71	0.11	CV	$2p^2-1s2p$
35.07	0.67	CV	$1s3p-1s^2$
40.27	0.77	CV	$1s2p(^1P)-1s^2$
40.73	0.055	CV	$1s2p(^3P)-1s^2$
41.33	0.068	CIV	$1s2s2p-1s^22s$
41.55	0.062	CIV?	$1s2p^2-1s^22p$?

Densitometer traces across the main lines in the spatially resolved spectra are shown in figure 5.3. They show that most of the radiation is emitted by a relatively diffuse plasma of roughly 2mm in diameter, with the less highly ionized species coming from a slightly larger volume of plasma. The experimental conditions for the spectra are listed in table 5.2.

Table 5.2 Experimental Conditions for the spectra in chapter 5

Figure number	Plate no.	$\alpha/^{o}$	S/μm	grating	number of shots	pre-ioniz-ation	charging voltage /kV	pressure /atmos
5.1A	74	2	2	2	1	Yes	27	8.5
5.1B	75	2	5x10	1	1	Yes	27	8.5
5.18	99	2	8	1	6	No	27	6
5.22A	71	2	5x100	2	1	Yes	27	8.5
5.22B	72	2	2	2	1	Yes	27	8.5

Figure 5·1

A Argon spectrum

B Carbon dioxide spectrum

C Spatially resolved carbon dioxide spectrum

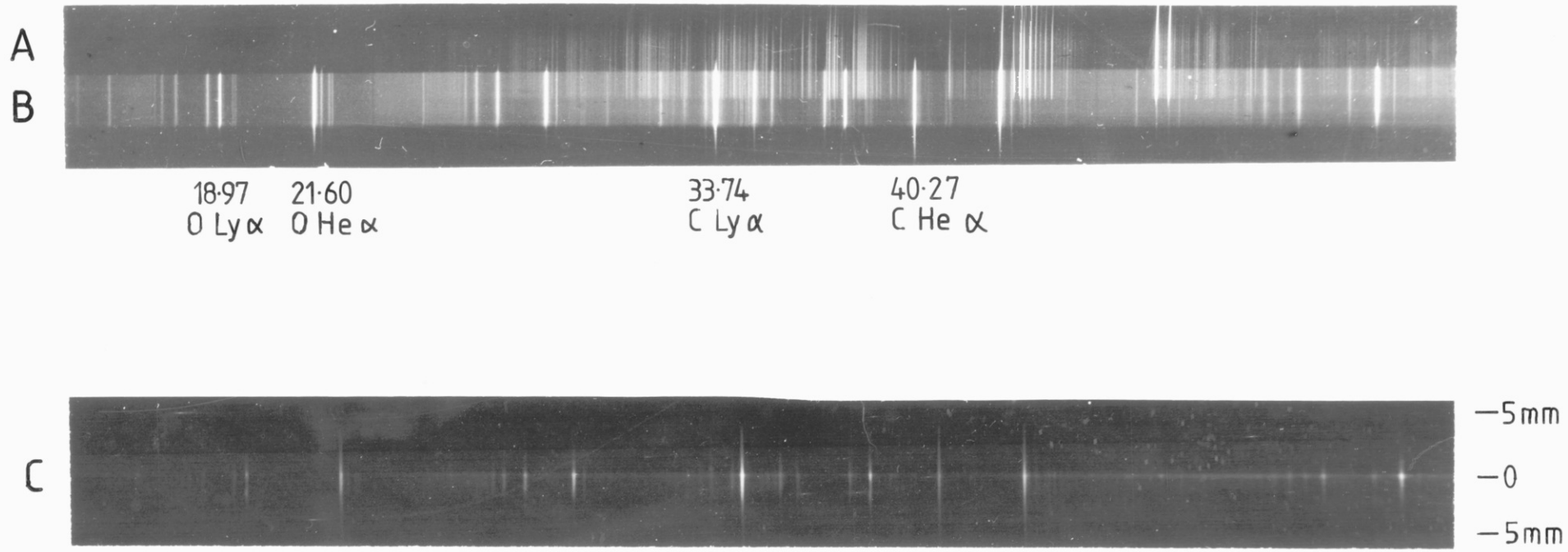


FIGURE 5.2 DENSITOMETER TRACE OF CARBON DIOXIDE SPECTRUM

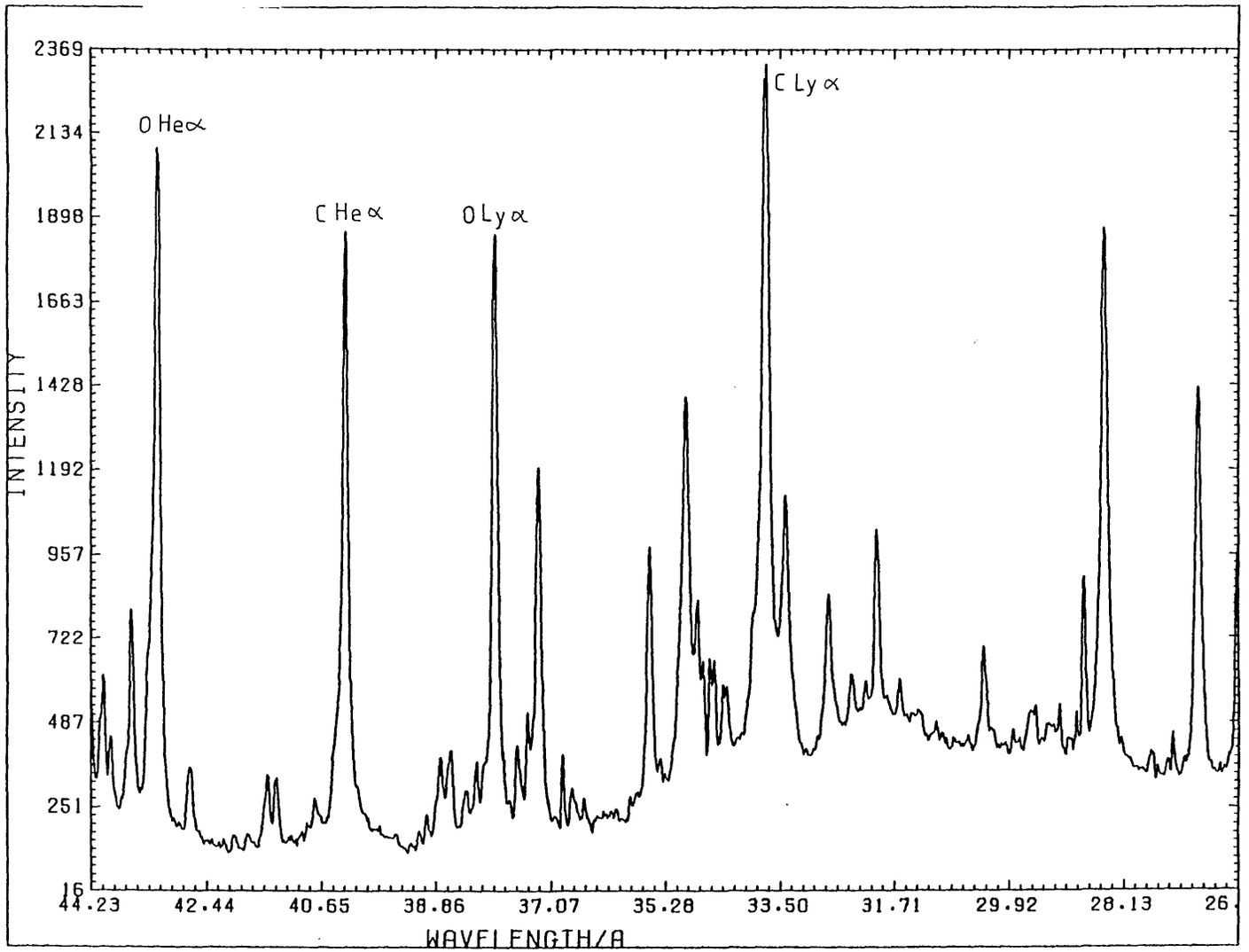


Figure 5.2 continued

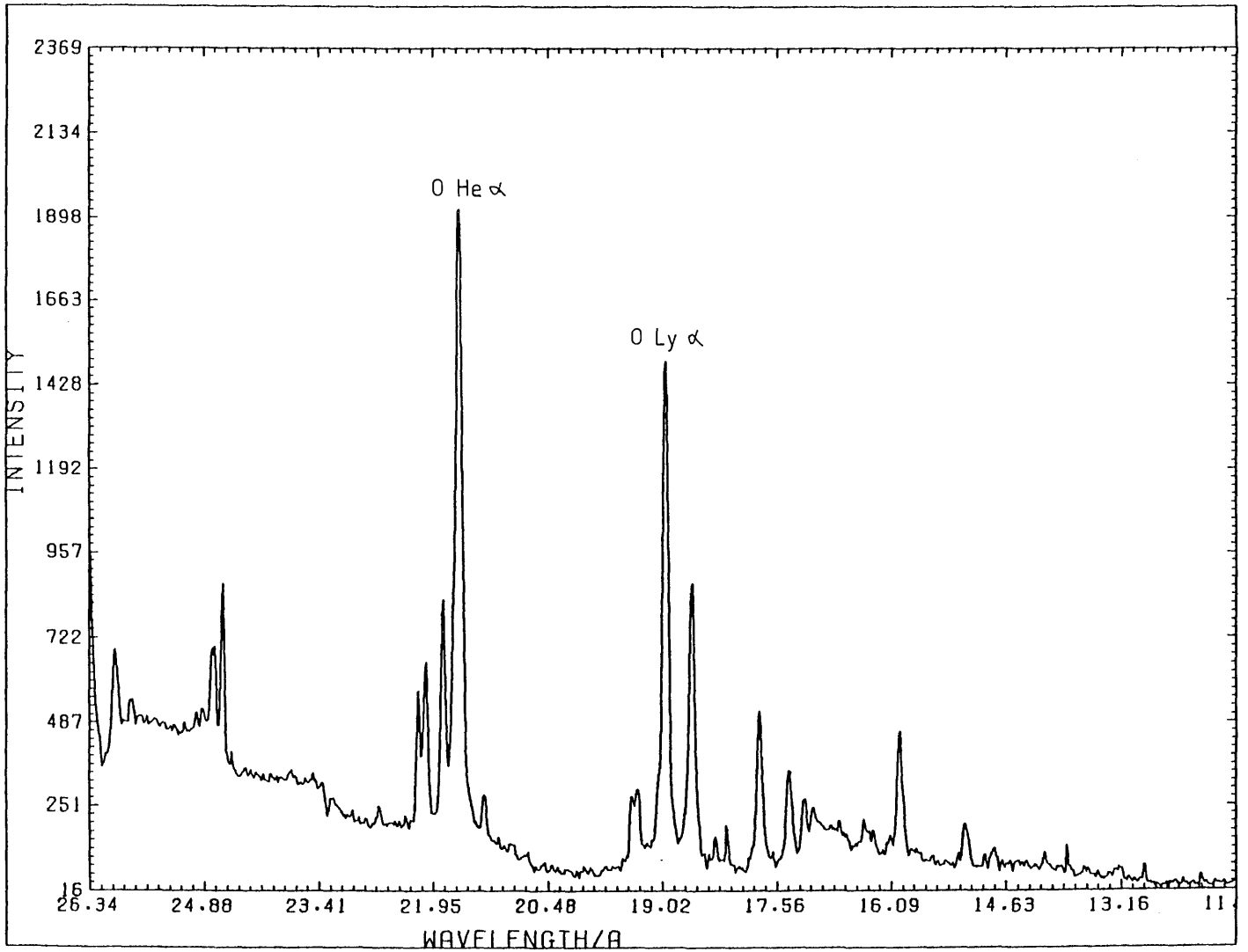
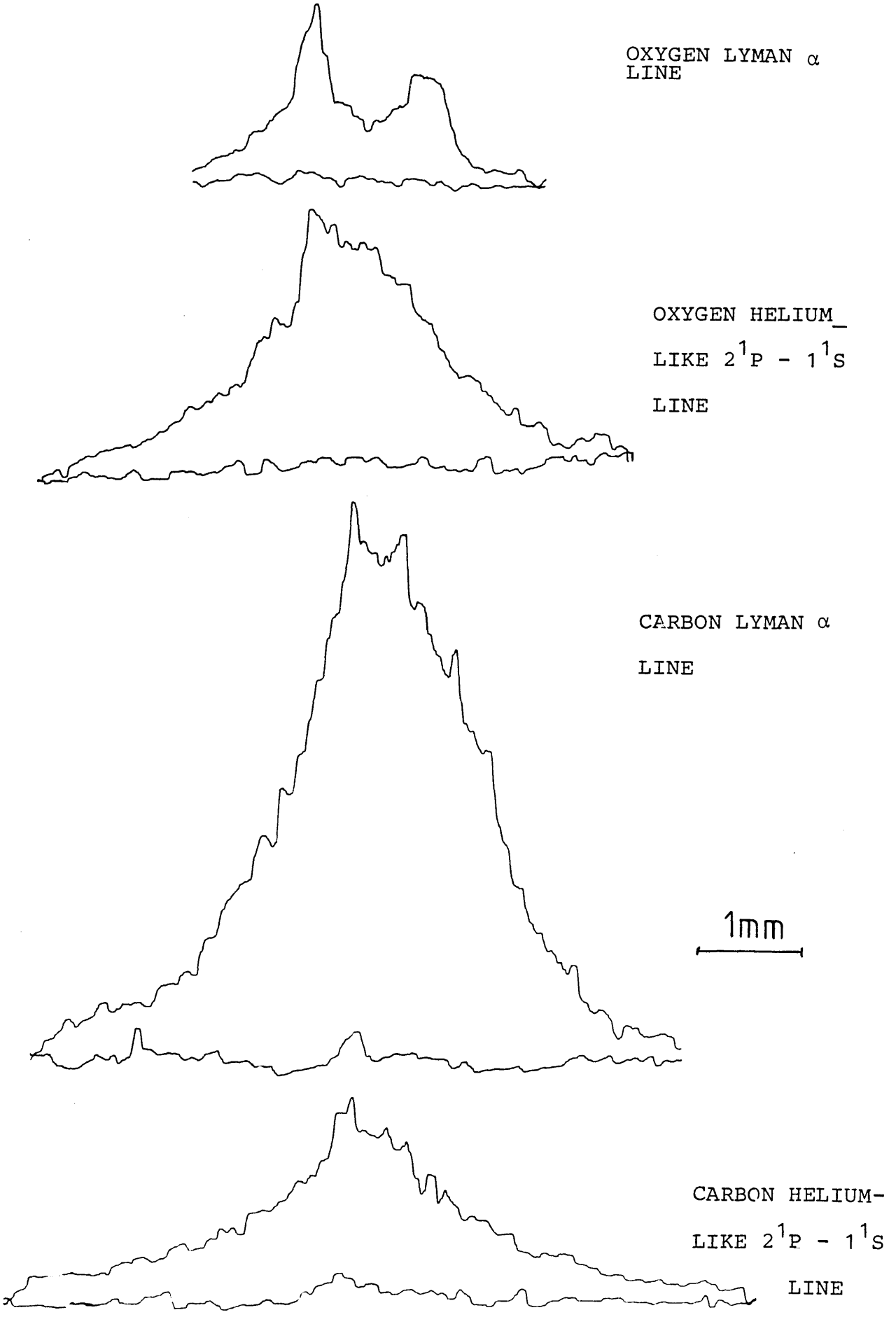


FIGURE 5.3 RADIAL DENSITOMETER TRACE ACROSS MAJOR LINES IN CARBON DIOXIDE SPECTRUM



5.2.1 ELECTRON TEMPERATURE

Three basic methods were outlined in chapter 2 in order to obtain the electron temperature, namely :

(i) Slope of the soft x-ray continuum (section 2.4).

(ii) Satellite / resonance line intensity ratio (section 2.3.3)

(iii) Ionization of the plasma (section 2.2.2 and 2.2.4)

The results obtained using these methods are presented in the following sections.

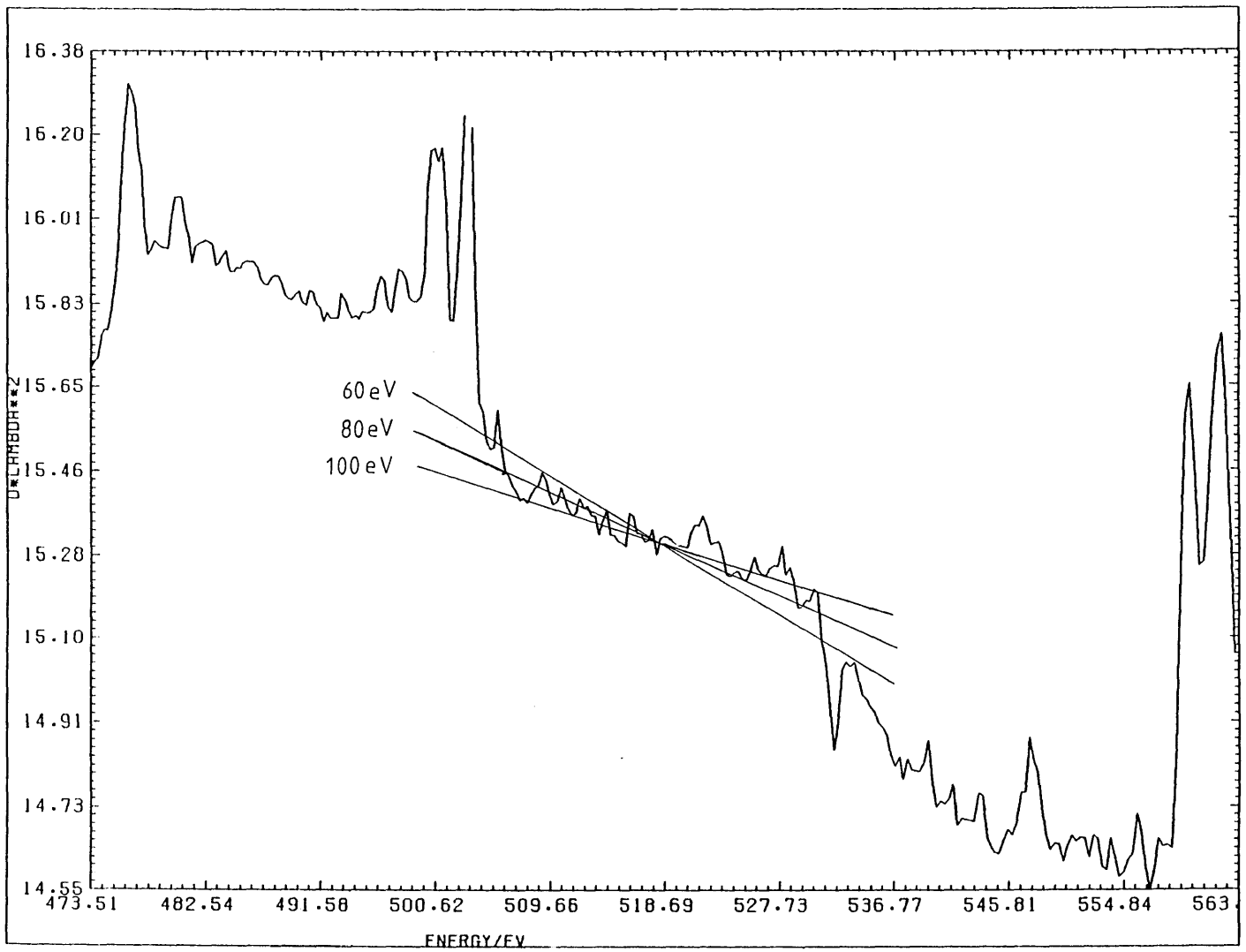
5.2.1.1 SLOPE OF THE SOFT X-RAY CONTINUUM

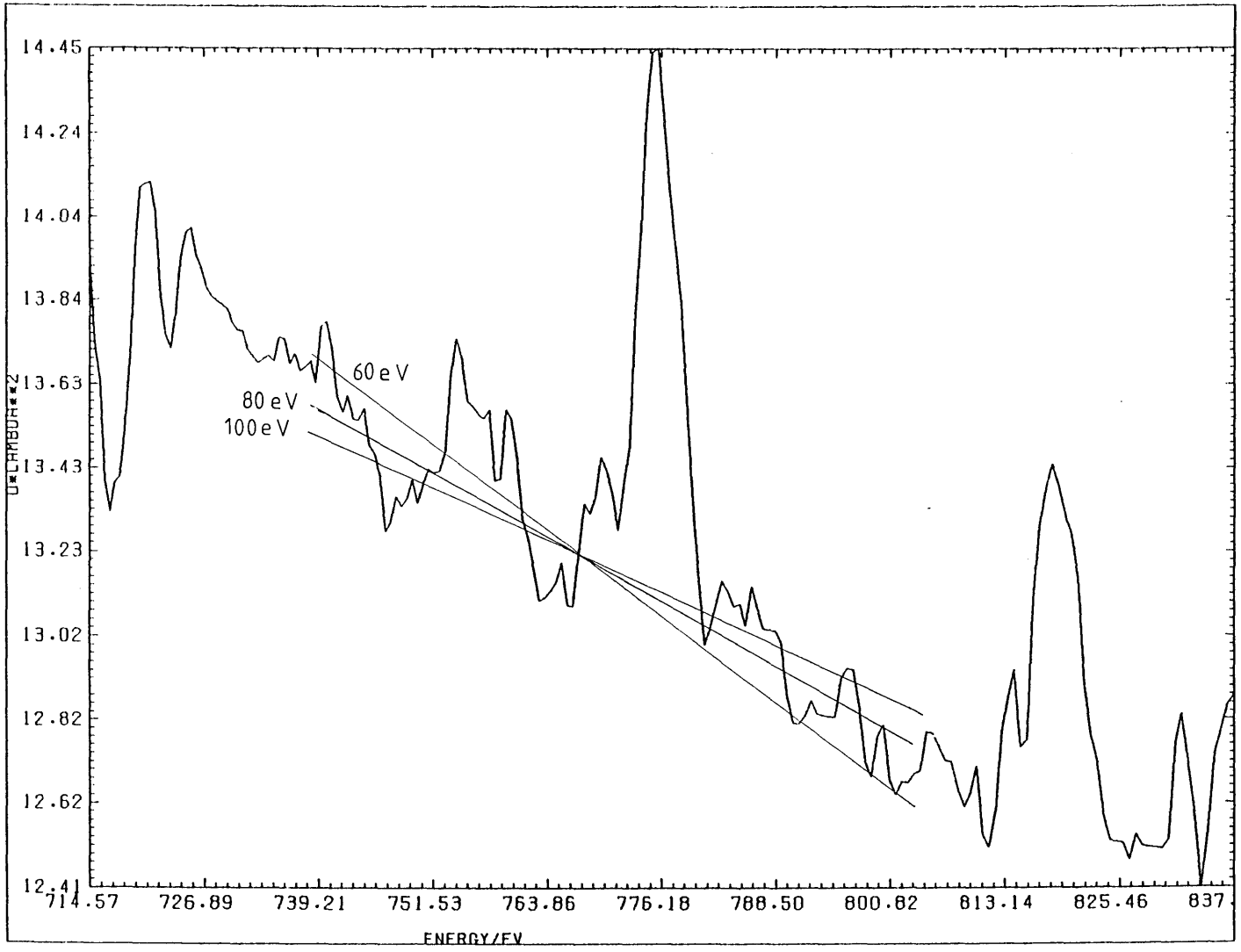
The equation for the intensity of the soft x-ray continuum (equation 2.28) can be re-written in terms of the emitted intensity per Angstrom $N(\lambda)$ giving:

$$\ln\left(N(\lambda) \frac{\lambda^2}{c} \right) = \frac{-hc}{\lambda k T_e} + \text{const} \qquad 5.1$$

$N(\lambda)$ can then be related to the plate density by using the equation for the sensitivity of the spectrograph (equation 3.15). It can be seen from the above equation that a plot of $\ln N(\lambda)\lambda^2/c$ against the photon energy in eV should be

FIGURE 5.4 SLOPE OF THE SOFT X-RAY CONTINUUM FOR CARBON AND OXYGEN




14.45
14.24
14.04
13.84
13.63
13.43
13.23
13.02
12.82
12.62
12.41
U*LAMBDA**2
60 eV
80 eV
100 eV
714.57
726.89
739.21
751.53
763.86
776.18
788.50
800.82
813.14
825.46
837
ENERGY/EV

a straight line of gradient $1/kT_e$ where kT_e is in eV.

Figure 5.4 shows the results obtained for the carbon and oxygen free-bound continua shown on figure 5.2. A least squares fit yields a temperature of (80±20) eV in both carbon and oxygen continua.

5.2.1.2 SATELLITE / RESONANCE LINE INTENSITY RATIO

The electron temperature from the observed satellite / resonance line intensity ratio was obtained by comparison with the theoretically predicted ratio. Two theoretical methods were used. First, the expected intensity ratio was calculated by assuming that the resonance line was in LTE with higher states, and the satellite line was populated solely by dielectronic recombination (equation 2.24). Secondly, the ratio was calculated for a series of temperature using the collisional - radiative code described in section 2.4.5, at the expected electron densities.

The lines chosen, together with the wavelengths and intensities are listed in table 5.3. The satellites chosen were the lithium-like 'jkl' satellite line and the helium-like $2p^2\ (^1D) - 1s2p\ (^1P)$. The highest n visible resonance line was chosen in order to minimize the effect of opacity. These were the $1s5p - 1s^2$ and 5p - 1s lines of helium - like and hydrogenic ions respectively. The effect of opacity could be estimated by comparing the result with the

result obtained by using the next lower n line. The results are given in table 5.5.

Table 5.3 Lines used for the evaluation of kT_e and N_e

Ion	Transition	Wavelength /Å	Radiative rate /s^{-1}	Autoionizing rate / s^{-1}
CVI	5-1	26.357	5.35×10^{9}	
	4-1	26.99	1.66×10^{10}	
CV	$1s5p-1s^2$	32.75	2×10^{9}	
	$1s4p-1s^2$	33.426	5.7×10^{9}	
	$2p^2(^1D)-1s2p$	34.709	1.43×10^{12}	3.73×10^{14}
	$2p^2(^3P)-1s2p$	34.59	1.42×10^{12}	4.6×10^{10}
	$2s2p(^3P)-1s2s$	34.53	7.09×10^{11}	1.35×10^{13}
CIV	jkl	41.56	3.98×10^{11}	1.86×10^{14}
	ad	41.44	1.18×10^{12}	2.1×10^{10}
	qr	41.36	7.18×10^{11}	5×10^{12}
OVIII	5-1	14.821	1.69×10^{10}	
	4-1	15.176	5.34×10^{10}	
OVII	$1s4p-1s^2$	17.77	1.5×10^{10}	
	$125p-1s^2$	17.39	5×10^{9}	
	$2p^2(^1D)-1s2p$	19.39	4.67×10^{12}	3.73×10^{14}
	$2p^2(^3P)-1s2p$	19.34	4.64×10^{12}	2.15×10^{11}
	$2s2p(^3P)-1s2s$	19.30	2.31×10^{12}	1.35×10^{13}
OVI	jkl	22.13	1.51×10^{12}	1.86×10^{14}
	ad	22.06	4.52×10^{12}	1.5×10^{12}

Ion	Transition	Wavelength /Å	Radiative rate $/s^{-1}$	Autoionizing rate / s^{-1}
	qr	22.02	2.75×10^{12}	5.51×10^{13}
NeX	2-1	12.134	4.7×10^{12}	
NeIX	$1s3p-1s^2$	11.544	8.87×10^{12}	
NeVIII	ad	13.67	1.23×10^{13}	5.5×10^{12}
	qr	13.65	7.5×10^{13}	5×10^{13}
	jkl	13.71	4.1×10^{12}	1.86×10^{14}
	$1s^2 2s-1s^2 4p$	67.38	3.6×10^{10}	

5.2.1.3 IONIZATION OF THE PLASMA

The ionization of the plasma is a highly sensitive function of electron temperature but can be estimated independently from it. The method of analysis is as follows. Firstly, equation 2.5 was used to obtain the ratio of bare to hydrogen-like ions from the intensity ratio of hydrogen-like and helium-like lines. The ratio of hydrogen-like to helium-like ions was obtained from equation 2.25, which relates the ratio to the ratio of helium-like to lithium-like dielectronic satellites. The ionization predicted by the collisional-radiative model of Lee at a series of temperatures was then compared to the result, and the electron temperature obtained. The predicted ionization as a function of temperature is plotted for carbon and oxygen in figures 5.5 and 5.6. Wavelengths and

FIGURE 5.5 IONIZATION BALANCE FOR OXYGEN AT 10^{21} CM^{-3}

calculated from Lee Whitten Strout (1984)

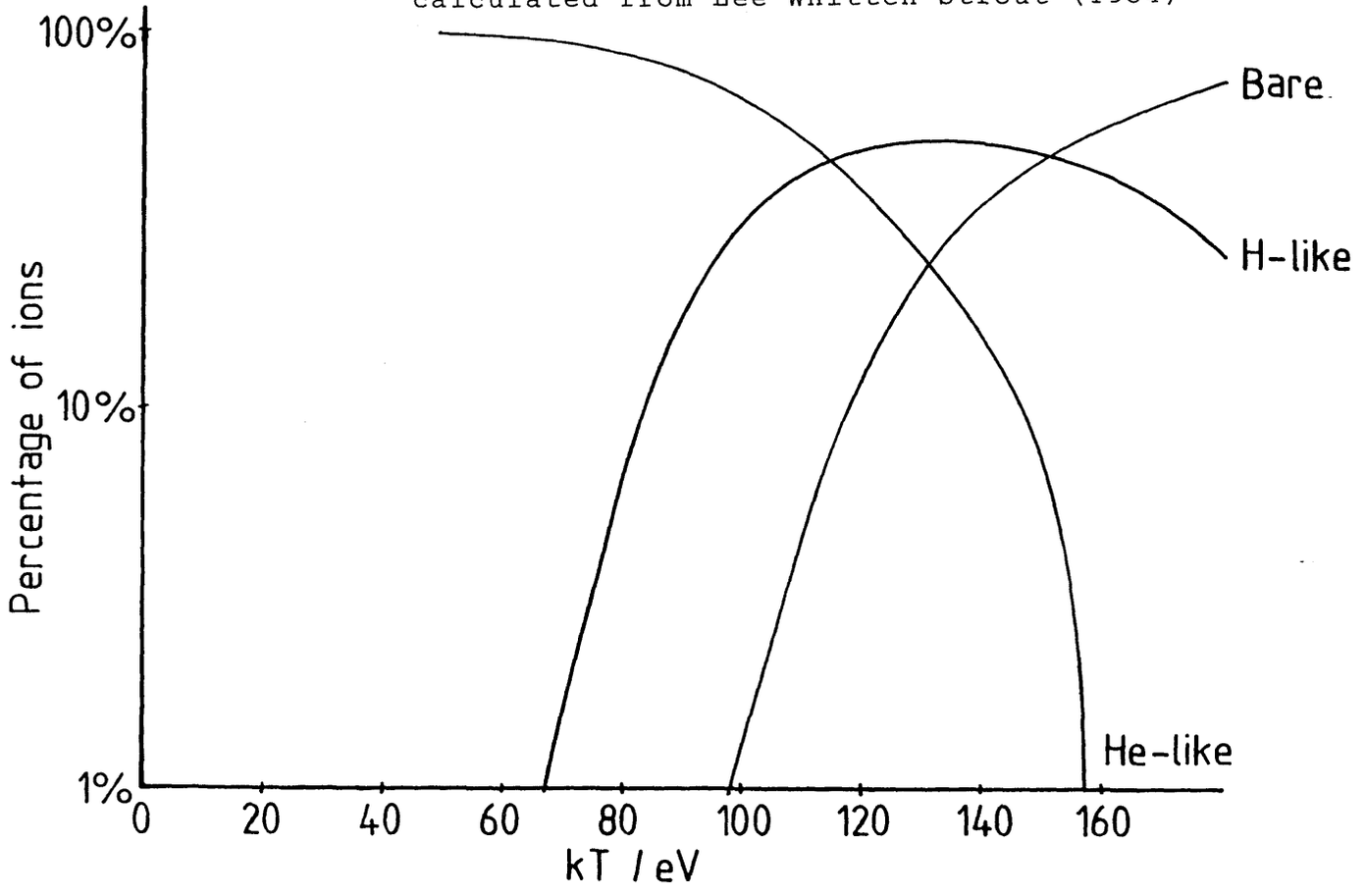
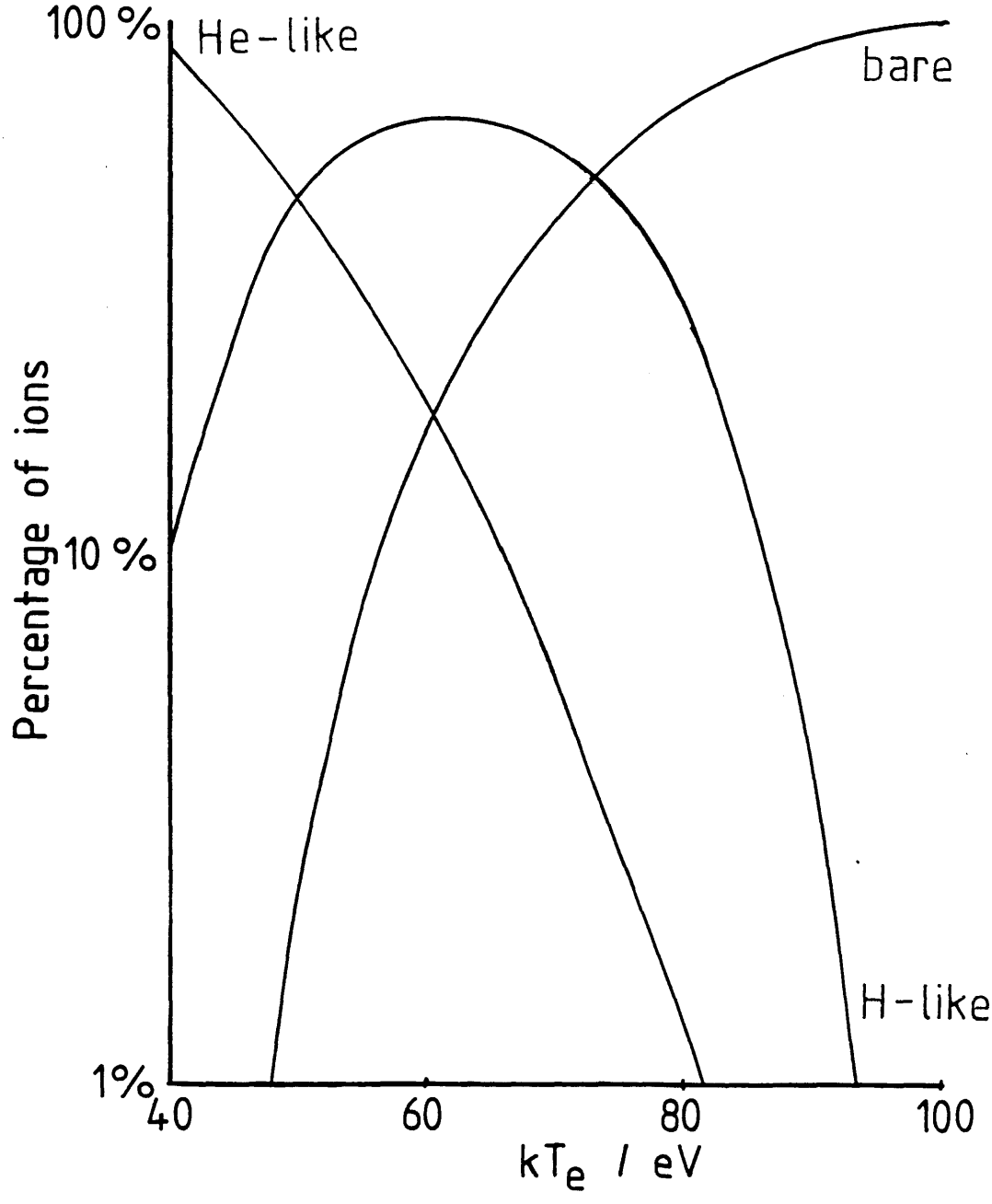


FIGURE 5.6 IONIZATION BALANCE FOR CARBON AT 10^{20} CM^{-3}

calculated from Lee Whitten Strout (1984)



intensities for the lines used are given in table 5.3. The results are summarized in table 5.4.

Table 5.4 Ionization Balance of Carbon Dioxide Plasma

Line ratio	Diagnostic	Carbon	Oxygen
5-1 / $1s5p-1s^2$	n_B/n_H	1.27±0.4	
4-1 / $1s4p-1s^2$	n_B/n_H		0.29±0.04
$\frac{2p^2(^1D)-1s2p}{jkl}$	n_H/n_{He}	?	0.57±0.1
	n_B	0.52	0.095
	n_H	0.41	0.33
	n_{He}	0.07	0.58
	kT_e	74±5 eV	115±5 eV

5.2.2 THE ELECTRON DENSITY

Two methods were used to estimate the electron density. These are analysis of:

(i) Satellite line intensity ratios.

(ii) Spectral line broadening.

5.2.2.1 SATELLITE LINE INTENSITY RATIOS

In order to obtain the electron density from the dielectronic satellite line, the spectra were fitted as described in section 2.3. Typical fits of the satellites are shown in figures 5.7 - 5.11, for both of the plates in figure 5.1. The densities obtained are:

Carbon Ly α satellites : $2.5\pm1 \times 10^{20}$ cm^{-3}

Carbon He α satellites : ?

Oxygen Ly α satellites : $6\pm4 \times 10^{20}$ cm^{-3}

Oxygen He α satellites : $6\pm1 \times 10^{20}$ cm^{-3}

The fit for the helium-like satellites in carbon was poor. Figure 5.10 shows that neither the predicted intensities nor the predicted wavelengths correspond to the experimental spectra. It should be noted that at the expected temperature of 60eV, the $2p^2$ (^1D)/jkl satellite intensity ratio would be about 12. In this case, the jkl satellite line would not be expected to be seen at all. As the wavelength of this feature corresponds more closely with the forbidden 1s2s (^3S) - $1s^2$ line, it is possible that this feature has been misinterpreted. However, the forbidden line would not be expected at electron densities greater than 10^{14} cm^{-3}, indicating that if the feature is due to the forbidden line, it must be formed from a high temperature but low density plasma. More evidence of this would be needed in order to confirm this.

5.2.2.2 LINE BROADENING

The method used to obtain the electron density and ion density x length product is described in section 2.6.4. In the spectrum analysed, carbon lines up to n=6 were observed, and line profiles of Ly β, γ and δ were used to obtain

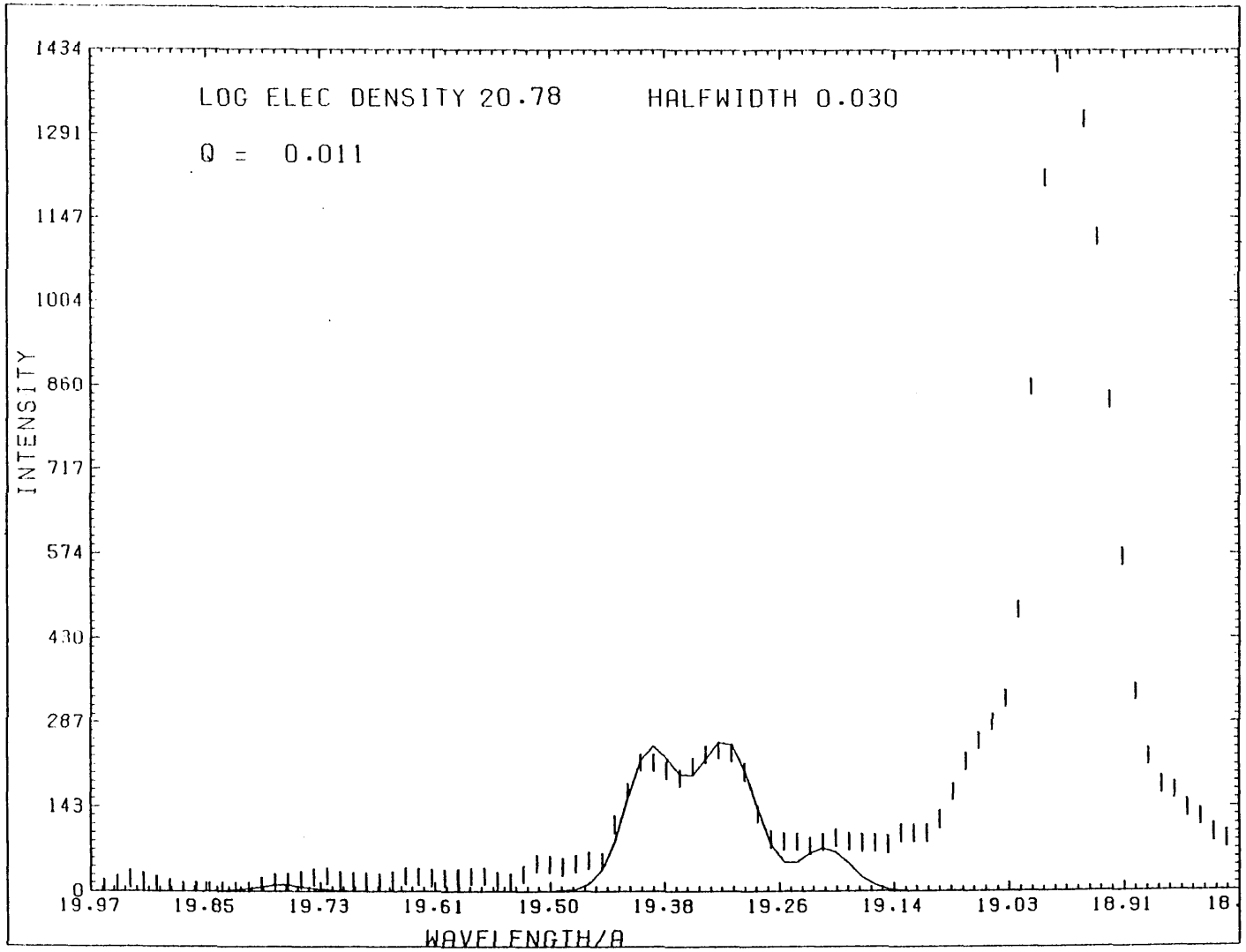
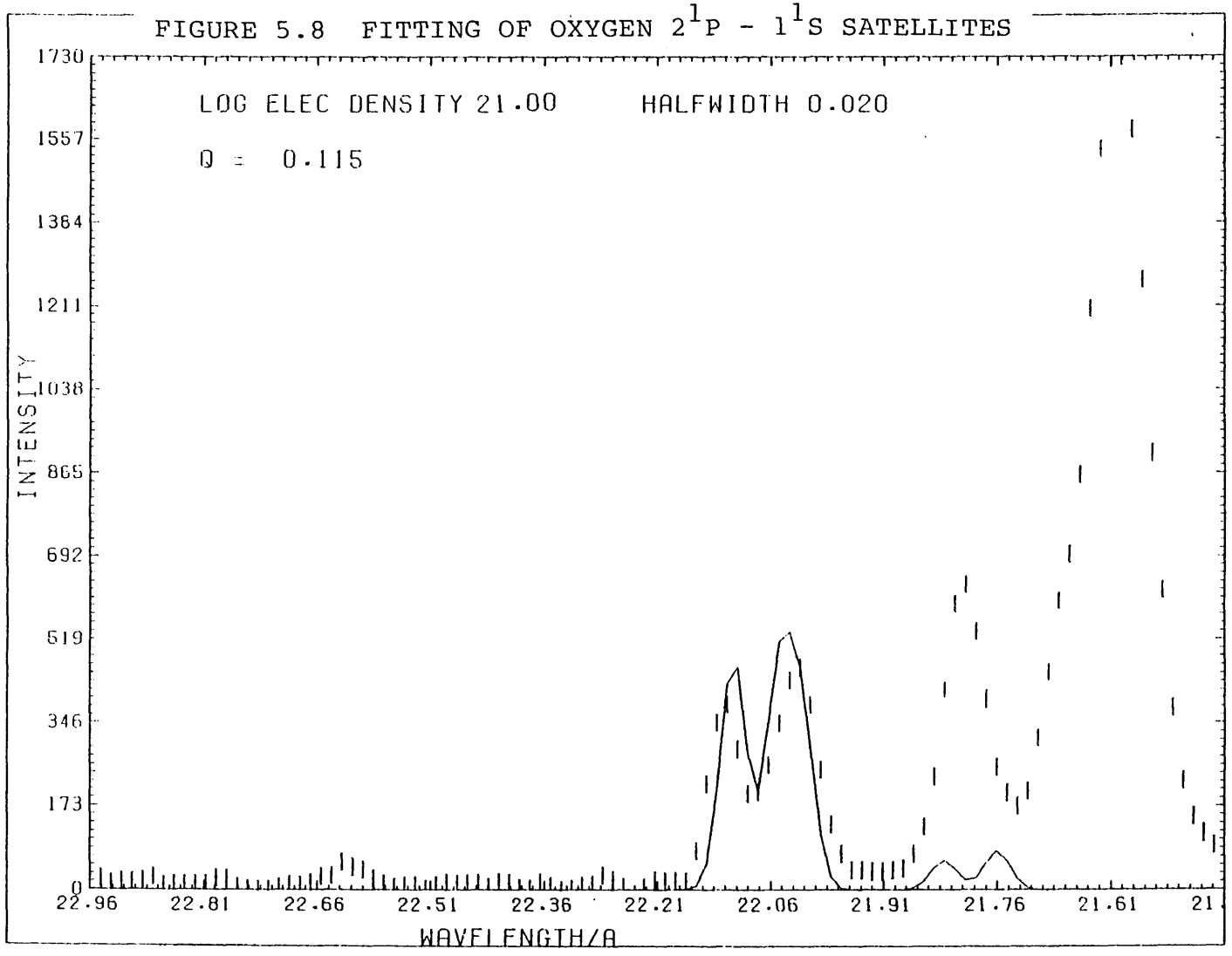


FIGURE 5.7 FITTING OF OXYGEN LYMAN α SATELLITES

FIGURE 5.8 FITTING OF OXYGEN $2^1P - 1^1S$ SATELLITES



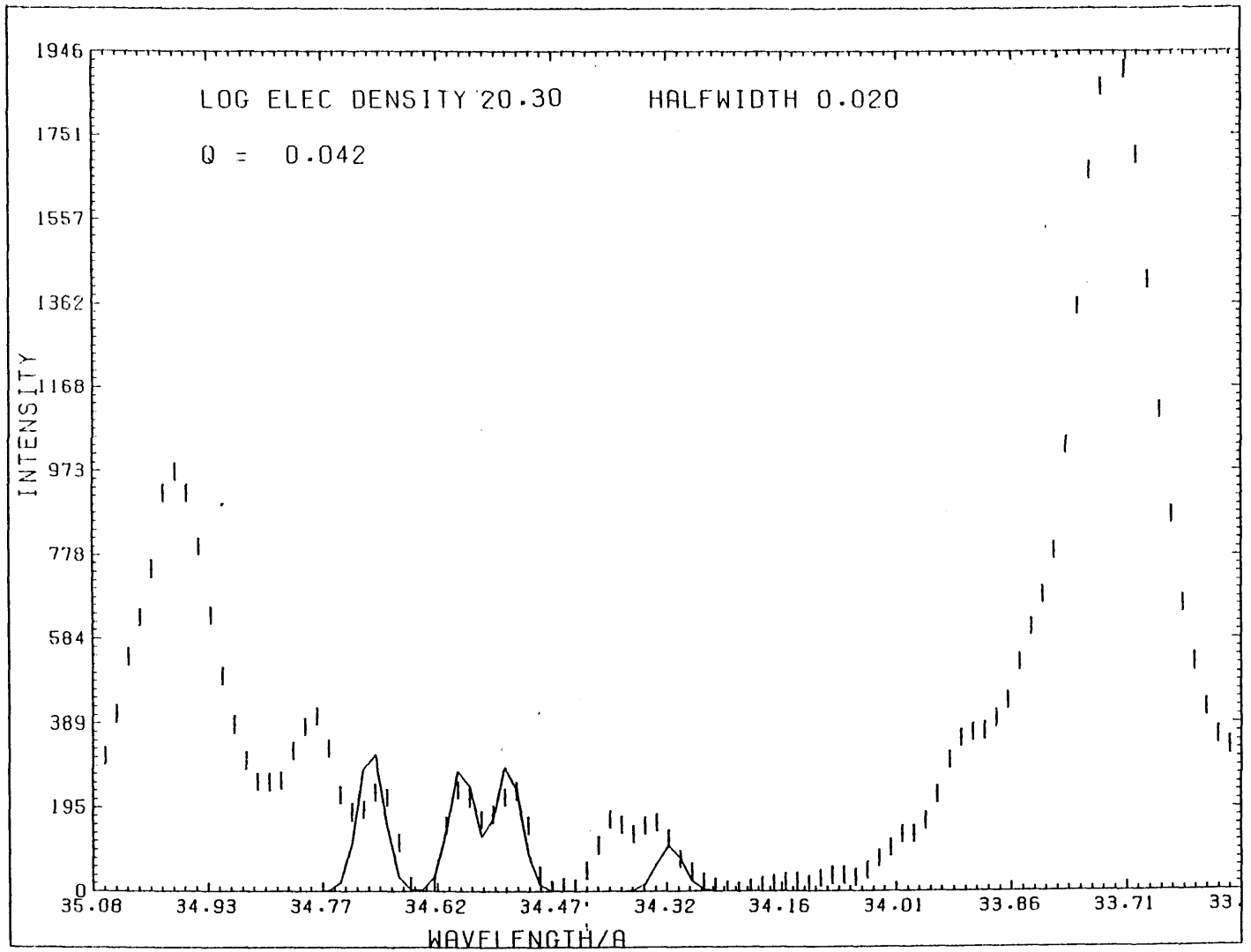


FIGURE 5.9 FITTING OF CARBON LYMAN α SATELLITES

| experimental

____ theoretical

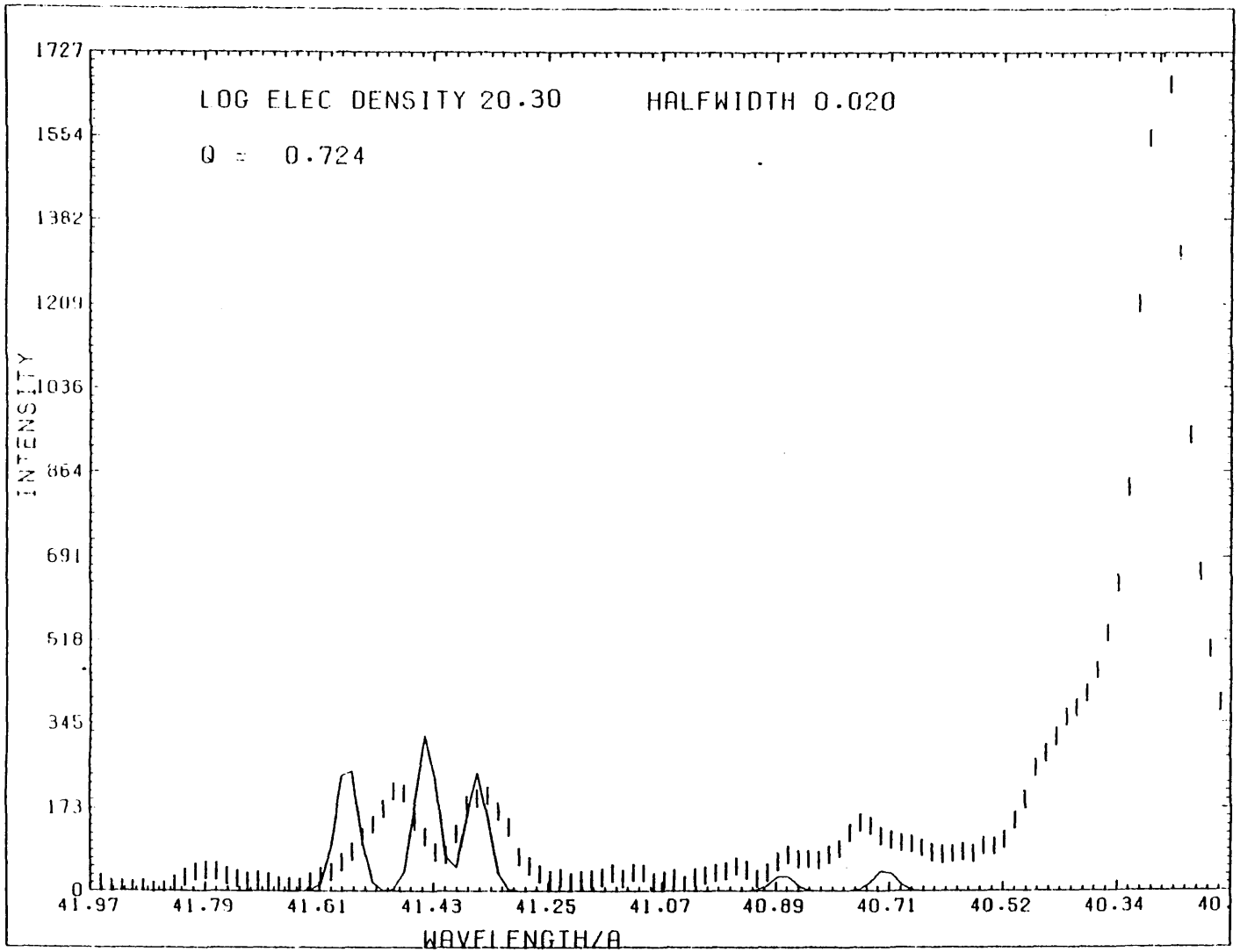


FIGURE 5.10 FITTING OF CARBON $2^1P - 1^1S$ SATELLITES USING GABRIEL'S WAVELENGTHS

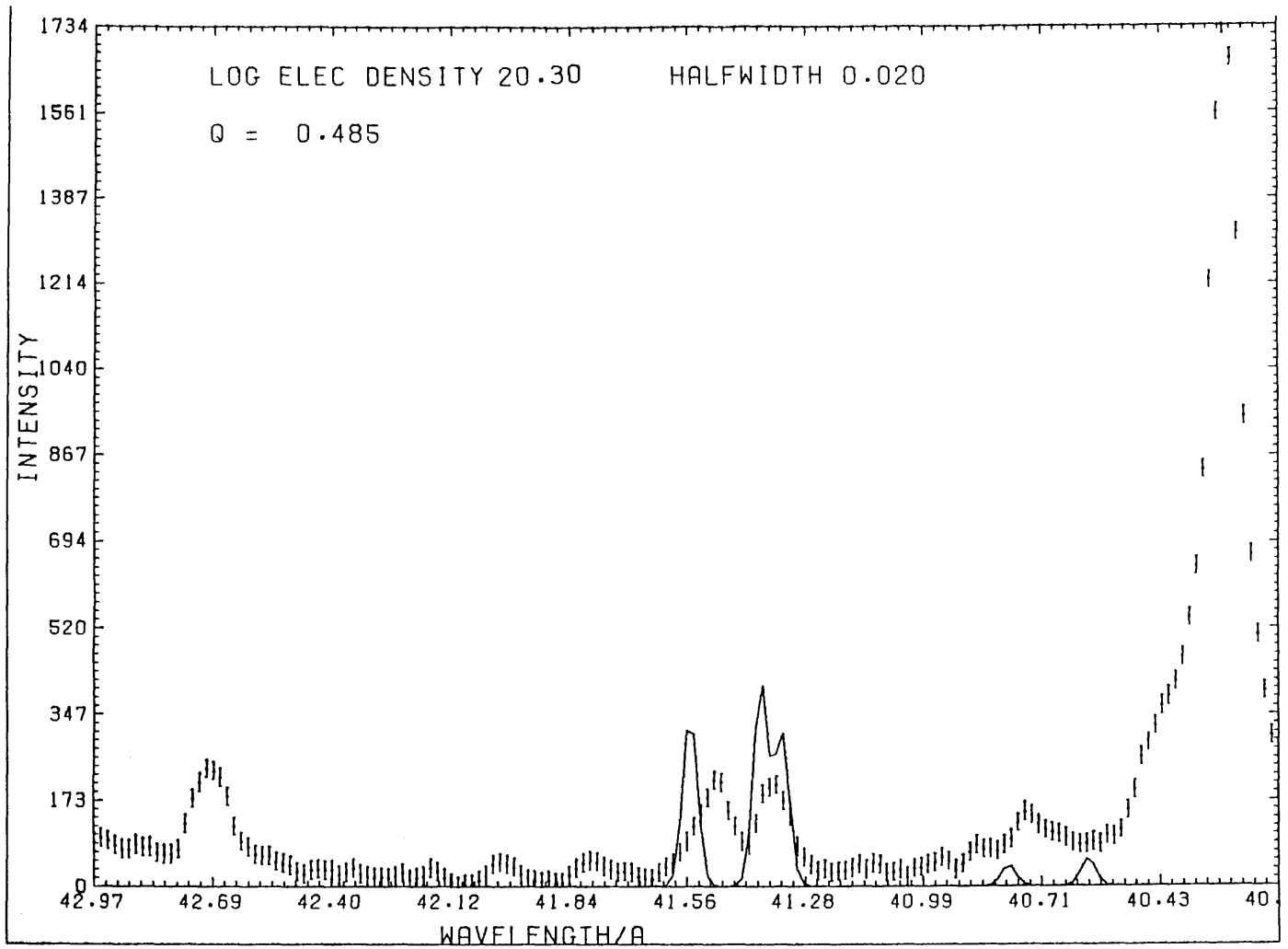


FIGURE 5.11 FITTING OF CARBON $2^1P - 1^1S$ SATELLITES USING VAINSTEIN AND SAFRANOVA WAVELENGTHS

the density. Figures 5.12 and 5.13 show the resulting graphs of electron density against ion density x length. Also marked is the expected average ion density x length assuming an emitting sphere of diameter 3mm, and the ionization measured (section 2.2.2). The shaded region represents the condition where more than 60% of the ions are H-like, and is forbidden in all models. The best fit is at the following conditions:

Carbon electron density	: $1.5\pm0.5 \times 10^{20}$ cm^{-3}
Carbon ion density x length	: $2.5\pm0.5 \times 10^{18}$ cm^{-3}
Oxygen electron density	: $6 \pm 4 \times 10^{20}$ cm^{-3}
Oxygen ion density x length	: $6 \pm 4 \times 10^{18}$ cm^{-3}

Example line profiles are given in figures 5.14 and 5.15. It can be seen that most of the lines fit well to the spectra, with the exception of Lyα , which is much broader than would be expected. As the opacity of Lyα at these conditions is very large, the most probable explanation of the poor fit is that the simple estimate of opacity broadening is no longer valid. This would break down if re-emission of absorbed radiation would be important. This would be most important in the centre of the line profile. Photons absorbed near line centre would be re-emitted over the whole profile, having the effect of broadening the line further.

The results for the fitting of oxygen lines are given in

FIGURE 5.12 FITTING OF CARBON LYMAN LINES FOR SPECTRUM IN FIGURE 5.18

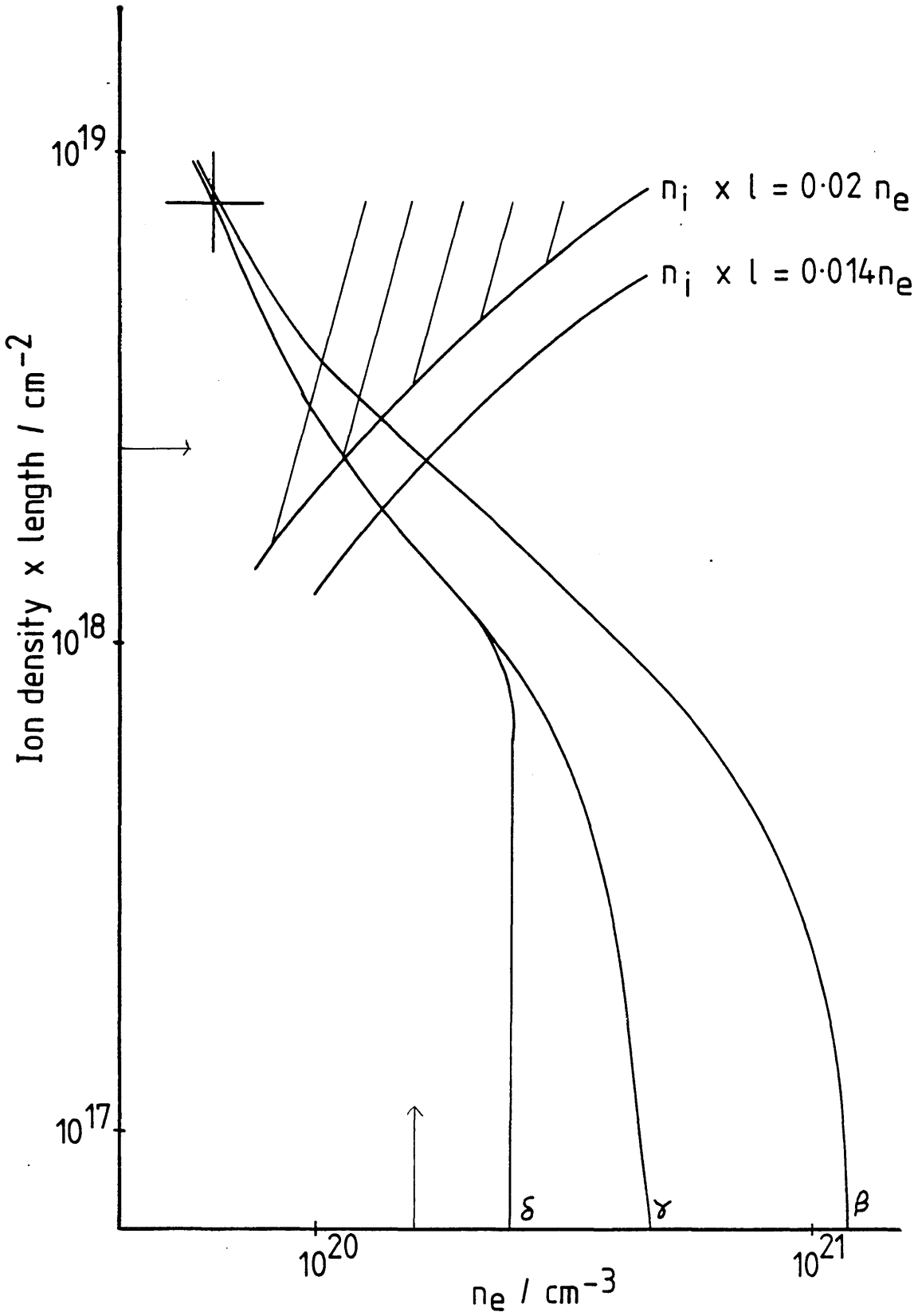


FIGURE 5.13 FITTING OF CARBON LYMAN LINES FOR SPECTRUM IN FIGURE 5.1C

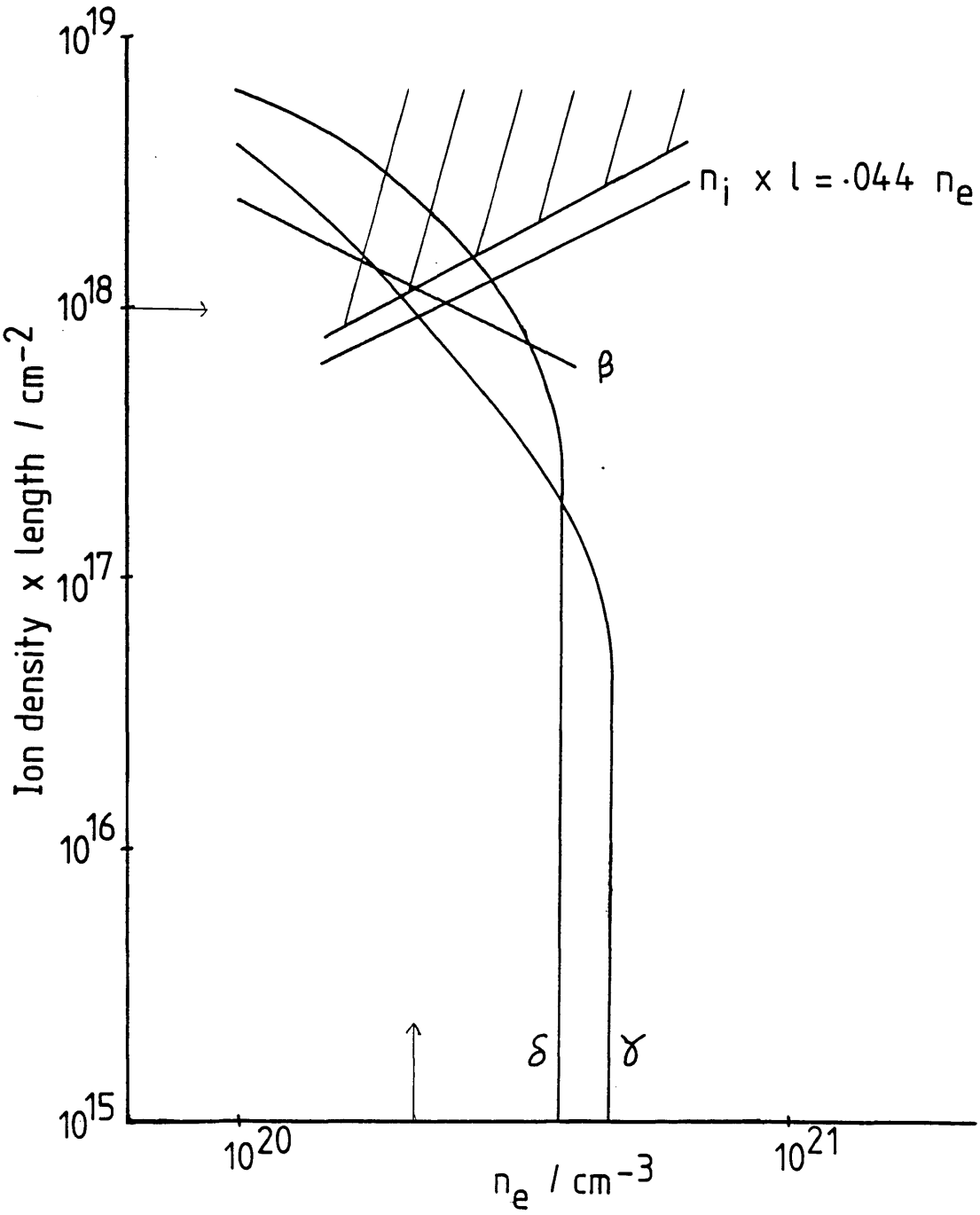
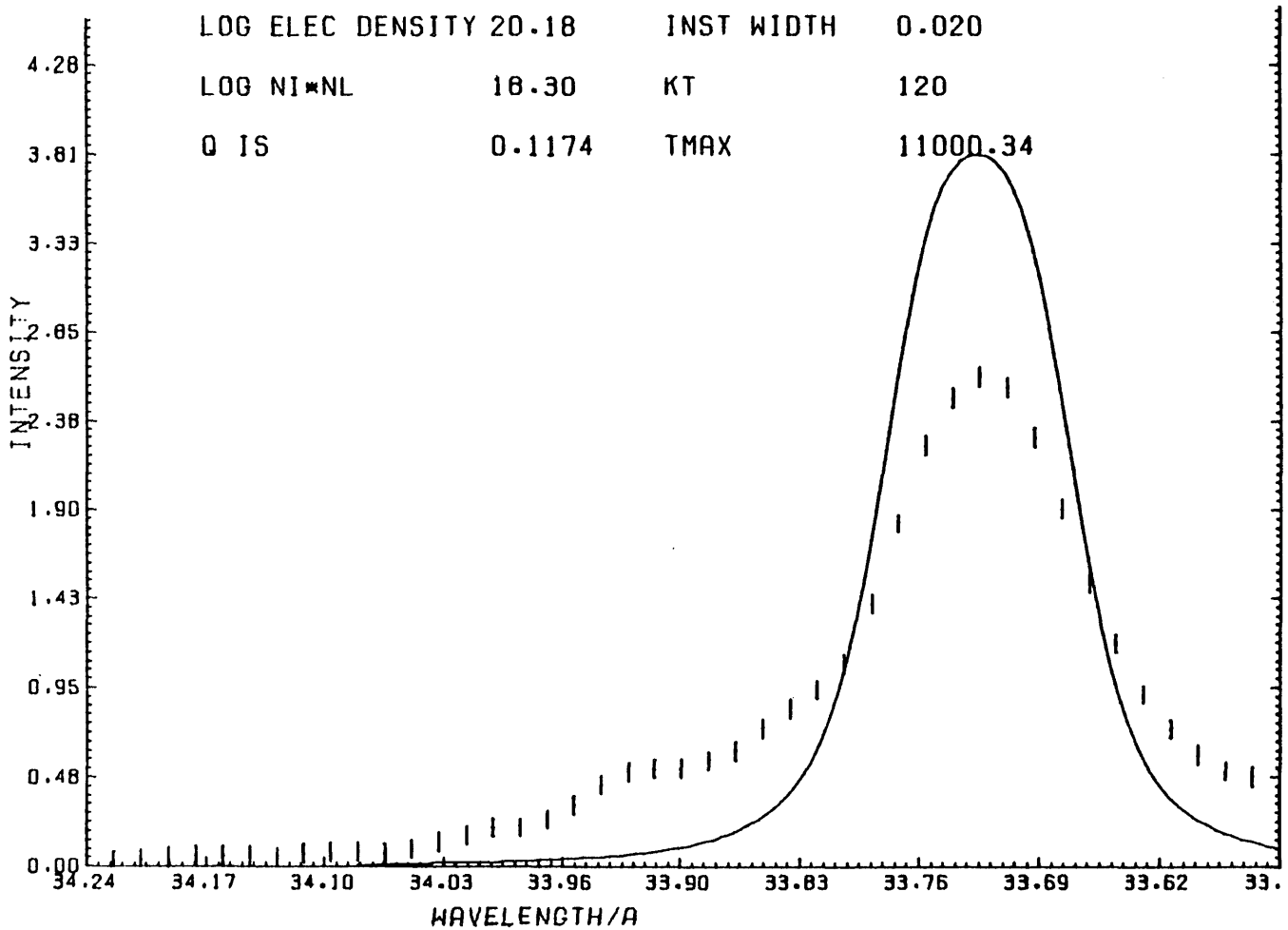


FIGURE 5.14 CARBON LYMAN LINE PROFILES FOR SPECTRUM IN FIGURE 5.1B Ly α



Q from equation 2.27 Tmax is peak opacity

Figure 5.14 Ly β

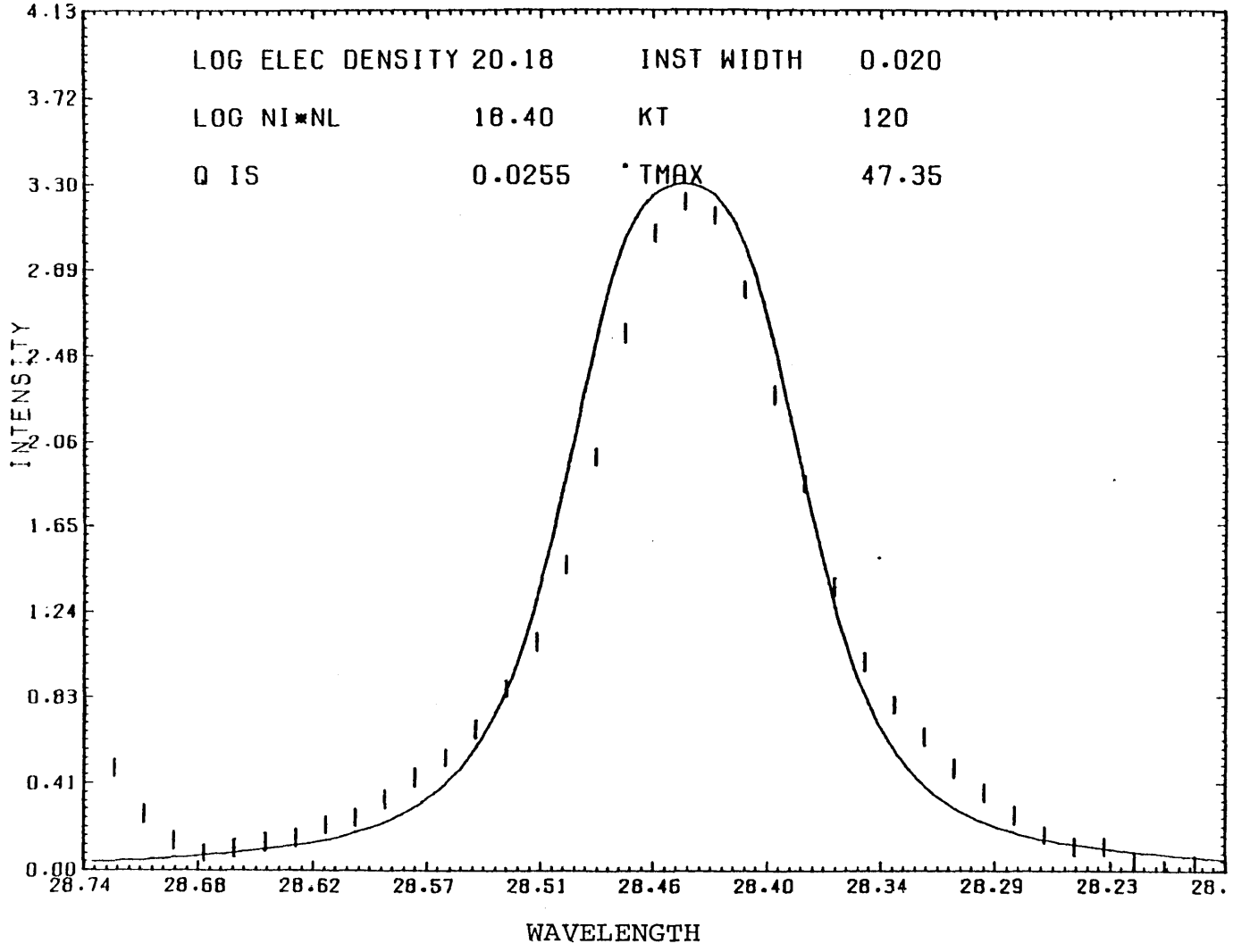


Figure 5.14 Ly γ

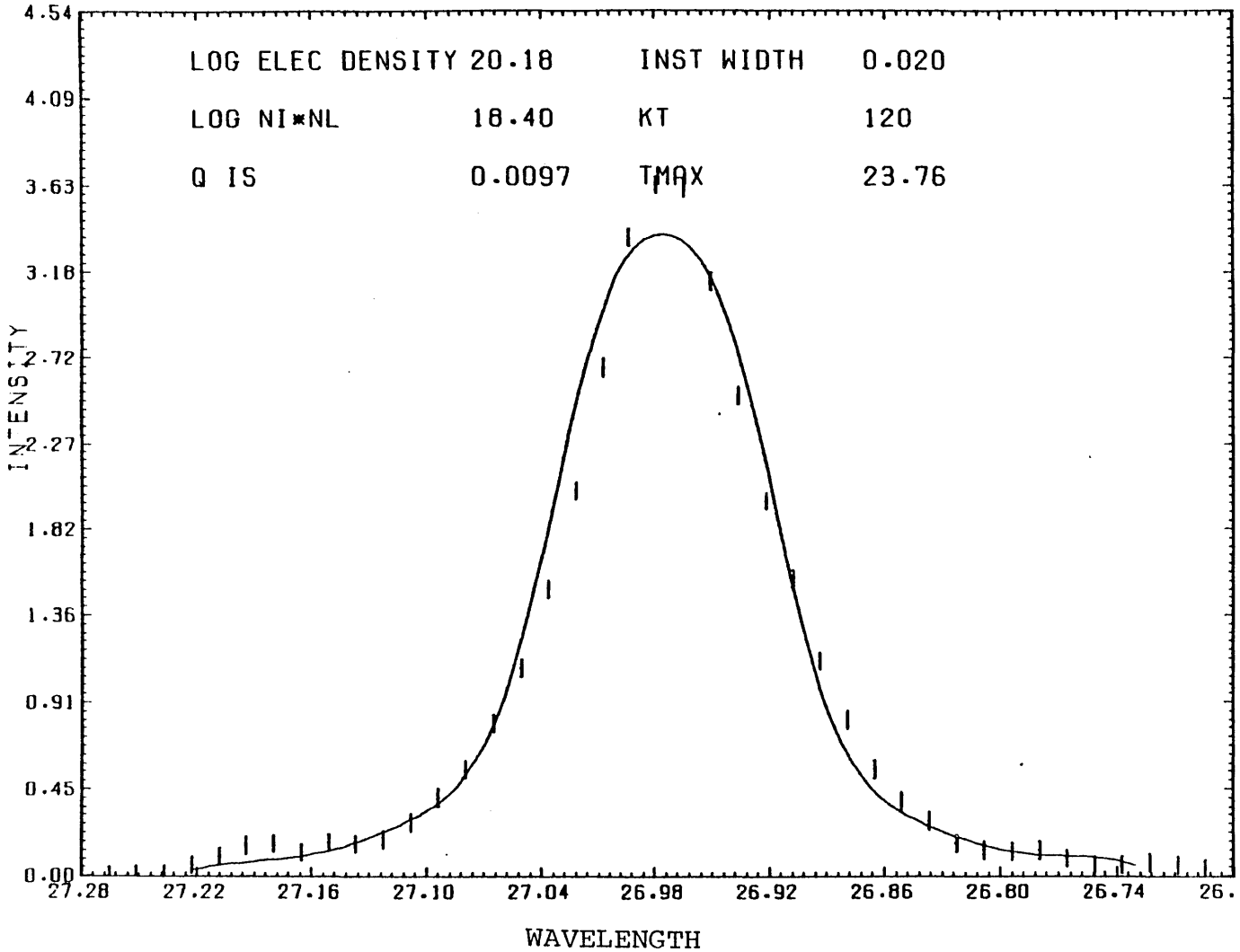


Figure 5.14 Ly δ

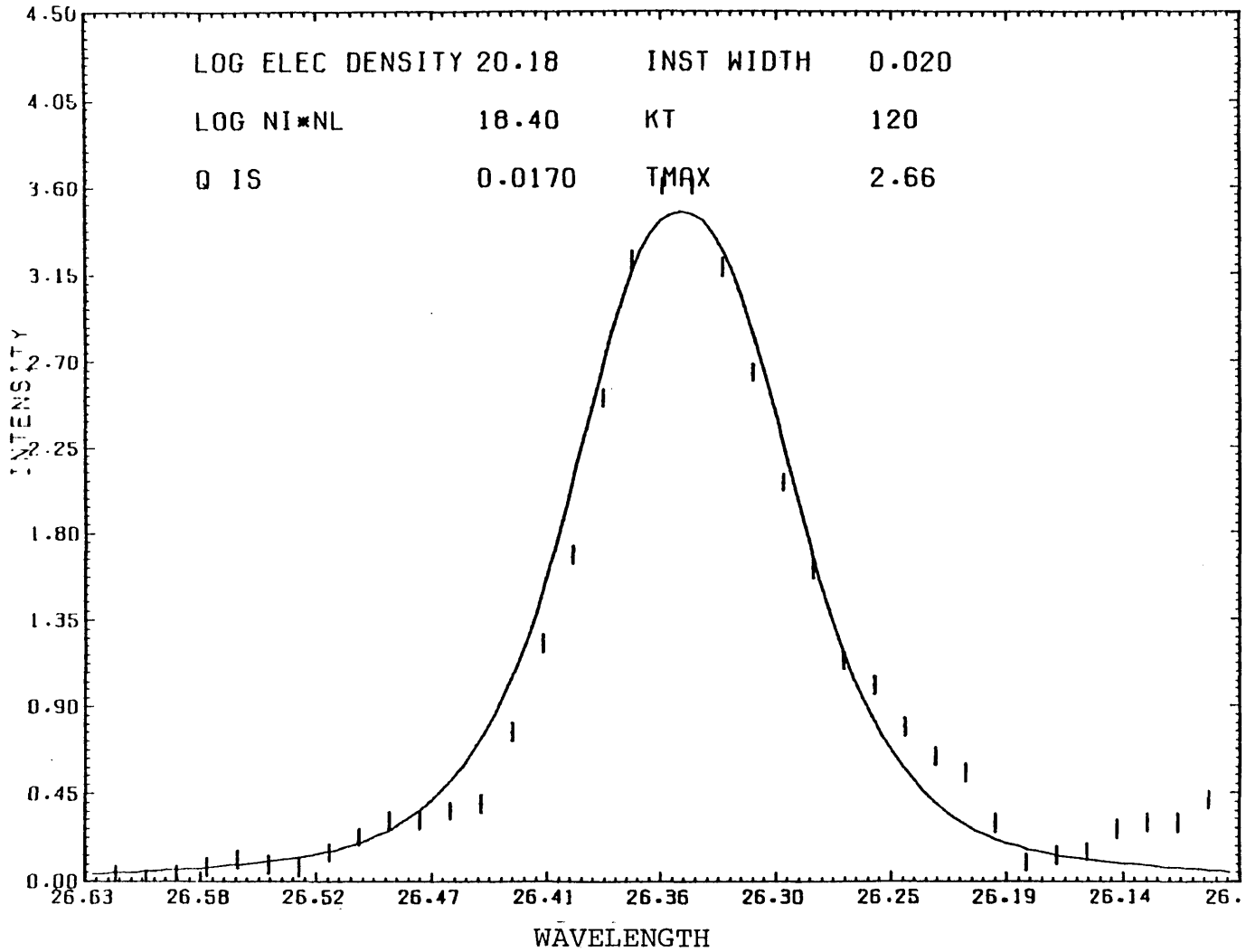


Figure 5.15 Carbon Lyman line profiles for spectrum in figure 5.1C Lyβ

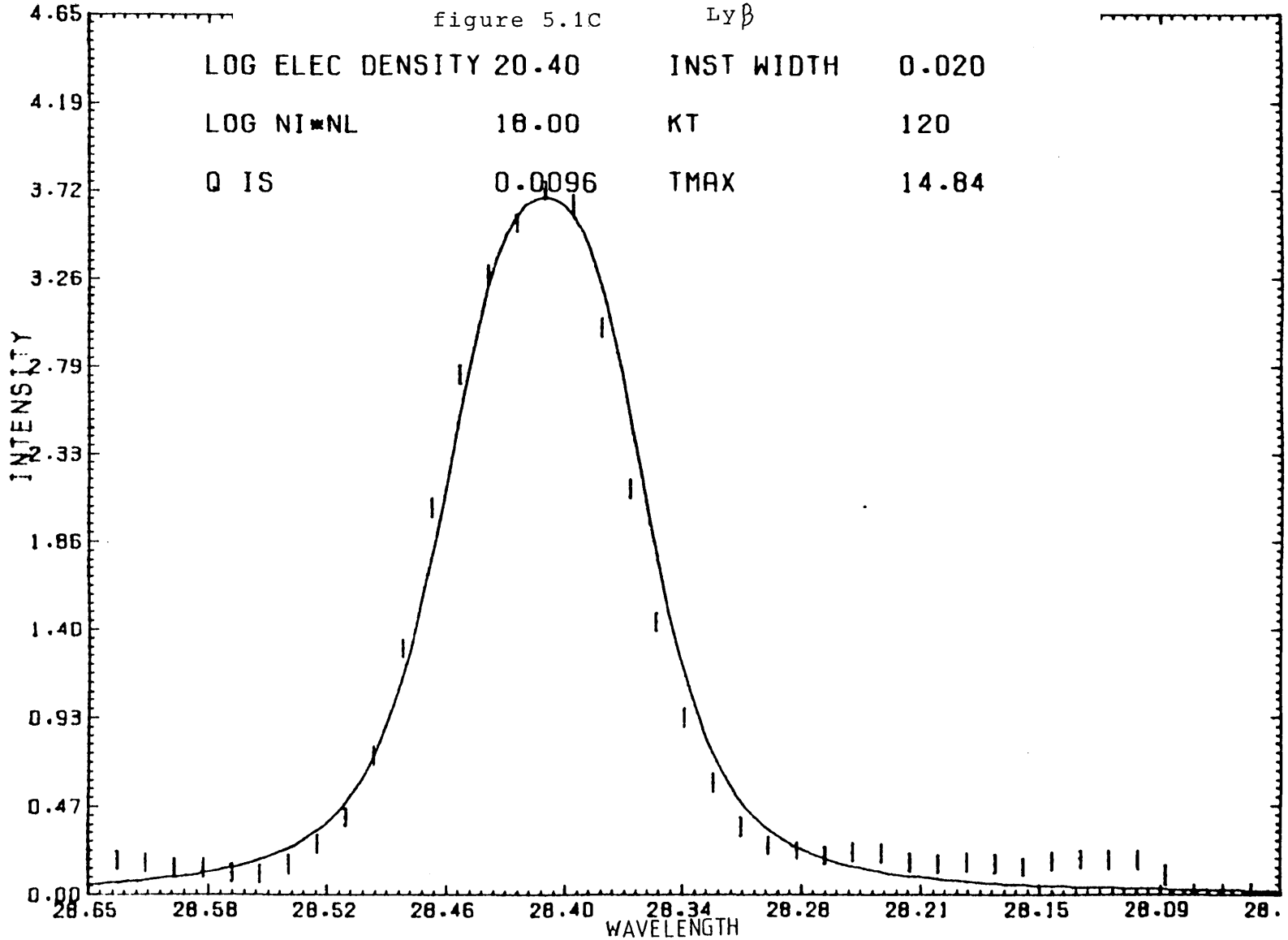


Figure 5.15 Ly γ

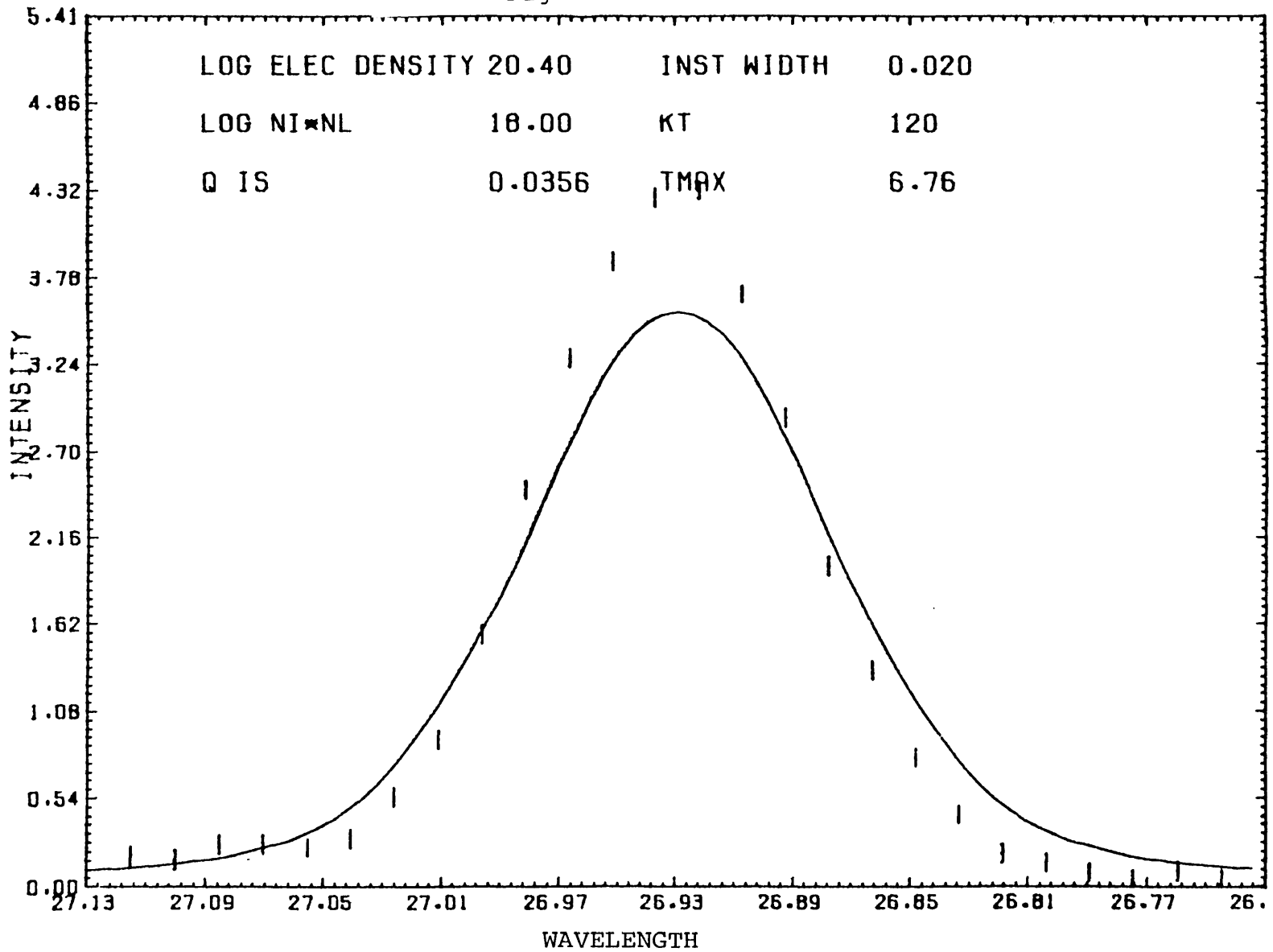


Figure 5.15 Ly δ

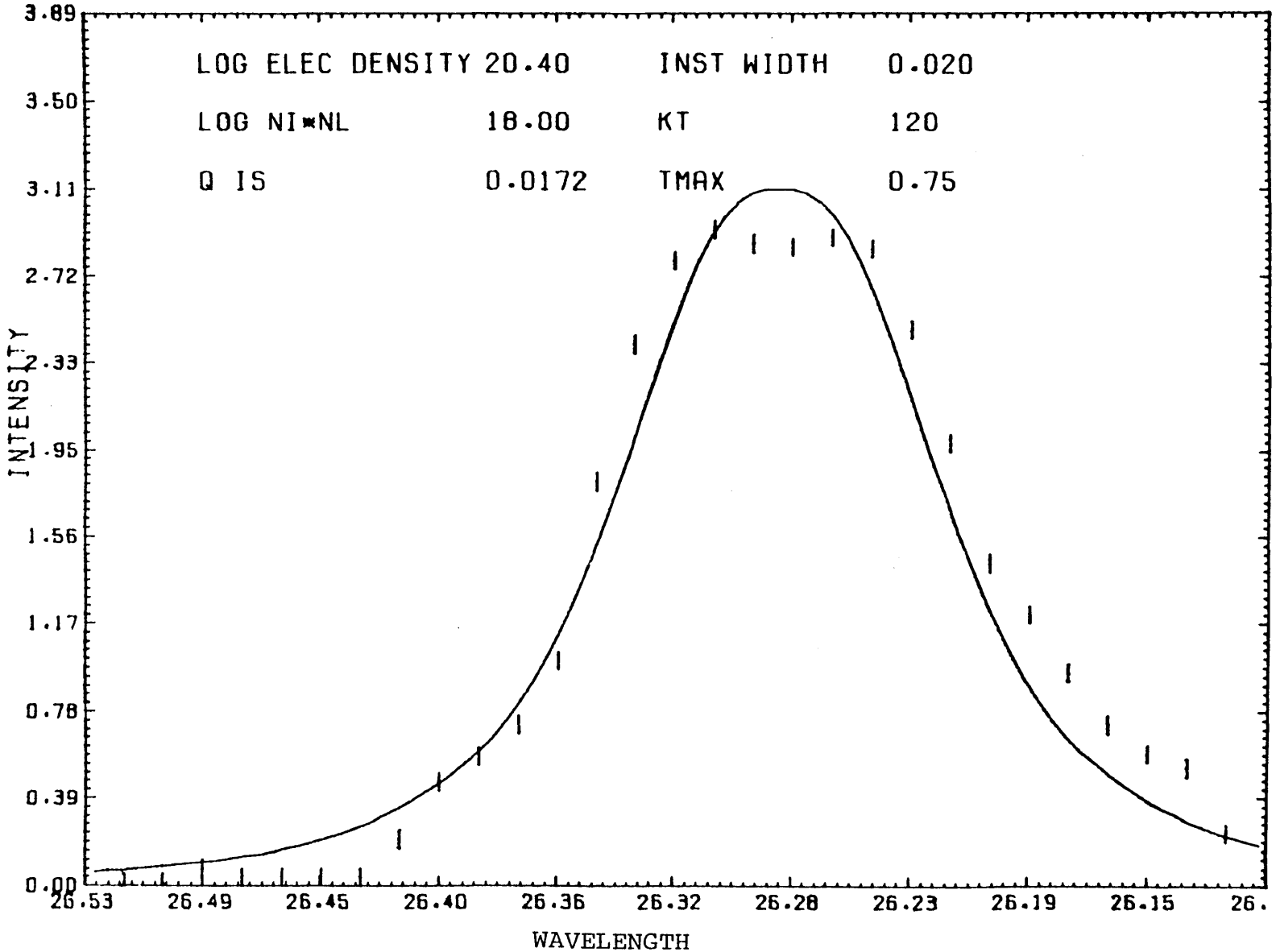


Figure 5.16 Fitting of Oxygen Lyman lines for Spectrum in figure 5.1B

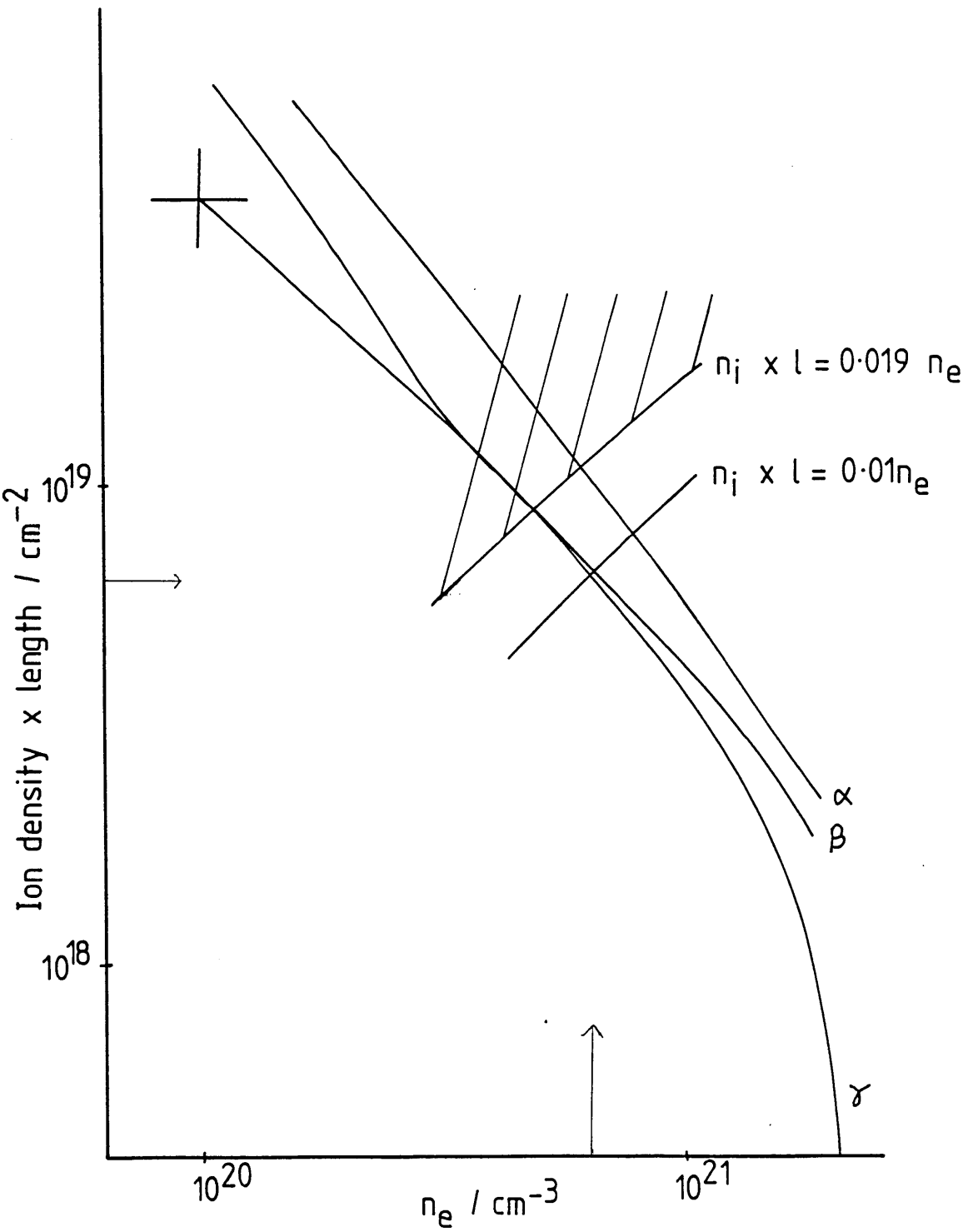


FIGURE 5.17 OXYGEN LYMAN LINE PROFILES IN FIGURE 5.1A

Lyα

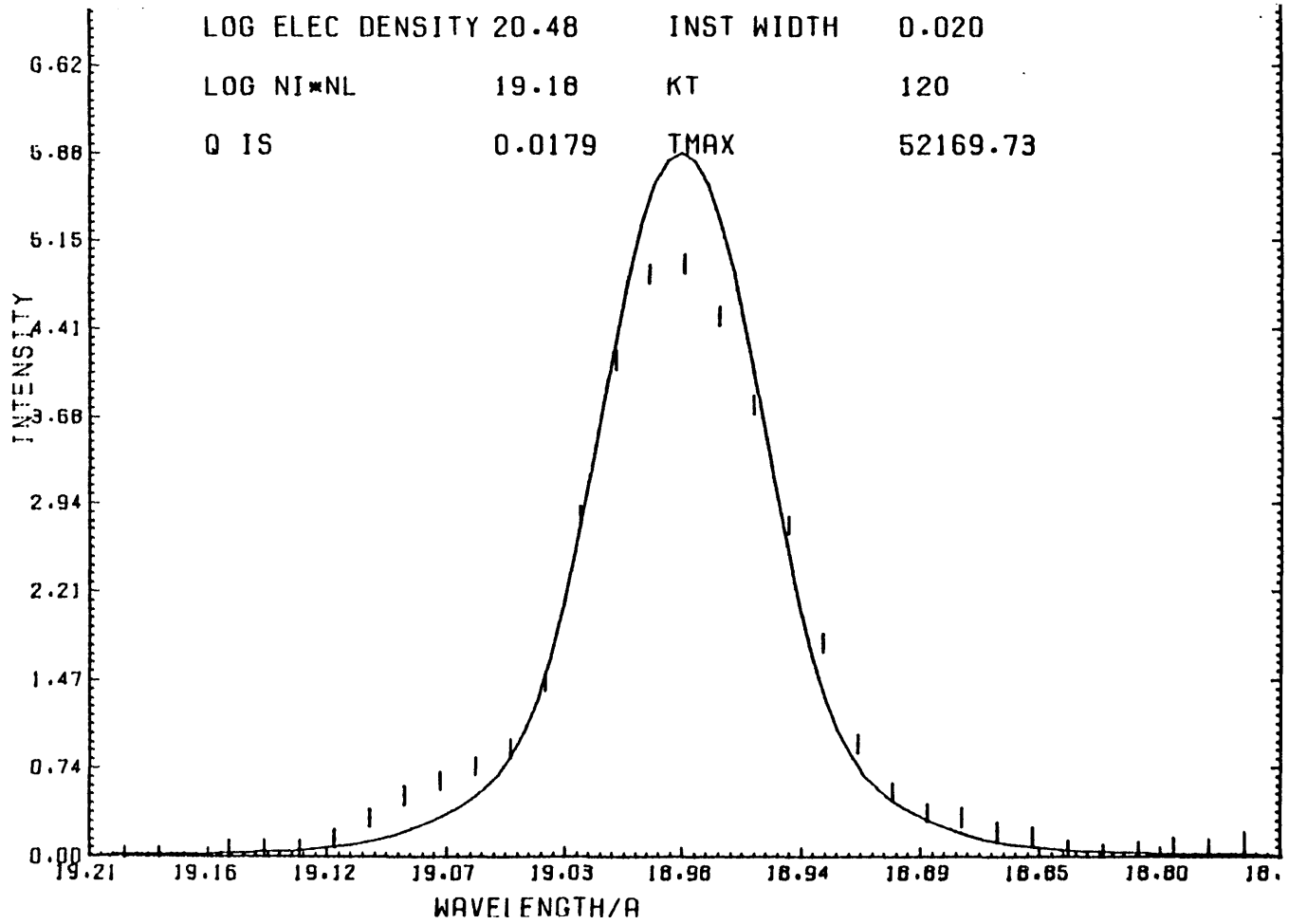


Figure 5.17 Ly β

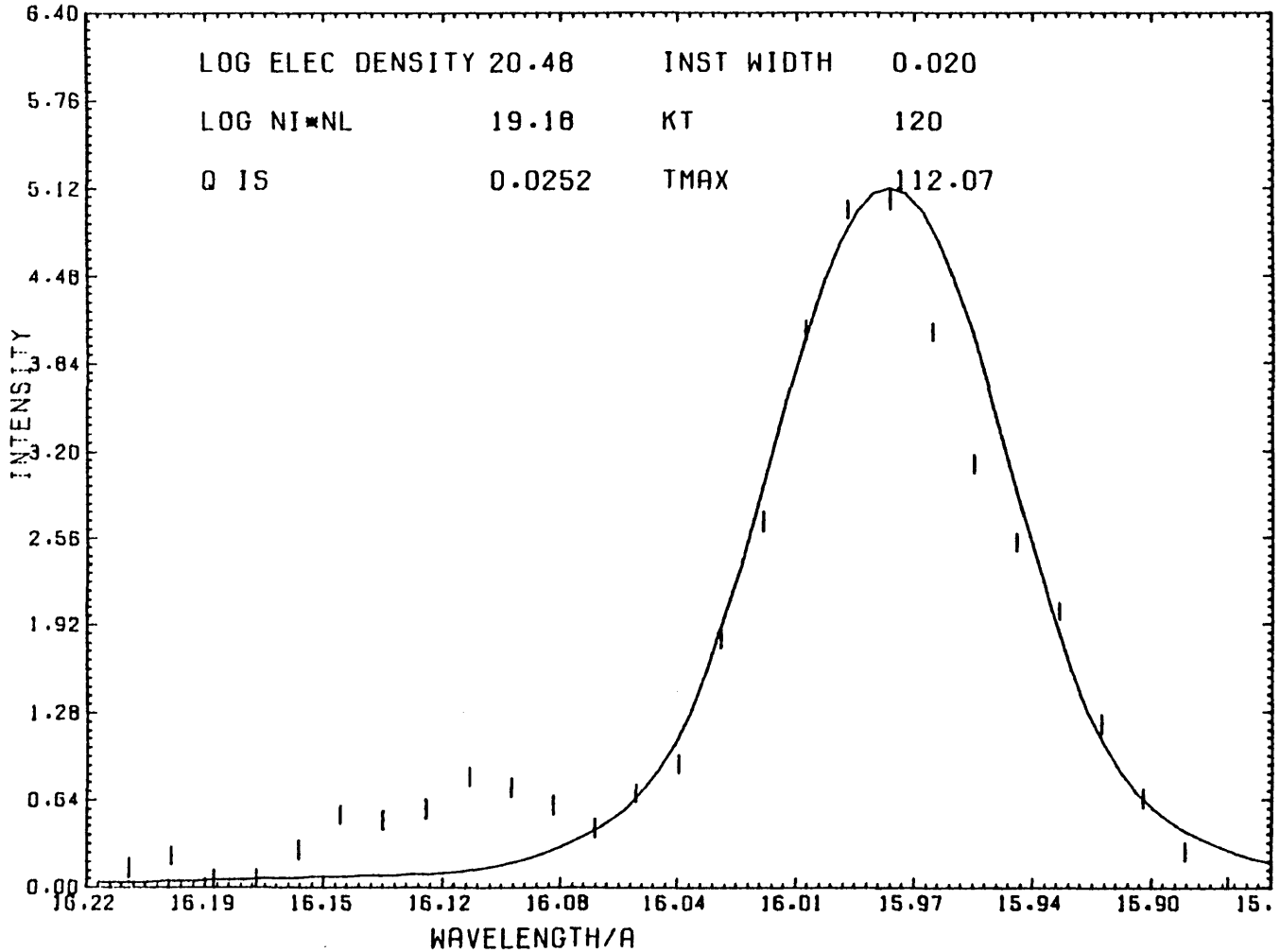
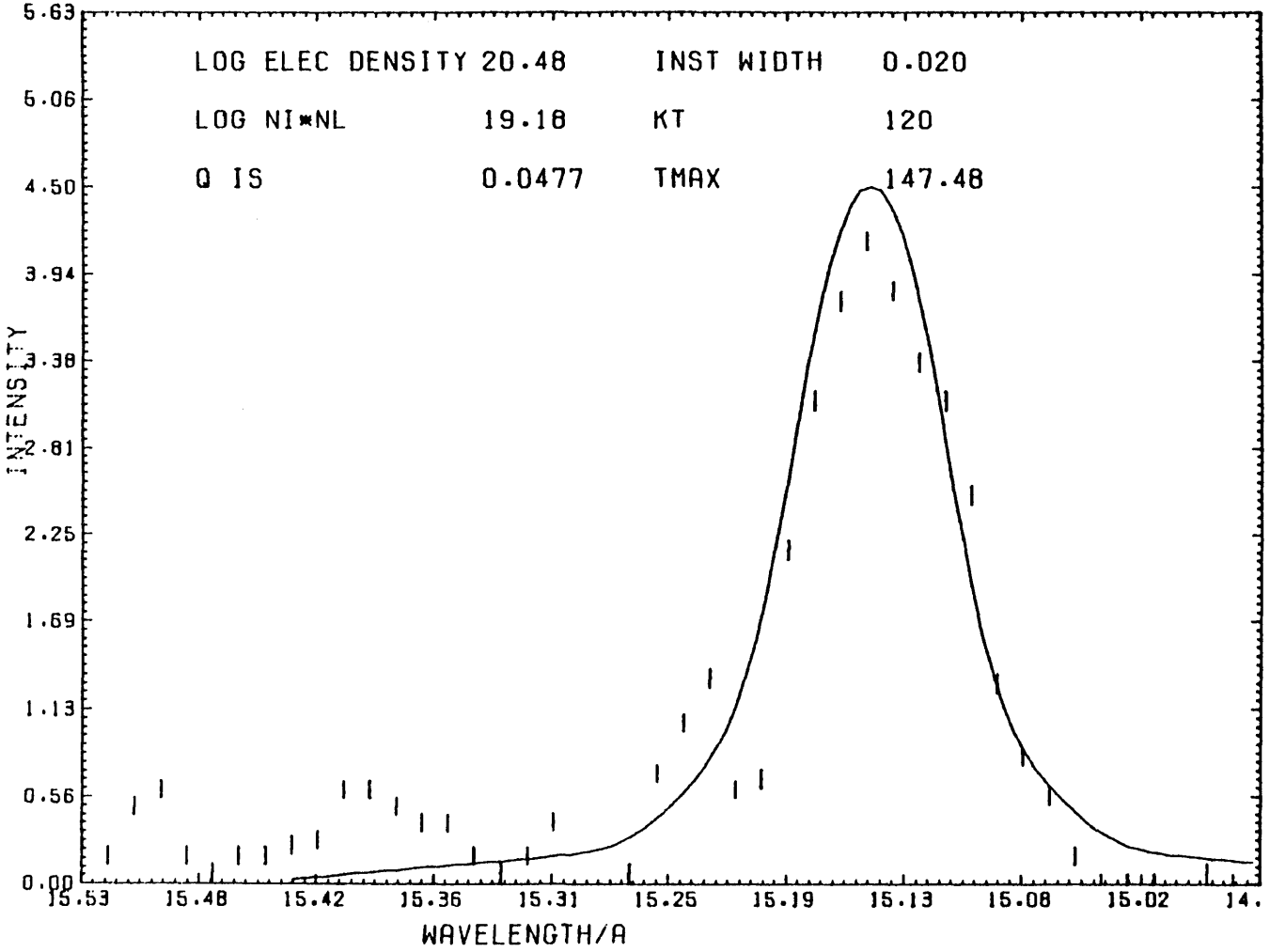


Figure 5.17 Lyγ



figures 5.16 and 5.17. Again the lines fit well, and in this case Lyα fits well despite the high opacity.

5.2.3 DISCUSSION

The results obtained using the above methods are summarized in table 5.5 for both of the plates in figure 5.1. The temperatures obtained using line ratios agree fairly well, but disagree with the temperatures obtained from the slope of the soft x-ray continuum. As mentioned in section 5.2.2, the intensity of the jkl satellite in carbon is much greater than would be expected, and implies a temperature of under 40eV. The wavelengths of the lithium-like satellites in carbon do not correspond well to those predicted, and the wavelength of the line previously identified as jkl in fact corresponds more closely to the forbidden $2^3S - 1\ ^1S$ transition. This forbidden transition is also highly sensitive to electron density, and would not be expected at densities over 10^{14} cm $^{-3}$. It may have been formed by a high temperature, low density background plasma within the gas-puff, but further observations would be needed to confirm this.

The electron densities obtained from dielectronic satellites and line broadening studies also agree well, with the exception of the helium-like satellites in carbon. Both Gabriel's and Vainstein and Safranova's wavelengths

Table 5.5 Summary of the results obtained in CO_2

Method	Quantity	Plate 74		Plate 75	
		Carbon	Oxygen	Carbon	Oxygen
Continuum slope	kT_e / eV	80±20	80±20	50±20	
$2p^2(^1D)$-1s2p np-1s	kT_e / eV	60±5	115±7	50±5	110±20
n-1 / 1snp-$1s^2$	n_B / n_H	1.3±.4	0.29±0.04	2.2±.6	0.5±0.1
$2p^2(^1D)$-1s2p	n_H / n_{He}	?	0.57±0.05		
Ionization	kT_e / eV	74±5	115±5	79	133
Lyα satellites	n_e / cm^{-3}	$(2.5\pm1)\times10^{20}$	$(6\pm4)\times10^{20}$		
Heα satllites	n_e / cm^{-3}	?	$(6\pm4)\times10^{20}$		
Line broadening	n_e / cm^{-3}	$(1.5\pm.5)\times10^{20}$	$(6\pm2)\times10^{20}$	$(2.5\pm.5)\times10^{20}$	
	$n_i x l$ / cm^{-2}	$(2.5\pm.5)\times10^{18}$	$(6\pm2)\times10^{18}$	$(1\pm0.4)\times10^{18}$	

and transition probabilities were used. The transition probabilities differed little from one another, but problems were found in fitting either of the values of wavelengths to the experimental spectra.

It can be concluded that the carbon and oxygen spectra are produced at different times and or different positions in the plasma. No evidence of non-thermal electron distributions has been seen, in contrast to the highly non-thermal electron temperatures implied by the hard x-ray emission from argon plasmas (Challis 1986). Hence the soft x-ray spectra appear to be a good diagnostic of the background plasma emission in the gas-puff for these low z plasmas.

Table 5.5 also summarizes the results obtained from the analysis of the spatially resolved spectrum obtained from a densitometer trace along the central mm of the spectrum. As this was a spatially resolved spectrum, the quality of the densitometer trace was much poorer, and hence some of the dimmer features were not visible above the noise. The electron density in oxygen was only obtainable from the satellites, which are shown in figure 5.8. The graph of N_e against N_i x 1 for carbon is shown in figure 5.13.

5.3 THE EFFECT OF PRE-IONIZATION

The plates taken without pre-ionizing the injected gas are generally poor, with few of the weaker satellites and

continua visible. The effect of pre-ionization is to make the collapse of the plasma more uniform and possibly with a higher velocity. Hence more of the collapse energy is thermalized on axis, and thus the emission is thermal, and in the soft x-ray region, rather than non-thermal with a large hard x-ray component.

Figures 5.18 and 5.19 show the photo and densitometer trace of a spectrum of carbon dioxide without pre-ionizing the gas. The slope of the soft x-ray continuum is shown in figure 5.20. The absence of Stark broadening in the spectrum indicates that the electron density is less than 3×10^{19} cm^{-3}. Analysis of the lithium-like satellites in oxygen indicates an electron density of 10^{20} cm^{-3}

Table 5.6 Summary of results from CO_2 without pre-ionization

Method	Quantity	Plasma	Result
Continuum slope	kT_e / eV	C	70±30eV
$1snp-1s^2/n-1$	kT_e	C	65±5 eV
		O	160±5 eV
Heα satellites	n_e	O	$(3\pm1)\times10^{19}cm^{-3}$
line broadening	n_e max	C	$3\times10^{19}cm^{-3}$

Figure 5·18 Carbon dioxide spectrum

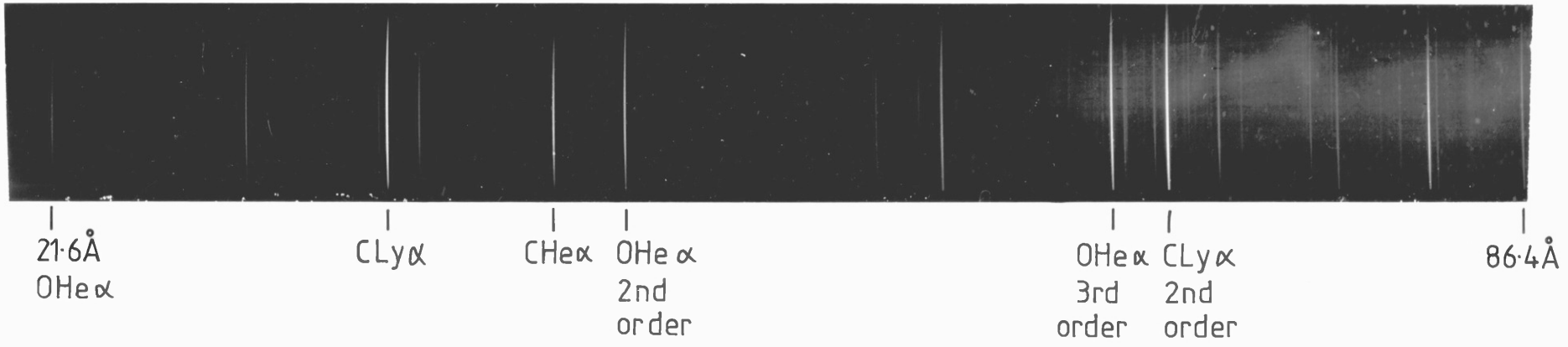
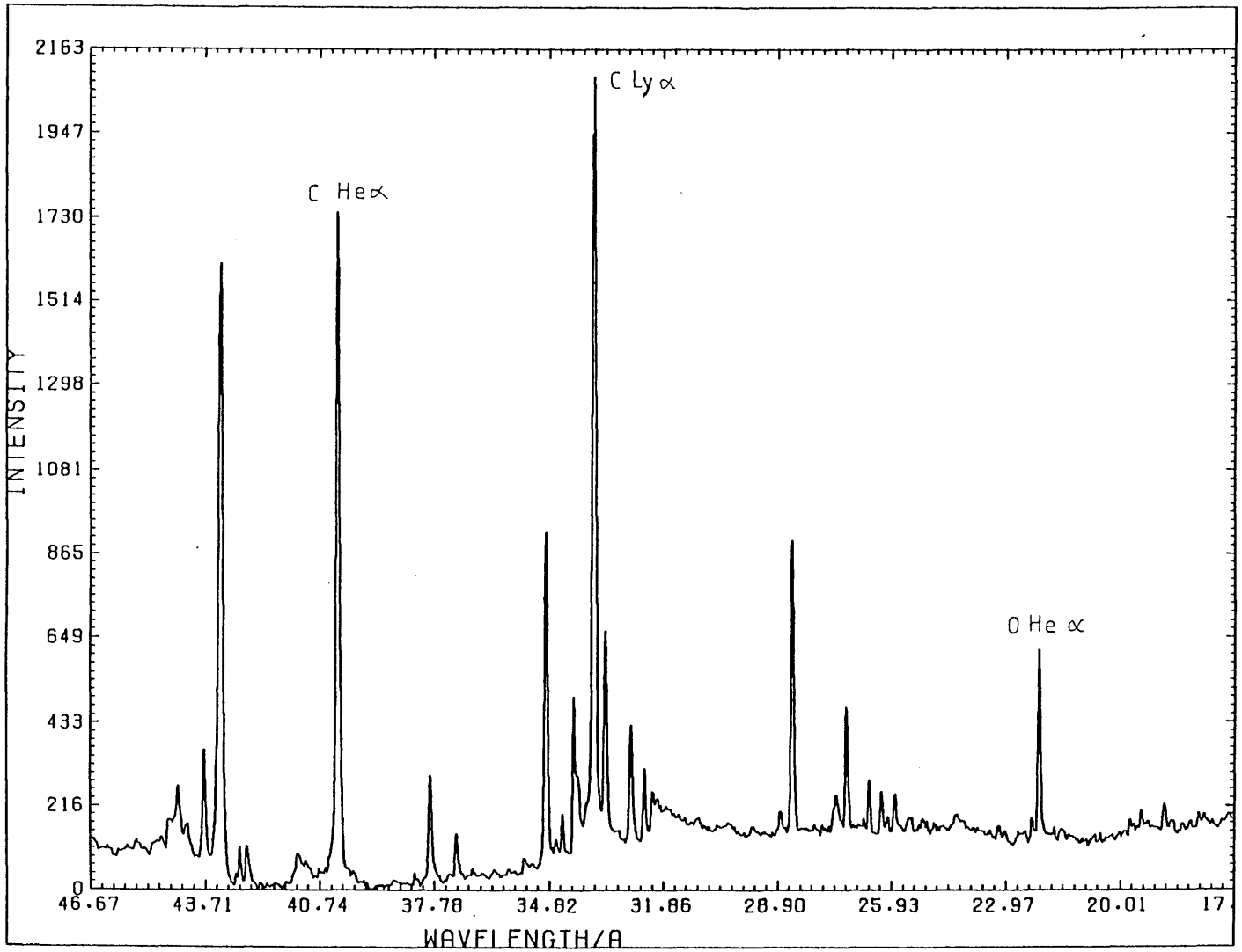


FIGURE 5.19 DENSITOMETER TRACE OF CARBON DIOXIDE SPECTRUM TAKEN WITHOUT PRE-IONIZATION



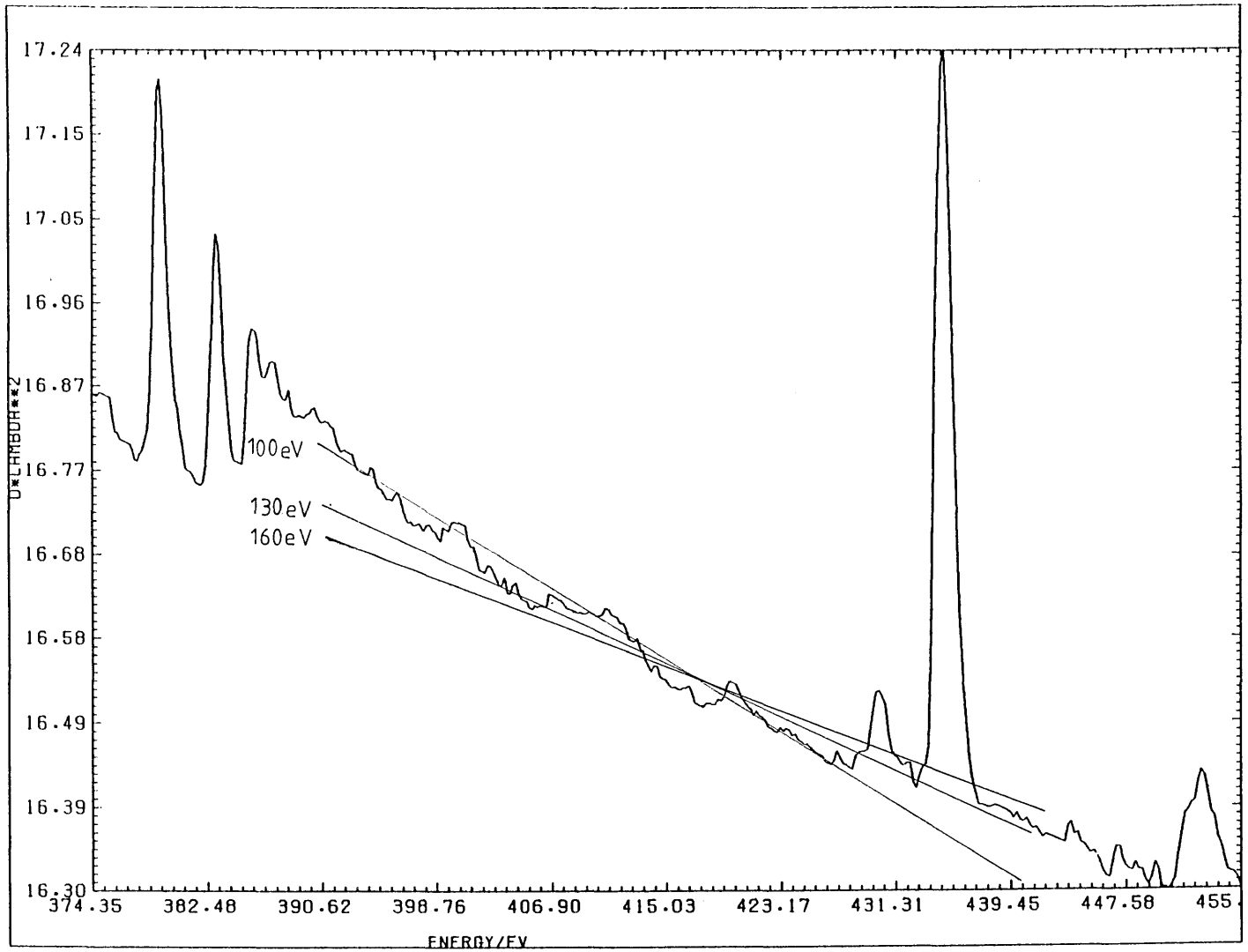


FIGURE 5.20 SLOPE OF THE SOFT X-RAY CONTINUUM FOR SPECTRUM IN FIGURE 5.18

One of the reasons why the results obtained from this plate are not consistent was that it was found necessary to superimpose several shots (in this case 6) in order to obtain a sufficiently exposed spectrum. The poor results serve to indicate the irreproducibility of the soft x-ray radiation from the gas-puff without pre-ionization, in contrast to the hard x-ray output which is much more reproducible without pre-ionization (Challis 1986).

5.4 RESULTS OBTAINED IN OTHER GASES

In addition to spectra of carbon dioxide, spectra of nitrogen and neon have been obtained. The spectra of nitrogen were taken without pre-ionization, and are thus poor. The spectra of neon however, were taken with pre-ionization. This section will present and analyse these spectra.

Figure 5.21 shows photographs of two neon spectra, with a densitometer trace in figure 5.22. Experimental conditions for the plates are given in table 5.2. Densitometer traces across the dominant lines of each ion species in the radially resolved spectrum are presented in figure 5.23. They show that the Ne VII and Ne VIII lines come from a slightly larger region of plasma of diameter 1.8mm. The Ne IX lines come from a region of diameter 1.4mm.

The electron temperature for this spectrum can be found

from the slope of the soft x-ray continuum, and also from line intensity ratios of Ne VII, VIII, IX and X ions. The electron density however, can only be obtained from the lithium-like satellites, because the helium-like satellites are not visible, and there is no evidence of Stark broadening.

Table 5-7 Wavelengths and intensities observed in Ne

Wavelength /Å	Intensity /J	Ion	Transition
11.00	0.043	IX	$1s4p-1s^2$
11.54	0.077	IX	$1s3p-1s^2$
12.13	0.096	X	2-1
13.45	0.27	IX	$1s2p(^1P)-1s^2$
13.54	0.046	IX	$1s2p(^3P)-1s^2$
13.71	0.011	VIII	$1s2s^2-1s^22s$
14.16	0.036	VIII	$1s^22p-1s2s^2$
56.04	0.025	VIII	7p-2s
57.75	0.023	VIII	6p-2s
60.80	0.081	VIII	5p-2s
62.36	0.10	VIII	6d-2p
65.80	0.047	VIII	5d-2p
65.10	0.058	VIII	5d-2p
67.38	0.133	VIII	4p-2s
68.78	0.013	VII	2p5p-2s2p
68.92	0.016	VII	2s7d-2s2p
70.99	0.091	VII	2s6d-2s2p

Figure 5·21 Neon Spectra

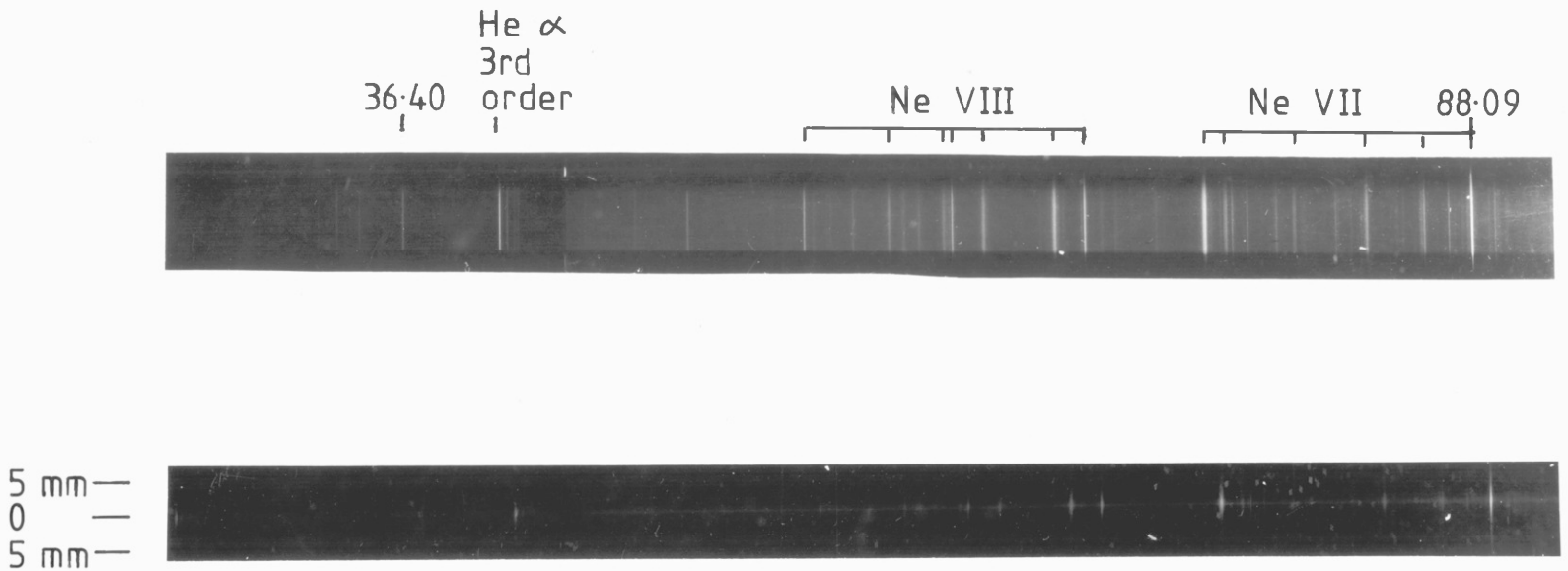


FIGURE 5.22 DENSITOMETER TRACE OF NEON SPECTRA

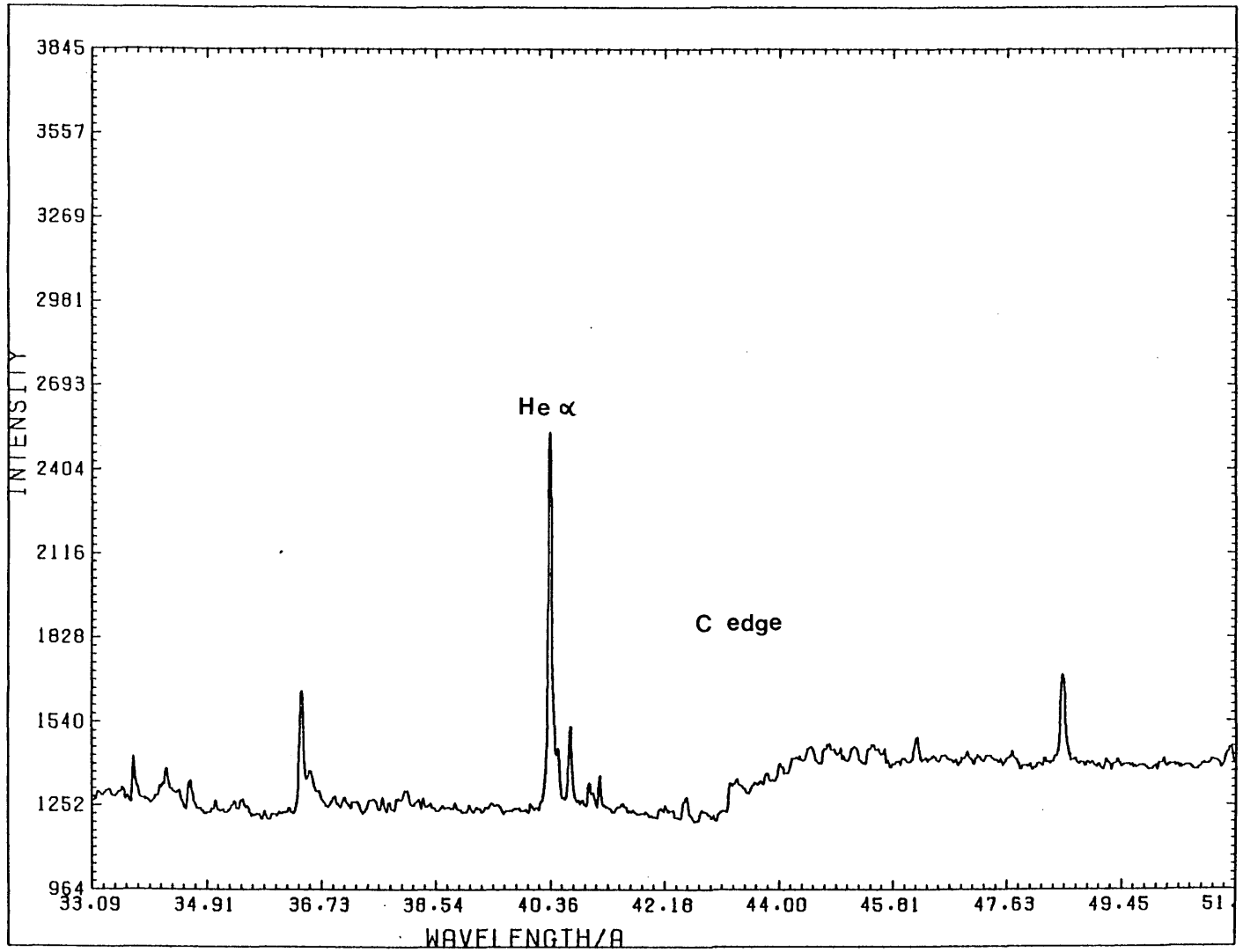


Figure 5.22 continued

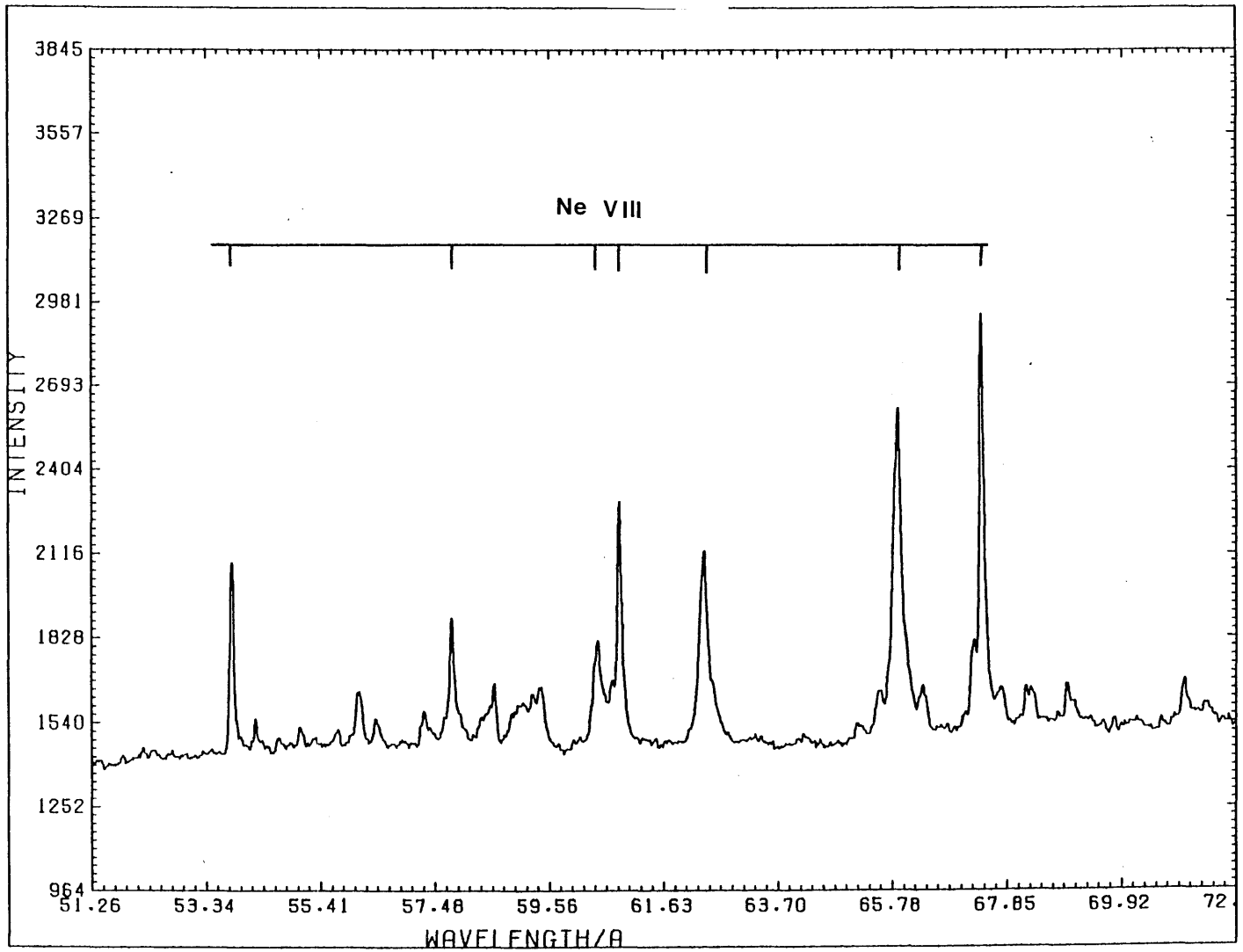
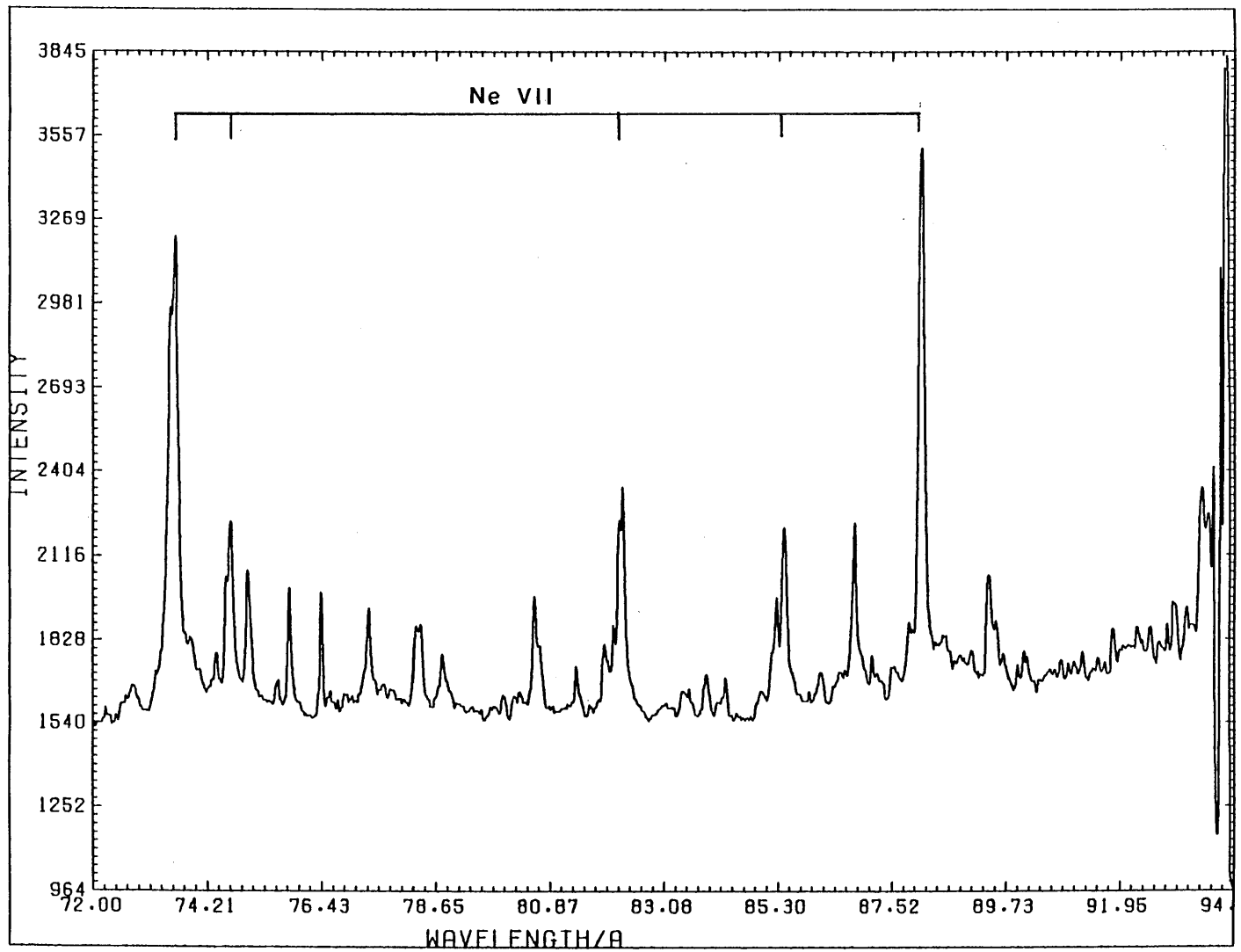


Figure 5.22 continued



Wavelength /Å	Intensity /J	Ion	Transition
73.47	0.156	VIII	4d-2p
73.57	0.198	VIII	4d-2p
74.23	0.016	VII	2s7d-2s2p
74.96	0.031	VII	2p4p-2s2p
75.77	0.025	VII	$2s4p-2s^2$
77.30	0.038	VII	$2p5d-2p^2$
80.53	0.022	VII	2s5d-2s2p
81.37	0.012	VII	2p4p-2s2p
82.20	0.045	VII	2s4d-2s2p
82.27	0.073	VII	2s4d-2s2p
85.19	0.02	VII	$2p4d-2p^2$
85.29	0.004	VII	$2p4d-2p^2$
85.43	0.067	VII	$2p4d-2p^2$
86.82	0.036	VII	$2p4d-2p^2$
88.09	0.31	VIII	3p-2s
89.02	0.023	VII	$2p4s-2p^2$

In addition to the methods described in section 5.2, a new line ratio was used to obtain the electron temperature in neon discharges. In the carbon dioxide and nitrogen spectra, the only lithium-like lines visible were the satellites. In the neon spectra however, lithium-like resonance lines were seen, and hence equation 2.19 was applied to the line ratios :

$$\underline{\underline{1s^2}}\,\underline{\underline{5p}}\;(jkl) - \underline{\underline{1s^2}}\,\underline{\underline{2s}} \qquad\qquad \underline{\underline{1s^2}}\,\underline{\underline{5d}}\;(jkl) - \underline{\underline{1s^2}}\,\underline{\underline{2s}}$$

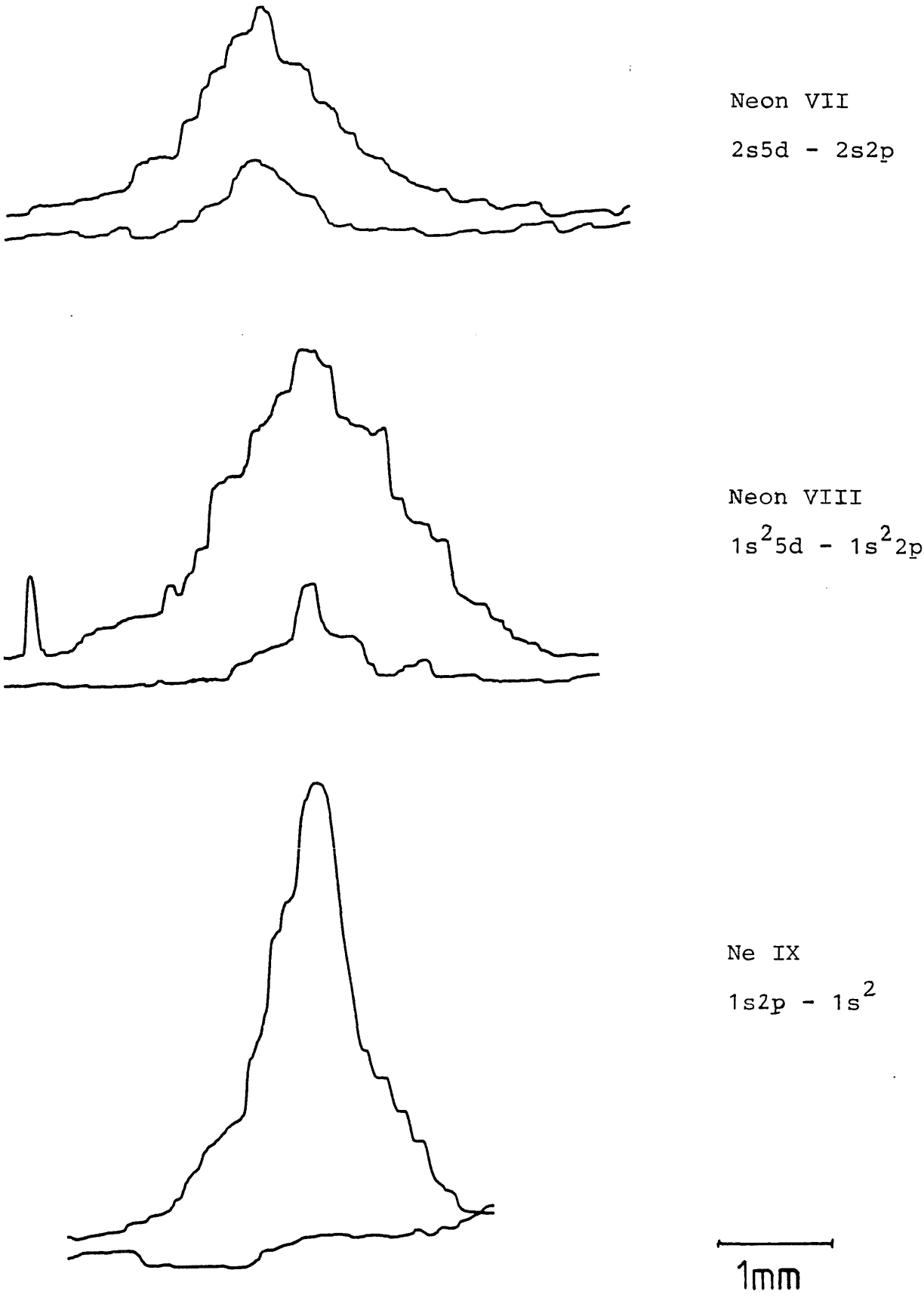
The lines used for the calculation of the electron temperature are listed in table 5.3 .

The results are tabulated in table 5.8. They indicate an electron temperature of 90eV with a slightly lower temperature obtained from the slope of the continuum. The electron density implied by the satellites is $2\pm1\times10^{21}$ cm^{-3}. The results agree well with one another, with the exception of the Heα/Lyα line ratio, which indicates a higher temperature of 200eV. This is probably due to the Lyα line being optically thick. The results are also quite similar to those obtained from the oxygen spectrum in carbon dioxide.

Table 5.8 Summary of results in Neon

Method	Quantity	Result
Continuum slope	kT_e / eV	65±20
jkl / $1s3p-1s^2$	kT_e / eV	100±10
jkl / $1s^2 2s-1s^2 4p$	kT_e / eV	80±10
$1s3p-1s^2$ / 2-1	kT_e	200
Heα satellites	n_e / cm^{-3}	$(2\pm1)\times10^{21}$

FIGURE 5.23 RADIAL DENSITOMETER TRACE ACROSS MAJOR LINES IN NEON SPECTRUM



CHAPTER 6 CONCLUSIONS

6.1 SUMMARY OF RESULTS

This work has greatly extended the study of the soft x-ray spectrum of a gas-puff z-pinch, in terms of the wavelength resolution achieved, the plasmas observed, and the range of firing conditions used. A much better understanding of the factors affecting soft x-ray production in a gas-puff z-pinch has thus been obtained, and is summarized in the following points:

1 The argon spectrum of a gas-puff z-pinch has been observed with a higher resolution than before, at a greater range of firing conditions. This has been used to obtain both electron temperatures, and electron densities for the thermal, background plasma in the device, which can only be observed by means of soft x-rays; the harder x-rays being produced mainly from non-thermal instabilities in the device, such as hot-spots.

2. A high resolution Ar XV spectrum has been observed for the first time, and the wavelengths and intensities have been shown to agree well with published theories.

3. Carbon dioxide and neon spectra have been analysed in detail to obtain electron and ion densities, electron

temperatures, and ion density x length products. The results from the different methods agree well, but the results from carbon and oxygen in a carbon dioxide discharge differ, suggesting that the plasmas were formed in different times or places.

4. An unidentified satellite of the $2^1P - 1\ ^1S$ line of carbon has been observed. The wavelengths of this line corresponds to the wavelength of the forbidden $2^3S - 1^1S$ line. This line would not be expected at electron densities above 10^{14} cm^{-3}. Recent evidence from filtered pinhole photographs suggests the existence of a high temperature (10keV), low density background plasma (C. Deeney, private communication), which may give rise to this feature.

5. The effects of pre-ionization, the nozzle size, and the charging voltage have been studied. The most significant of these features is pre-ionization, which gives a higher temperature, higher density plasma, which emits a larger quantity of soft x-rays. The absence of hard x-rays under these conditions suggests that the collapse is more even, giving a more uniform plasma. The spectra taken without pre-ionization were all poor, and several shots needed to be superimposed for a sufficiently exposed spectrum. A higher charging voltage of 30kV gave a much higher temperature plasma, with a strong Ar XV spectrum.

6.2 SUGGESTIONS FOR FURTHER WORK

It is clear from the work in this thesis that further studies of the soft x-ray spectrum from the gas-puff z-pinch are best conducted with pre-icnization, which gives a much brighter spectrum. Further studies of pre-ionized discharges would be useful in gaining a better idea of how the plasma parameters are affected by charging voltage and the plenum pressure. The previously obtained spectra of nitrogen were poor, as none of them were obtained with pre-ionization. These spectra could be repeated with pre-ionization, and the studies extended to other gases.

The resolution of the Ar XV spectrum obtained could be improved in several ways. At the time that the spectra were taken, a full study of the focus of the spectrograph had not been completed, and thus the resolution shcuild be improved by repeating the spectrum with the focused spectrograph, giving a theoretical resolution of 14mA. This could be improved still further by using a 6001/mm grating instead of the 3001/mm grating used in this study. The wavelength calibration of the spectrograph could also be improved by finding a better set of standards than the Ar IX and X lines used. Although the spectrum of H-like carbon is often used, the electron density of the plasma would need to be lowered to ensure that the Stark broaden-

ing would be less than the instrumental width. This could possibly be achieved with a mixture of carbon and argon.

The line broadening studies conducted can now also be extended to include the helium-like lines of carbon and oxygen using the theoretical profiles of Lee (Kilkenny et al, 1980), which should soon be available at Imperial College. The Lyman line profiles can also be compared to those of Griem used in this thesis to obtain the best fit to the experimental spectrum.

Finally, the experimental techniques developed in this thesis could be invaluable in a future investigation of x-ray laser schemes on the gas-puff z-pinch. The time-resolved detector that has been developed for the spectrograph (Mrowka, 1983) would be invaluable in investigating the proposed lasing lines of several of the schemes currently under investigation.

APPENDIX

The following programs were used in this thesis :

SCALE77 This takes the data file transmitted from the TANDY, displays it, and requests the wavelengths of known lines.

TRY This fits a Chebyshev polynomial to the data and indicates the success or otherwise of the fit on the file TAPE7. TAPE10 lists the coefficients of the polynomial.

CALCAR This uses TAPE10 in order to calibrate the original spectrum TAPE1. The output is to the file CALDATA.

DISPLAY This displays any selected portion of the spectrum. A modified version calibrates the intensity, displaying the energy per 40mA.

LINEFIT This calculates a theoretical satellite spectrum using Lee's collisional-radiative code and wavelengths and A-values from Vainstein and Safranova.

CONTHK This opacity broadens theoretical Stark profiles of Griem, convolves them with the instrumental profile, and fits them to the experimental spectrum.

```
C    SCALE77 READS FILE FROM TANDY. USER INPUTS WAVELENGTHS OF KNOWN
C    LINES USING CURSOR TO GIVE POSITIONS. WAVELENGTH OF 0.0 TERMINATES
C    AND NEXT RANGE CAN BE DISPLAYED. OUTPUTS DATA TO FILE DATA19
C    WHICH IS USED AS INPUT FOR PROGRAM TRY.
      PROGRAM SCALE77(INPUT,OUTPUT,DATA19,TAPE5=INPUT,TAPE1,
     1 TAPE3=DATA19,TAPE6=OUTPUT)
      DIMENSION IXEXP(10000),IYEXP(10000)
      CHARACTER*1 C,NCHAR
      CHARACTER*77 IDENT
C    READ IN IDENSTIFICATION, WRITE OUT PARAMETERS FOR POLYNOMIAL.
      READ(1,100) IDENT
      WRITE(3,100) IDENT
  100 FORMAT(A)
      WRITE(3,150)
  150 FORMAT(3X,'0.0000',4X,'0303 10',4X,'521120002000',
     2 10X,'000000 ',8X,'0.00 003455404',/,'999999999')
      READ(1,*)M,L,J,K
      IF(L.GT.M) J=K
      IF(L.GT.M) M=L
C    READ IN DATA
      READ(1,*)(IYEXP(I),I=1,M)
C     IBACK IS LOWEST VALUE OF THE DENSITY MEASURED. IE BACKGROUND.
      READ(1,*) IBACK
        DO 200 I=1,M
          IXEXP(I)=I*J
          IYEXP(I)=IYEXP(I)-IBACK
  200     CONTINUE
      CALL START(2)
C    SPECTRM PLOTS OUT THE SPECTRUM.
  300     CALL SPECTRM(XL,TICKS,YMAX,IXEXP,IYEXP,J)
  400         CONTINUE
C    IDENTIFY THE POSITION OF A LINE USING THE CROSS-WIRES
C    INPUT THE WAVELENGTH XLAMBDA.
              CALL XWIRES(XPAGE,YPAGE)
              XSPC=XPAGE*TICKS/2.05+XL
              YSPC=YPAGE*YMAX/1.5
```

```
              READ (5,*,END=400) XLAMBDA
              IYSPC=IFIX(YSPC)
              IF(XLAMBDA.EQ.0.0) GOTO 470
              IF(XLAMBDA.EQ.99.0) GOTO 400
C     WRITE OUT INFORMATION TO FILE DATA19
              WRITE(3,450)XSPC/100.,XLAMBDA,IYSPC
  450         FORMAT(F7.2,F8.2,2X,I4)
              GOTO 400
  470     WRITE(6,*)'REPEAT'
          READ(5,500,END=470) C
  500     FORMAT(A1)
          IF(C.NE.'N')GOTO 300
        WRITE(3,550) '999999999'
  550   FORMAT(A)
C    FIND POSITIONS OF UNKNOWN LINES USING THE CROSS-WIRES
  580     CALL SPECTRM(XL,TICKS,YMAX,IXEXP,IYEXP,J)
  600     CONTINUE
          CALL XWIRES(XPAGE,YPAGE)
          XSPC=XPAGE*TICKS/2.05+XL
          IYSPC=IFIX(YPAGE*YMAX/1.5)
          WRITE(3,700)XSPC/100.,IYSPC
  700     FORMAT(F7.2,2X,I4)
  750     READ(5,500,END=750) NCHAR
C     NCHAR=R MEANS NEW FRAME, NCHAR=S MEANS STOP.
          IF(NCHAR.EQ.'R') GOTO 580
          IF(NCHAR.NE.'S') GOTO 600
        WRITE(3,550) '999999999'
        CALL ENPLOT
        STOP
        END
C    SPECTRUM PLOTS OUT THE SPECTRUM OVER REQUESTED RANGE, L,K.
          SUBROUTINE SPECTRM(XL,TICKS,YMAX,IXEXP,IYEXP,J)
          DIMENSION IXEXP(10000),YEXP(10000),XEXP(10000),IYEXP(10000)
          CALL PROMPT('INPUT 1ST AND LAST POINTS FOR PLOTTING')
          READ(5,*)L,K
          TICKS=FLOAT(K-L)*J/10
```

```
      XL=FLOAT(L)*J
      NUM=K-L+1
C     READ OVER REQUESTED RANGE INTO PLOTTING ARRAY XEXP, YEXP.
        DO 350 I=L,K
        XEXP(I-L+1)=FLOAT(IXEXP(I))
        YEXP(I-L+1)=FLOAT(IYEXP(I))
350     CONTINUE
C     FIND MAX AND MIN VALUES OF INTENSITY FOR PLOTTING RANGE.
      YMAX=0.0
      YMIN=5000.
        DO 370 I=1,K-L
        IF(YEXP(I).GT.YMAX)YMAX=YEXP(I)
        IF(YEXP(I).LT.YMIN) YMIN=YEXP(I)
370     CONTINUE
      YMAX=(YMAX-YMIN)/10.
        DO 380 I=1,K-L+1
        YEXP(I)=YEXP(I)-YMIN
380     CONTINUE
C     PLOT OUT SPECTRUM.
      CALL NEWPAGE
      CALL SCALEZ(1.5)
      CALL LINAXS(1.15,.2,5.10,XL,TICKS,10,-1)
      CALL LINAXS(2.20,5.1,50,10,0,,YMAX,10,-1)
      CALL SYMBOL(6.0,-1,,0.3,'POSITION/UM',0,,11)
      CALL SYMBOL(-1,,7.0,0.3,'INTENSITY',90,,9)
      CALL POINTS(XEXP,YEXP,NUM)
      CALL BUFFEM(0)
      RETURN
      END
```

```
      PROGRAM CALIB(TAPE1,TAPE10,CALDATA,TAPE3=CALDATA)
C    CALIB USES TAPE 10 (THE PARAMETERS OF THE CHEBYSHEV POLYNOMIAL
C    TO CALIBRATE THE INITIAL SPECTRUM (TAPE1). OUTPUTS FILE
C    CALDATA IN FORM OF WAVELENGTH, INTENSITY.
      DIMENSION X(10000),NOY(10000),XLAM(10000)
      CHARACTER*80 IDENT
      READ(1,1) IDENT
    1 FORMAT(A)
        DO 3 I=1,10000
        X(I)=0.
    3   NOY(I)=0
      READ(1,*) NX
      READ(10,*)A1,A,A2,B1,B,B2,C1,C,C2
      READ(1,*,END=4)(NOY(I),I=1,NX)
    4   DO 10 I=1,NX
        XLAM(I)=A+B*FLOAT(I)*.4+C*FLOAT(I)*.4*FLOAT(I)*.4
        WRITE(3,*) XLAM(I),NOY(I)
   10   CONTINUE
      STOP
      END
```

```
C     DISPLAY DISPLAYS AND SELECTED PORTION OF THE SPECTRUM.
C     A MODIFIED VERSION INCLUDES COMMENTED LINE ALSO CALIBRATES
C     THE INTENSITY AND DISPLAYS THE ENERGY PER 40MA.
      PROGRAM COMPARE(INPUT,OUTPUT,CALDATA,TAPE5=INPUT,TAPE3=CALDATA,
     1TAPE6=OUTPUT,TAPE7)
      DIMENSION X(10000),Y(10000)
          DO 5 I=1,10000
          X(I)=0.
    5     Y(I)=0.
      READ(5,*)L
      YM=5000.
C     READ IN THEE POINTS. SUBTRACT OFF THE MIN INTENSITY IE BACKGROUND.
          DO 10 I=1,L
          READ(3,*)X(I),Y(I)
   10     IF(Y(I).LT.YM)YM=Y(I)
         DO 12 I=1,L
         Y(I)=Y(I)-YM
C    43.11 IS C ABSORPTION EDGE. USE NEXT TWO LINES FOR CALIBRATED SPECTRUM.
C       IF (X(I).LT.43.11)Y(I)=Y(I)/(X(I)*375.)
C       IF(X(I).GT.43.11)  Y(I)=Y(I)/16000.
   12     CONTINUE
          YMIN=5000.
          YMAX=0.
C     FIND MAX AND MIN INTENSITIES. PLOT OUT SPECTRUM (PLOTUP).
          DO 15 I=1,L
          IF (Y(I).LT.YMIN)YMIN=Y(I)
          IF(Y(I).GT.YMAX)YMAX=Y(I)
    15    CONTINUE
```

```
      CALL START(2)
   20 CALL PLOTUP(X,Y,L,YMAX,YMIN)
        GOTO 20
      END
C    PLOTUP PLOTS OUT SPECTRUM BETWEEN INDICATED POINTS.
      SUBROUTINE PLOTUP(XEXP2,Y2EXP,NPOINTS,YMAX,YMIN)
      DIMENSION XEXP2(10000),YEXP(10000),XEXP(10000),Y2EXP(10000)
      CALL PROMPT('INPUT 1ST AND LAST POINTS FOR PLOTTING')
      READ(5,*)L,K
      IF(K.EQ.0)  STOP
      TICKS=(XEXP2(K)-XEXP2(L))/10.
      XL=XEXP2(L)
      NUM=K-L+1
          DO 350 I=L,K
          XEXP(I-L+1)=XEXP2(I)
          YEXP(I-L+1)=Y2EXP(I)
  350     CONTINUE
      YDIS=(YMAX-YMIN)/10.
      CALL NEWPAGE
      CALL SCALEZ(1.5)
      CALL LINAXS(1.15.,2.05.,10.,XL,TICKS,10,2)
      CALL LINAXS(2.20,5.1,50.,10.,YMIN,YDIS,10,2)
      CALL SYMBOL(6.0,-1.,0.3,'WAVELENGTH/A',0.,12)
      CALL SYMBOL(-1.2,7.0,0.3,'INTENSITY',90.,9)
      CALL POINTS(XEXP,YEXP,NUM)
      CALL BUFFEN(0)
      RETURN
      END
```

```
C
C     LINEFIT CALCULATES THE THEORETICAL SATEELLITE SPECTRUM USING
C     LEE'S CODE QRATNEW. WAVELENGTHS & INTENSITIES FORM VAINSTEIN
C     AND SAFRANOVA.
      PROGRAM LINEFIT(INPUT,OUTPUT,CALDATA,POPS,TAPE5=INPUT,
     1 TAPE6=OUTPUT,TAPE1=CALDATA,TAPE2=POPS,TAPE62)
      DIMENSION X3(500),Y3(500),Y4(500),X(500),Y(500),
     1 XN1(6),XN(6),XL1(6,9),XL(6,9),R1(9),R(9),NUM(2)
C     READ IN EXPERIMENTAL POINTS (CALDATA)
      READ(1,*)N
      READ(1,*)(X3(I),Y3(I),I=1,N)
      M=N
C     READ IN LEE'S POPULATIONS FOR SATELLITES
C     MAKE SURE POPULATIONS MATCH LINES BELOW.
      WRITE(6,*)N
         DO 30 J=1,6
        READ(2,*)XN1(J),(XL1(J,I),I=1,9)
         WRITE(6,*)XN1(J)
         XN(J)=ALOG10(XN1(J))
            DO 20 I=1,9
            XL(J,I)=ALOG10(XL1(J,I))
20          CONTINUE
30     CONTINUE
C     READ IN HWHM AND BACKGROUND. SUBTRACT OFF BACKGROUND.
      WRITE(6,*)'HALFWIDTH'
      READ(5,*) H4
      WRITE(6,*)'BACKGROUND'
      READ(5,*) B
         DO 35 I=1,M
         Y3(I)=Y3(I)-B
35       CONTINUE
C    SHIFT IS WAVELENGTH SHIFT OF THEORETICAL SPECTRUM.
      WRITE(6,*)'SHIFT'
      READ(5,*) S
         DO 37 I=1,M
         X3(I)=X3(I)-S
37       CONTINUE
```

```
      WRITE(6,*) 'ELEC DEN'
      READ(5,*) XN4
      XN5=ALOG10(XN4)
C     CALCULATE THEORETICAL POPULATIONS AT REQUIRED DENSITY.
C    EXTRAPOLATING LOGARITHMICALLY BETWEEN LISTED POINTS.
           DO 50 J=1,6
          IF(XN(J).GT.(XN5+0.01)) GOTO 60
   50     CONTINUE
   60      DO 70 I=1,9
           R1(I)=XL(J-1,I)+(XL(J,I)-XL(J-1,I))*(XN5-XN(J-1))/
     1  (XN(J)-XN(J-1))
           R(I)=10.0**R1(I)
           WRITE(6,*) R(I)
   70      CONTINUE
C    NEXT DO LOOP SHOULD BE ALTERED TO REQUIRED SATELLITE SPECTRUM.
C    THIS VERSION IS FOR OXYGEEN LYMAN ALPHA SATELLITES.
C GENERATE SPETRUM
C    CALCULATE GAUSSIAN INSTRUMENT PROFILE ABOUT EACH WAVELENGTH.
C    MULTIPLY BY WEIGHTED A-VALUE. MAKE SURE THEY MATCH POPULATIONS.
          DO 80 I=1,M
          D1=R(1)*24.2*GAUSS(H4,X3(I),19.214)
          D3=R(3)*(0.0204*GAUSS(H4,X3(I),19.236)+46.7*GAUSS(H4,X3(I),
     1    19.393))
          D7=46.5/9*GAUSS(H4,X3(I),19.338)
          D8=6.444*GAUSS(H4,X3(I),19.333)+6.433*GAUSS(H4,X3(I),19.338)+
     1    3.8667*GAUSS(H4,X3(I),19.336)
          D9=15.5/3*GAUSS(H4,X3(I),19.336)+0.0145*GAUSS(H4,X3(I),19.494)+
     1    34.8*5/9*GAUSS(H4,X3(I),19.335)
          D4=R(4)*(D7+D8+D9)
          D5=R(5)*23.1*(GAUSS(H4,X3(I),19.309)/9+GAUSS(H4,X3(I),19.307)
     1    /3+GAUSS(H4,X3(I),19.304)*5/9)
           D6=R(6)*(9.85*GAUSS(H4,X3(I),19.771))
          Y4(I)=D1+D3+D4+D5+D6
   80     CONTINUE
C     AREA NORMALIZE THEORETICAL SPECTRUM TO EXPERIMENTAL SPECTRUM.
C     BETWEEN INPUT POINTS. THESE SHOULD BE EITHER SIDE OF SATELLITES.
```

```
      WRITE(6,*)  'INPUT POINTS OVER WHICH TO NORMALIZE'
      CALL RATIO(X3,Y3,Y4,T2,E2)
      R3=T2/E2
          DO 100 I=1,M
          Y4(I)=Y4(I)/R3
  100     CONTINUE
      01=0.
      02=0.
C    CALCULATE QUALITY OF FIT PARAMETER Q.
      WRITE(6,*)  INPUT 1ST+NTH POINTS TO CALCULATE Q'
      READ(5,*)  I1,I2
      DO 140 I=I1,I2
      01=01+(Y3(I)-Y4(I))**2
      02=Y4(I)**2+02
  140 CONTINUE
      Q=01/02
C     PLOT OUT SPECTRUM
      CALL START(2)
      CALL PLOTUP(X3,Y3,Y4,M)
      CALL SYMBOL(2.,14.,.3,'LOG ELEC DENSITY',0.)
      CALL NUMBER(7.,14.,.3,XN5.2,.2)
      CALL SYMBOL(10.,14.,.3,'HALFWIDTH',0.)
.     CALL NUMBER(13.,14.,.3,H4/2.,0.,3)
      CALL SYMBOL(2.,13.,.3,'Q =',0.)
      CALL NUMBER(3.5,13.,.3,Q,0.,3)
      CALL ENPLOT
      END
C    RATIO CALCULATES AREA UNDER INPUT PORTION OF SPECTRUM.
      SUBROUTINE RATIO(X1,Y1,Y2,T2,E2)
      DIMENSION X1(500),Y1(500),Y2(500)
      WRITE(6,*)'1ST POINT'
      READ(5,*)IF2
      WRITE(6,*)'NTH POINT'
      READ(5,*)L2
      E2=0
      I=0
```

```
          DO 200 I=IF2,L2-2
          E2=E2+(Y1(I)+Y1(I+1))*(X1(I+1)-X1(I))/2
          T2=T2+(Y2(I)+Y2(I+1))*(X1(I+1)-X1(I))/2
  200     CONTINUE
      RETURN
      END
C
C   GAUSS CALCULATES VALUE OF A GAUSSIAN AT INDICATED POINT.
      FUNCTION GAUSS(H4,X1,X)
      GAUSS=.9394/(H4*EXP(2.7726/((H4/(X1-X))**2+0.035)))
      RETURN
      END
C    PLOTUP PLOTS OUT SPECTRUM.
          SUBROUTINE PLOTUP(XEXP,YEXP,YTH,M)
          DIMENSION YEXP(4000),XEXP(4000)
          TICKS=(XEXP(M)-XEXP(1))/10.
          XL=XEXP(1)
          YMAX=0.0
            DO 370 I=1,M
            IF(YEXP(I).GT.YMAX)YMAX=YEXP(I)
  370       CONTINUE
          YMAX=YMAX/10.
          CALL NEWPAGE
          CALL SCALEZ(1.5)
          CALL LINAXS(1.15,,2.05,10,XL,TICKS,10,2)
          CALL LINAXS(2.20,5,1.50,10,0,,YMAX,10,-1)
          CALL SYMBOL(6.0,-1,,0.3,'WAVELENGTH/A',0,,12)
          CALL SYMBOL(-1,,7.0,0.3,'INTENSITY',90,,9)
            DO 372 I=1,M
          CALL ERRV(XEXP(I),YEXP(I),YMAX/10,,TICKS/10,,2)
 372        CONTINUE
          CALL POINTS(XEXP,YTH,M)
          CALL BUFFEM(0)
          RETURN
          END
```

```
C    CONTHK FITS THEORETICAL STARK PROFILES OF GRIEM. OPACITY
C    BROADENS THEM AND CONVOLVS WITH INSTRUMENTAL GAUSSIAN.
C    RESULT IS COMPARED WITH EXPERIMENTAL SPECTRUM.
C    FILES REQUIRED ARE STARK- GRIEMS PROFILES: EXPPROF- EXPERIMENTAL
C     PROFILES
      PROGRAM CONTHK(STARK,EXPPROF,OUTPUT,INPUT,TAPE1=STARK,
     1 TAPE2=EXPPROF,TAPE6=OUTPUT,TAPE5=INPUT)
      DIMENSION ALP(2000),XINT(2000),YINT(2000),XLAM(2000),YLAM(2000),
     1 WORK(2000),XEXP(2000),IYEXP(2000),XINST(2000),YINST(2000),
     2 X(1400),Y(1400),XALP(70),XXINT(70),XXEXP(2000),IIYEXP(2000),
     3 YEXP(2000)
      REAL NE,NL,LD,KT
C     INPUT PARAMETERS FOR OPACITY CALCULATION.
      WRITE(6,*) 'INPUT KT,NL,F,NE,LAMBDA,HALFWIDTH,BACKGROUND,SHIFT'
      READ(5,*) KT,NL,F,NE,LD,H4,IBACK,SHIFT
      A=1.193E26/LD**5.
      B=12416/KT
      C=7.08E-12*F*NL*LD**2./NE**(2./3.)
      N=1
         DO 5 I=1,2000
         YINST(I)=0.
         YLAM(I)=0.
    5    CONTINUE
C    READ IN STARK PROFILES
   10  READ(1,*)ALP(N),XINT(N)
       N=N+1
       IF(ALP(N-1).NE.99.0)GOTO 10
       N=N-2
C      CONVERT EV TO ANGSTROMS
          DO 20 I=1,N
          ALP(I)=1.25E-9*NE**0.667*ALP(I)
   20     CONTINUE
       SP=IFIX(ALP(1)/5E-03)*5E-03
       L=1
C     RECALCULATE PROFILES EVERY 5MA.
   25  I=1
```

```
   30 I=I+1
         IF(ALP(I).LE.SP)GOTO 30
      YINT(L)=XINT(I)-(ALP(I)-SP)*(XINT(I)-XINT(I-1))/
     1 (ALP(I)-ALP(I-1))
      XLAM(L)=SP
      SP=SP+5E-3
      L=L+1
      IF(SP.LE.-ALP(1))GOTO 25
      SP=SP-5E-3
      L=L-1
      YSUM=0.
      TMAX=0.
           DO 40 J=1,L
C     CALCULATE OPACITY BROADENED PROFILES.
           IF(C*YINT(J).GT.TMAX)TMAX=C*YINT(J)
           YLAM(J)=A*(1-EXP(-C*YINT(J)))/(EXP(B/LD)-1)
   40      CONTINUE
C     CALCULATE INSTRUMENTAL PROFILES
           DO 50 I=1,L
           IF((XLAM(I)**2./H4**2.).GT.1000.)THEN
           YINST(I)=0.
           ELSE
           YINST(I)=EXP(-0.693*XLAM(I)**2./H4**2.)
           ENDIF
  50       CONTINUE
C     PERFORM CONVOLUTION
C     C06FKF IS NAG LIBRARY ROUTINE.
      IFAIL=0
      CALL C06FKF(1,YINST,YLAM,2000,WORK,IFAIL)
        N=1
C     READ IN EXPERIMENTAL PROFILES
 60      READ(2,*)XEXP(N),IYEXP(N)
         IYEXP(N)=IYEXP(N)-IBACK
         XEXP(N)=XEXP(N)
         N=N+1
         IF(XEXP(N-1).NE.99.0)GOTO 60
```

```
      N=N-2
       DO 80 I=1,L
       Y(I)=YINST(I+L/2)
       X(I)=XLAM(I)+SHIFT+LD
80     CONTINUE
      YTSUM=0.
C     AREA NORMALIZE PROFILES
      YESUM=0.
      DO 81 I=2,L
81    YTSUM=YTSUM+ABS((Y(I)+Y(I-1))*(X(I)-X(I-1)))
      DO 83 I=2,N
83    YESUM=YESUM+ABS(FLOAT(IYEXP(I)+IYEXP(I-1))*(XEXP(I)-XEXP(I-1)))
      DO 85 I=1,L
85    Y(I)=Y(I)/YTSUM
        DO 90 I=1,N
        YEXP(I)=FLOAT(IYEXP(I))/YESUM
90      CONTINUE
C     PLOT OUT SPECTRUM
      CALL START(2)
      CALL PLOTUP(X,Y,XEXP,YEXP,L,N)
      CALL SYMBOL(2.,14.,.3,'LOG ELEC DENSITY',0.)
      CALL NUMBER(7.,14.,.3,ALOG10(NE),0.,2)
      CALL SYMBOL(10.,14.,.3,'INST WIDTH',0.)
      CALL NUMBER(14.,14.,.3,W4,0.,3)
      CALL SYMBOL(2.,13.,.3,'LOG NI*NL',0.)
      CALL NUMBER(7.,13.,.3,ALOG10(NL),0.,2)
      CALL SYMBOL(10.,13.,.3,'KT',0.)
      CALL NUMBER(14.,13.,.3,KT,0.,-1)
      CALL SYMBOL(10.,12.,.3,'TMAX',0.)
      CALL NUMBER(14.,12.,.3,TMAX,0.,2)
      CALL QSUBR(XEXP,YEXP,N,X,Y,L)
      CALL ENPLOT
      END
```

```
C     PLOTUP PLOTS OUT SPECTRUM
            SUBROUTINE PLOTUP(X,Y,XEXP,YEXP,L,N)
            DIMENSION XEXP(2000),YEXP(2000),X(1400),Y(1400)
            TICKS=(XEXP(N)-XEXP(1))/10.
            XL=XEXP(1)
            YMAX=0.0
              DO 370 I=1,N
              IF(YEXP(I).GT.YMAX)YMAX=YEXP(I)
  370         CONTINUE
             DO 380 I=1,L
  380        IF(Y(I).GT.YMAX)YMAX=Y(I)
            YMAX=YMAX/8.
            CALL NEWPAGE
            CALL SCALE7(1.5)
            CALL LINAXS(1.15,.2.05,10,XL,TICKS,10,2)
            CALL LINAXS(2.20,5.1,50,10,0.,YMAX,10,2)
            CALL SYMBOL(6.0,-1.,0.3,'WAVELENGTH/A',0.,12)
            CALL SYMBOL(-1.,7.0,0.3,'INTENSITY',90.,9)
            CALL POINTS(X,Y,L)
              DO 390 I=1,N
              CALL ERRV(XEXP(I),YEXP(I),YMAX/10.,TICKS/10.,2)
  390         CONTINUE
            CALL BUFFEM(0)
            RETURN
            END
C    QSUBR CALCULATES QUALITY OF FIT PARAMETER Q
       SUBROUTINE QSUBR(X1,Y1,N,X2,Y2,M)
       DIMENSION X1(2000),Y1(2000),X2(2000),Y2(2000)
       Q1=0.
       Q2=0.
         DO 1500 I=1,N
           DO 1010 J=1,M
             IF(X2(J).GT.X1(I)) GOTO 1020
 1010      CONTINUE
```

```
            GOTO 1500
1020        IF(J.EQ.1) J=2
            YB=ABS(Y2(J)-(Y2(J)-Y2(J-1))*(X2(J)-X1(I))/(X2(J)-X2(J-1)))
            Q1=(Y1(I)-YB)**2+Q1
            Q2=Q2+YB**2
1500     CONTINUE
            Q=Q1/Q2
         CALL SYMBOL(2.,12.,0.3,'Q IS',0.)
         CALL NUMBER(7.,12.,0.3,Q,0.,4)
         RETURN
         END
```

REFERENCES

1 AIP conf proc (1981), no 75, whole conference.

2 Baranger, M. (1962), Chapter 13 in Atomic and Molecular processes, (ed Bates, D.) Academic Press

3 Bates, D. R., Kington, A. E., McWhirter, R. W. P., Proc. Roy. Soc. A 270 p155 1962

4 Bleach, R. D., Burkhalter, P. G., Nagel D. J., NRL memo report 4732

5 Burkhalter P. et al (1979) J. Appl. Phys. 50 p705

6 Ceglio, N. M., Hawryluk, A. M., Price, R. H. (1981) SPIE 316 High resolution soft x-ray optics p134

7 Challis, C. D. (1986) PhD Thesis, Univ London

8 Cuthill, J. R. (1974) chapter 3 in X-ray spectroscopy (ed Azaroff, L. V.) McGraw Hill

9 Davies, J., Duston, D. (1982) JQSRT 27 p267

10 de Michelis, C., Mattioli, M. (1981) Nuclear Fusion 21 p677

11 Dubau, J., Volonte, S. (1980) Rep. Prog. Phys. 43 p199

12 Duston, D., Davies, J. (1980) Phys. Rev. A 21 p1664

13 Elton, R. C., Lie, T. N., (1971) Phys. Rev. A3 p875

14 Fawcett, B. C. (1984) At Dat Nucl Dat Tables 30 p1

15 Feldman, U. (1981) Physica Scripta 24 p681

16 Gabriel, A. H., Bhalla, C. P., Presnyakov, L. P. (1975) MNRAS 172 p359

17 Gabriel, A. H., Jordan, C. (1969) Nature 221 p947

18 Gabriel, A. H., Paget, T. M. (1972) J. Phys. B 5 p673

19 Gill, R. D. (1981) Chapter 27 of Plasma Physics and

Nuclear Fusion research

20 Griem, H. R. (1964) Plasma Spectroscopy. McGraw Hill Book Co.

21 Griem, H. R. (1974) Spectral line broadening by plasmas. Academic press.

22 Haines, M. G. (1982) Physica Scripta T2 p380

23 Henke Shattenburg (1975) Adv X-ray Anal 19 p749

24 Holtsmark, J. (1919) Ann. Phys. 58 p577

25 IAEA conf proc (1984) in Plasma physics & controlled nuclear fusion research. Vol 3.

26 ICCC bulletin (1982) No. 4.12/1(6) SIMPLE

27 Jacobs, V. C., Blaha, M. (1980) Phys. Rev. A 21 p525

28 Jahoda, F. C., Sawyer, G. A., Ribe, F. L., Stratton, T. F. (1962) JQSRT 2 p467

29 Kania, R., Jones, L. A., (to be published) Phys Rev Lett

30 Kelly, R. L., Polumbo, L. J., (1973) NRL report 7599

31 Kepple, P. C., Griem, H. R. (1978) NRL memo report 3634

32 Key, M. H., Lunney J. G., Ward, M., Evans, R., Rumsby, P., J. Phys. B 12 L213 1979

33 Kilkenny, J. D. et al (1980) Phys Rev A 22 p2746

34 Kilkenny, J. D., Lee, R. W., Whitten, B. L., MacGowan, B., Bradley, D. (unpub) Density dependence of dielectronic satellites of He-like ions.

35 Lee, R. W., Whitten, B. L., Strout, R. E. (1984) JQSRT 32 p91

36 Lunney, J. G. (unpub) Measurement of electron temperature and state of ionization in laser produced plasmas using dielectronic satellite lines.

37 Mather, J. W. (1971) Methods of Experimental Physics 9B (ed Lovberg, R. H., Griem, H. R.) p187 Academic press

38 Matthews, D. L. et al (1985) Phys Rev Lett 54 p110

39 Maxon, S., Wainwright, T. (1984) Phys Fluids 27 p2535

40 McWhirter, R. W. P. (1965) in Plasma Diagnostic Techniques

41 Mrowka, S. (1983) PhD Thesis, Univ London

42 Peacock, N. J., Hobby, M. G. (1972) J Phys E 6 p854

43 Seaton, M. J. (1962) Atomic and Molecular processes (ed Bates D. B.) p374. Academic press.

44 Seely, J. F. (1979) Phys Rev Lett 42 p1606

45 Seely, J. F. (1981) At Dat Nucl Dat Tables 26 p138

46 Shiloh, J., Fisher, A., Rostoker, N., (1978) Phys Rev Lett 40 p515

47 Shiloh, J.,Burkhalter, P. G., Fisher, A., Cowan, R. D., J Appl Phys 50 p4532 **1979**

48 Sigel, R. (1982) Nuclear Fusion 22 p665

49 Speer, R. J. (1976) Space Sci. Instrum 2 p463

50 Thorne, A. P. (1974) Chapter 11 in Spectrophysics Chapman and Hall Ltd.

51 Tighe, R. J., Hooper, C. F. (1977) Phys Rev A 15 p1773

52 Vainstein, L. A., Safranova, U. I., (1978) At Dat Nucl Dat Tables 21 p49

53 Vinogradov, A. V., Skobelev, I. Yu., Yukov, E. A., Sov J. Quant Elect. 5 p630 **1975**

54 Vinogradov, A. V., Skobelev, I. Yu., Yukov, E. A., Sov Phys JETP 45 p925 **1977**

55 Wiese, W. L., Smith, M. W., Miles, B. M. (1969) NSRDS National Bureau of Standards 22